

Encapsulation of a retina implant

A dissertation submitted to the
faculty of Electrical Engineering and Information Technology
of the University of Stuttgart
for the degree of Doctor of Engineering

presented by
Martin Rojahn
from Halle an der Saale

accepted on the recommendation of

Prof. Dr. J. H. Werner, referee,
Prof. Dr. E. Zrenner, co-referee

day of oral examination: February 7 2003

Institute of Physical Electronics
Stuttgart 2003

Verkapselung eines Netzhaut-Implantates

Von der Fakultät Elektrotechnik und Informationstechnik
der Universität Stuttgart
zur Erlangung der Würde eines
Doktor-Ingenieurs (Dr.-Ing.)
genehmigte Abhandlung

Vorgelegt von
Martin Rojahn
aus Halle an der Saale

Hauptberichter: Prof. Dr. J. H. Werner
Mitberichter: Prof. Dr. E. Zrenner

Tag der mündlichen Prüfung 7. Februar 2003

Institut für Physikalische Elektronik
Stuttgart 2003

Contents

Zusammenfassung	9
Summary	13
1 Introduction	17
1.1 Motivation	17
1.1.1 Concepts of retinal implants	18
1.1.2 Stimulation of neural activity	20
1.2 Encapsulation of a retina implant & Aim of this work	21
1.3 Organization	22
2 Thin-film micro-photodiodes for retina stimulation	25
2.1 Amorphous silicon basics	26
2.2 Photodiode design	27
2.2.1 The size of micro-photodiodes & achievable resolution .	30
2.3 Fabrication steps	30
2.4 Current-voltage measurements	33
2.4.1 Failure of conventional low-temperature deposited SiN_x encapsulation	35
3 Biostability of a Retina implant	37
3.1 Current status	37
3.2 Novel encapsulation materials	39
3.2.1 $\text{SiO}_x\text{:C/SiN}_y$	40
3.2.2 Benzocyclobutene – BCB	43
3.2.3 Polyimide 2611 – PI	45
3.2.4 Ultra-thin PI- and BCB layers	46
3.2.5 Morphology of the polymers	47
3.3 Sealing of stimulation electrodes	48
4 Cell-cultures for in-vitro tests	53

4.1	Cell-cultures	53
4.1.1	Cell culture procedures	55
5	Measurement techniques	59
5.1	Choice of techniques	59
5.2	Impedance spectroscopy	60
5.2.1	Experimental setup	60
5.2.2	Equivalent circuit	62
5.2.3	Mathematical description and fitting routine	64
5.2.4	Electrolyte cell without a dielectric	68
5.3	Fast Fourier infrared spectroscopy	69
5.3.1	Infrared spectrum of Dulbecco's medium	70
5.4	X-ray photoelectron spectroscopy	72
5.4.1	Mathematical fit of spectra	72
5.4.2	Repeated measurements on <i>one</i> PI sample	76
6	Experimental results and discussion	79
6.1	Inorganic $\text{SiO}_x\text{:C/SiN}_x$	80
6.1.1	Impedance spectroscopy	80
6.1.2	Fast Fourier Transform Infrared Spectroscopy – FTIR	82
6.1.3	X-ray Photoelectron Spectroscopy	86
6.1.4	Model for surface degradation	91
6.1.5	Summary: $\text{SiO}_x\text{:C/SiN}_y$	94
6.2	Benzocyclobutene	95
6.2.1	FTIR	96
6.2.2	XPS-analysis	98
6.2.3	Impedance spectroscopy	101
6.2.4	Summary: BCB	102
6.3	Polyimide	103
6.3.1	FTIR Spectroscopy	104
6.3.2	XPS analysis	106
6.3.3	Summary of biostability analysis with FTIR and XPS	112
6.3.4	Impedance spectroscopy	113
6.3.5	Summary: PI 2611	127
7	Appendix	129
7.1	Composition of the Dulbecco's growing medium and the phosphate buffered saline	129
7.2	RC-line- and Warburg impedance	131
	Abbreviations and constants	135

<i>CONTENTS</i>	7
Symbols	137
Bibliography	145
Danksagung (Acknowledgment)	163
Curriculum vitae (English)	165
Lebenslauf (Deutsch)	167

Zusammenfassung

Seit ca. sieben Jahren entwickeln internationale Forschergruppen halbleiterbasierte Implantate für die lichtempfindliche Netzhaut des Auges (Retina), die bei erblindeten Patienten mit einem bestimmten Krankheitsbild zur teilweisen Wiederherstellung des Sehens beitragen sollen. Die Langzeitstabilität eines solchen Implantates im menschlichen Organismus gehört zu den wissenschaftlichen und technischen Herausforderungen, die vor einer ersten Anwendung des Chips beim Menschen gelöst werden müssen. Biokompatibilität, Transparenz für sichtbares Licht und im nahen Infrarotbereich, technologische Kompatibilität zur kommerziellen Fertigung des Chips und eine möglichst niedrige Abscheidetemperatur gehören dabei zu den Bedingungen, die das Verkapselungsmaterial erfüllen muss, damit die Funktion des Chips gewahrt bleibt.

Die von Projektpartnern gefertigten ersten Chip-Generationen sind mit Siliziumdioxid, das aus Tetraethylorthosilikat hergestellt wird (TEOS SiO_2), als Verkapselungsschicht ausgestattet. Nach sechs- bis zwölfmonatigen Implantationen in Versuchstieren entwickelt das Material jedoch Löcher und zeigt eine fortschreitende Auflösung. Die exakten Degradationsvorgänge unter in-vivo Bedingungen sind dabei weitgehend unbekannt. Im Rahmen der vorliegenden Arbeit werden a-Si:H Mikrophotodioden mit einer Leerlaufspannung $V_{oc} = 2.3 \text{ V}$ zur in-vitro Stimulation von Retinae neu entwickelt und hergestellt. Das dabei zur Verkapselung verwendete Niedrigtemperatur Siliziumnitrid wird mittels Plasma-unterstützter Gasphasenabscheidung hergestellt (PE-CVD SiN_x). In der Arbeit durchgeführte Tests zeigen, dass das Material unter elektrischer Spannung einer Elektrolytumgebung nicht stand hält. Schäden treten insbesondere im Bereich der Durchführungen für die Stimulationselektroden auf, wo die geätzten Flanken des SiN_x nicht homogen durch das Elektrodenmaterial abgedeckt und damit geschützt werden.

In dieser Arbeit werden drei Materialien getestet, deren Biokompatibilität bekannt ist und die als Kandidaten für zukünftige Retina-Implantate in Frage kommen: (i) $\text{SiO}_x\text{:C/SiN}_y$, (ii) Benzocyclobuten (BCB) und (iii) Poly-

imid 2611 (PI). Die chemische Zusammensetzung wird durch Röntgen-Photoelektronen-Spektroskopie (XPS) und Fast Fourier Transmissions-Infrarotspektroskopie (FTIR) untersucht, während die Impedanzspektroskopie (IS) zur Analyse der elektrischen Eigenschaften aller drei Dielektrika dient. Die in der Arbeit entwickelten extrem dünnen Testschichten der beiden Polymere (Schichtdicke $d_{or} \approx 50$ nm) ermöglichen die frühzeitige Beobachtung von Änderungen an der Oberfläche der Materialien. Da die genannten Messmethoden eine Mindestgröße A_{ts} der Testkörper von $A_{ts} \geq 8 \times 8$ mm² erfordern, können nicht alle Testkörper in in-vivo Testreihen untersucht werden. Stattdessen werden in dieser Arbeit Experimente entwickelt, die mit Hilfe von in-vitro Zellserien mit (i) Ratten-Brusttumorzellen (BICR/M1R_k) und (ii) Gebärmutterhalstumorzellen (HeLa) die in-vivo Bedingungen implantierter Chips teilweise nachbilden.

Die Kombination der Ergebnisse der oberflächen- und volumensensitiven Analysen ermöglicht die Erstellung einer „Rangordnung“ der Materialien in Bezug auf ihre Biostabilität:

SiO_x:C/SiN_y erreicht den dritten Platz. Die von Projektpartnern bei Temperaturen von unter 100°C abgeschiedene Sandwich Struktur ist über mehrere Wochen biostabil und weist eine sehr geringe Dichte von Fehlstellen auf. Sie stellt damit einen wesentlichen Fortschritt gegenüber der PECVD SiN_x Einzelschicht dar. Für das Retina-Implantat kann SiO_x:C/SiN_y als äußere Schutzschicht für die darunterliegende dauerhafte Verkapselungsschicht eingesetzt werden, um Kratzern etc. vorzubeugen, die durch die Handhabung während der Implantation des Chips entstehen können. Über einen längeren Zeitraum wird sich das Material – in jedem Fall die obere SiN_x Schicht – auflösen. Sowohl FTIR als auch XPS zeigen eine kontinuierliche Abnahme der Dichte der Si-N Bindungen mit einer Rate $ds_s \approx 1 \dots 2$ nm d⁻¹ in Zellkulturmedium. Si-N Bindungen werden durch C-N Bindungen ersetzt, wobei das Ausmaß von der Art der Zellkultur mitbestimmt wird.

Benzocyclobuten erlangt Platz zwei. Im Gegensatz zu SiO_x:C/SiN_y nehmen materialspezifische Bindungen – bei BCB z.B. die Etherbindung Si–O–Si – nach der Behandlung mit Zellmedien nur in sehr geringem Maße ab. Weder XPS noch FTIR deuten auf eine fortschreitende Zerstörung des Materials hin. Die Impedanzspektroskopie zeigt einen (innerhalb der Messgenauigkeit) unveränderten Parallelwiderstand, der den Herstellerangaben entspricht. Darüber hinaus werden in dieser Arbeit in Designstudien von Elektrodendurchführungen trichterförmige Ätzflanken im BCB erzielt, die sich nach oben öffnen (positive Ätzflanken). Auf die positiven Ätzflanken abgeschiedenes Gold oder Titanitrid (Sputterprozess) führt zu einer homogenen Bedeckung dieses korrosionsempfindlichen Übergangsbereiches. Aus den vorläufigen Ergebnissen von Kohler und Stelzle [1] geht jedoch hervor,

dass das für die Stimulationselektroden eines Implantates vorgesehene Titanitrid (TiN) nach einjähriger subretinaler und subcutaner Implantation in Tieren eine unzureichende Haftung auf BCB aufweist. Die BCB- Proben waren im Rahmen dieser Arbeit hergestellt worden.

Polyimid 2611 ist das zuverlässigste Material für den Langzeitschutz eines Implantates. Die chemische Struktur des Polyimides ändert sich nicht nach Zellkulturtests, wie die in der Arbeit durchgeführten FTIR Messungen belegen. Gleichermaßen zeigt die Impedanzspektroskopie keine Unterschiede in der Kapazität und dem Parallelwiderstand des Materials nach Behandlung mit Salzlösung oder Zellkulturen. Innerhalb der ersten 24 h Elektrolytbehandlung nach der Probensterilisation in einem Trockenofen bei einer Temperatur $T_{h.o.} = 105^{\circ}\text{C}$ deutet die IS jedoch auf einen diffusions-ähnlichen Prozess von Elektrolytkomponenten in eine oberflächennahe Schicht des Polyimid hin. Basierend auf einem physikalischen Modell für PI-Schichten mit einem kolumnar-ähnlichen Volumen und einer hohen Oberflächenrauigkeit, entwickelt die vorliegende Arbeit ein Ersatzschaltbild für das PI-Elektrolyt-system im Frequenzbereich $f = 10^{-3} \dots 10^7$ Hz: Je ein Parallel-RC-Glied beschreibt die Helmholtz-Doppelschicht und das PI Volumen; die Oberflächenschicht des PI ist durch eine Warburg (Diffusions-) Impedanz dargestellt. Die Diffusion von Elektrolytkomponenten führt zu einem PI-Elektrolyt-Übergangsbereich mit einer Dicke $d_{(PI),s} \approx 3 \dots 10\text{nm}$, in dem eindiffundierte Ionen und Moleküle in die Biphenyldianhydrid / 1,4 Phenylendiamin- Matrix (BPDA/PPD) des Polyimids eingebettet sind. Diese Modellvorstellung wird ebenfalls gedeckt durch die XPS Ergebnisse: Zum einen zeigen sie eine Verbreiterung PI-spezifischer Bindungsenergie-Spektren. Zum anderen verdeutlichen Zeitserien mit Spülschritten des PI mit deionisiertem Wasser, dass der Spüleffekt mit zunehmender Behandlungsdauer der Proben in Zellmedium abnimmt, während sich die genannte Verbreiterung der XPS-Spektren innerhalb der ersten Stunden in Zelllösung verstärkt. Die Aufnahme von Elektrolytbestandteilen führt nicht zum Bruch kovalenter Bindungen im BPDA/PPD Gerüst. Kohler und Stelzle [1] untersuchen mit optischen Mikroskopen PI- Proben und BCB- Proben nach einjähriger subretinaler und subkutaner Implantation in Versuchstieren. Ihre vorläufigen Ergebnisse zeigen keinerlei Degeneration beider Polymere. Als Konsequenz aus der analytisch gefundenen – und in Tierexperimenten belegten – überlegenen Biostabilität wird Polyimid 2611 als Verkapselungsmaterial für die nächste Generation von Retina-Implantaten eingesetzt werden.

Summary

Over the last seven years, international research groups have started developing semiconductor-based implants for the light-sensitive retina part of the eye. Such devices are aimed at restoring some vision in blind patients with a certain eye disease pattern. A retina implant must have an encapsulation layer which serves two purposes: (i) It prevents the direct contact of the surrounding tissue to the electronic components of the chip which may not be biocompatible. (ii) The encapsulation protects the chip against its biological environment which would dissolve an uncoated silicon device. The long-term biostability of the encapsulation in the eye presents a scientific and technological challenge which must be solved before an implantation in a human being can be attempted. In order to maintain the functional integrity of the implant, the encapsulation layer must be biocompatible and transparent in the visible and near infrared spectrum. Technological requirements include a low deposition temperature of the material and the overall compatibility of the process to a standard commercial silicon chip fabrication.

The first retina chip generations, manufactured by project partners, feature a SiO_2 encapsulation which is deposited from *tetra-ethyl-ortho-silicate* (TEOS). Six to twelve months after implantation in laboratory animals, the thickness of the SiO_2 layer decreases and the material shows pit-corrosion. The exact mechanism of the progressive degradation is largely unknown. Novel micro-photodiodes with an open circuit voltage of $V_{oc} = 2.3$ V for the in-vitro stimulation of retinal tissue are designed and manufactured in this work. Plasma-enhanced chemical vapor deposition (PE-CVD) at substrate temperatures below 75°C is employed to grow the SiN_x encapsulation of the device. The micro-photodiodes do not withstand the electrolyte attack under illumination, as shown by tests performed in this work. The SiN_x exhibits structural defects (pin holes), but most corrosion-damage is observed in the vicinity of the feed-throughs of the stimulation electrodes through the encapsulation layer, where the etched SiN_x is not homogeneously covered (and thereby protected) by the gold- electrode material.

This work takes a broad approach for the evaluation of three alterna-

tive biocompatible materials which are candidates for future retina implant devices: (i) $\text{SiO}_x\text{:C/SiN}_y$, (ii) dry-etch benzocyclobutene (BCB, Dow Chemical) and (iii) polyimide 2611 (PI, HDMicrosystems, DuPont). In order to be able to detect *early stages* of changes at the polymers' surface, a process for the fabrication of ultra-thin samples with a thickness $d_{or} \approx 50$ nm is developed. Surface sensitive X-ray photoelectrospectroscopy (XPS) and volume- and surface sensitive Fast Fourier transmission infraredspectroscopy (FTIR) serve to analyse the chemical composition of the materials; impedance spectroscopy is employed to observe the electronic behavior of the dielectric materials. Chiefly because of the required size of the test samples for the analytical experiments, $A_s \geq 8 \times 8 \text{ mm}^2$, not all test specimen can be put to in-vivo trials. In order to at least partly simulate the in-vivo conditions of animal tests, in-vitro cell culture experiments with (i) female rat mammary tumor cells (BICR/MIR_k) and (ii) human cervix carcinoma (HeLa) cell lines are devised in this work.

The combined data from all analytical experiments allow a ranking of the three encapsulation materials with regard to their overall biostability:

SiO_x:C/SiN_y reaches the third position. Deposited at temperatures below 100°C, the sandwich structure is biostable for several weeks and presents a major progress from the single layer PE-CVD SiN_x. Impedance spectroscopy proves the high parallel resistance of the dielectric which points to a very low pin-hole density. In the context of the retina implant, SiO_x:C/SiN_y may be used as an outer protective layer for the main, long-lasting encapsulation material against mechanical damage (scratches) resulting from the handling in the implantation surgery. Over a period of several weeks to month, the sandwich structure will dissolve. Both FTIR and XPS show a continuous decline in the Si-N bonds resulting from a progressing dissolution of the top SiN_y layer by $d_{ss} \approx 1 \dots 2 \text{ nm d}^{-1}$ in cell culture media. Depending on the cell line, Si-N bonds are replaced by C-N bonds to varying degrees of concentration.

BCB comes on second position. In contrast to SiO_x:C/SiN_y, only a minor decrease of material-specific chemical bonds – eg the ether group Si–O–Si for BCB – is observed after the exposure to cell culture media. Neither XPS nor FTIR indicate a progressing degradation of the polymer. Impedance spectroscopy again demonstrates the layer's high parallel resistance after the cell culture tests. Moreover, in a design study performed in this work, funnel-shaped feed-throughs in BCB for the stimulation electrodes of an implant device are achieved (wide openings at the BCB surface). Such etch flanks in BCB provide the basis for the homogeneous coverage of the corrosion sensitive electrode–encapsulation layer interface by the electrode material. However, preliminary results from Kohler and Stelzle [1] indicate delamina-

tion problems of the titanium nitride electrode material (TiN, deposited by project partners in a sputter process) on BCB samples after one year subretinal and subcutaneous implantation in laboratory animals. The BCB samples had been manufactured in this work.

PI 2611 is the most promising material for the long-term protection of the implant: The chemical backbone structure of the polymer remains unchanged after cell culture tests as demonstrated by FTIR. Similarly, impedance spectroscopy shows no changes of the capacitance and the parallel resistance of the material after exposure to physiological sodium chloride solution or cell cultures. However, within the first 24 h of electrolyte treatment after the hot-oven sterilization at a temperature $T_{h.o.} = 105^{\circ}\text{C}$, the impedance spectroscopy points to a diffusion-like process of electrolyte components into the surface layer of the polyimide. Based on a physical model of the polyimide layer with a columnar-like bulk structure and a high surface roughness, this work develops an electric equivalent circuit for the PI-electrolyte system in the frequency range $f = 10^{-3} \dots 10^7$ Hz: The Helmholtz double layer and the bulk material are each described by a parallel RC element; the surface region of PI is represented by a *Warburg* (diffusion) impedance. The diffusion process leads to a smooth interface region, $d_{IF} \approx 3 \dots 10$ nm, at the PI's surface where ions or molecules are embedded into the biphenyldianhydride / 1,4 phenylenediamine (BPDA/-PPD) matrix of the polyimide. This model is supported by the XPS experimental results: On the one hand, XPS shows a broadening of PI-specific chemical bonds. On the other hand, time-series experiments of deionized-water rinse of PI demonstrate a decline of the water-rinse effect with increasing duration of exposure of the PI samples to the cell culture medium. The XPS peaks broaden simultaneously. The "water" uptake does not, however, result in the break up of bonds in the BPDA/PPD backbone structure. Kohler and Stelzle [1] examine with optical microscopes PI- and BCB samples after implantation in laboratory animals for one year. Preliminary results show no degradation of either polymer and a high adhesive strength of the TiN-PI system, thereby supporting the analytically found superior biostability of the polyimide. PI 2611 will be the encapsulation material of the next generation of subretinal implants.

Chapter 1

Introduction

1.1 Motivation

Men learn most about their environment through vision. Light passing through the cornea and iris is focussed by the lens onto the light sensitive retina part of the eye, see Figure 1.1 (A), see Bargmann [2]. There, roughly 130 million photoreceptor cells (rods and cones¹) transform the incoming light into electrical impulses through a chemical reaction of the rhodopsin molecule² [7]. The inner retina layers (horizontal cells, bipolar cells, amacrine cells and ganglion cells) are thus stimulated by the photoreceptors and perform their neural-network processing part before the "image signal" reaches the axons of the ganglion cells and travels along the optic nerve (approximately 3 mm in diameter, 50 mm in length, consisting of roughly one million "fibers" which are clustered into bundles) to the visual cortex.

¹The density of the rods and cones highly varies across the retina. In the fovea centralis (or makula), approximately 30.000 color sensitive cones provide for high resolution color pictures. Further away from the retina's center, rods mix between the cones and the resolution of the eye decreases. Rod cells do not distinguish between colors; they are, however, exceedingly light sensitive and enable us to detect motion when it is too dim for the cones to respond to [5, 6]. In total, there are about 130 million rods and 6 million cones.

²Rhodopsin consists of large protein *opsin* joined to 11-*cis-retinal*. Upon illumination (rhodopsin has a broad absorption band with its maximum around $\lambda_l = 500$ nm, $\alpha_{(l)500nm} \approx 40.000 \text{ cm}^{-1}\text{M}^{-1}$, see Stryer [7]), the cis-double-bond between the C-11 and C-12 in the retinal isomer is temporarily converted into a single bond. The molecule can now rotate 180° around this bond before the double bond reforms and the molecule reaches the *trans* isomer shape. The bond between the *opsin* and the *trans* retinal is energetically less stable and breaks off eventually. In that process, the movements of both separating molecules trigger nerve impulses which travel to the visual cortex. The free *trans* retinal converts back into the *cis* form through a series of enzyme-catalysed reactions. It bonds to an opsin molecule and the process starts all over again [8, 9].

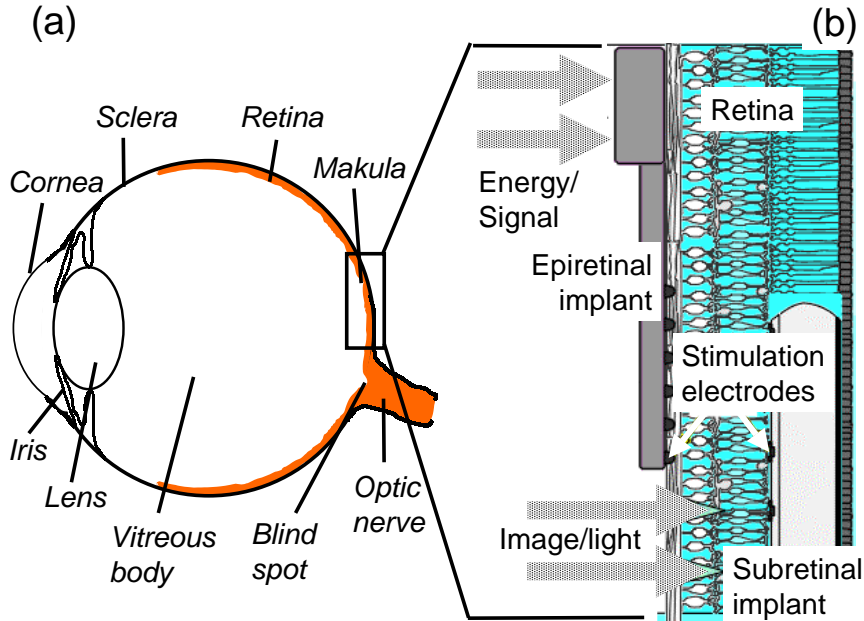


Figure 1.1: Concepts of restoring vision when natural photoreceptor cells are degenerated. (A) Cross section of a human eye. (B) Cross section of the retina. (i) Subretinal implant: A chip carrying an array of micro-photodiodes replaces the rods and cones of the outer retina. Each photodiode injects electric currents into the still functioning neural tissue of the inner retina layer. (ii) The epiretinal chip receives the image information from a camera which is carried outside the eye. The electrodes stimulate the axons of the ganglion cells that form the optic nerve (adapted from Stett, Zrenner [3, 4]).

Diseases such as Retina Pigmentosa (RP) and Age related Macula Degeneration (AMD) cause the photoreceptor layer of the retina to gradually degrade which eventually leads to complete blindness. Worldwide, roughly 1 to 3 million patients suffer from RP; in Germany alone approximately 30.000-40.000 people are affected [10]. Devices have been developed which (transiently) restore the sensation of light in patients, including a selenium cell placed behind the retina [11], and cortical implants of electrodes to stimulate the visual cortex [12, 13, 14, 15].

1.1.1 Concepts of retinal implants

Over the last few years, a number of research groups have started developing a prosthesis which could be directly implanted into the human retina [4, 16]. An acute stimulation of the human retina of RP patients is described

by Humayun [17, 18]. Figure 1.1 (b) depicts the two concepts for chronic implants. The subretinal approach [19, 20] aims at the direct functional replacement of the photoreceptor layer by a device that delivers electrical currents upon daylight illumination [3]. Figure 1.2 shows examples of the first generations of the subretinal implant chip, manufactured at the Institute for Microelectronics Stuttgart (IMS) and at the Natural and Medical Science Institute at the University of Tübingen (NMI). The devices consist of a *Micro-PhotoDiode Array* (MPDA) of several dozens to several thousands crystalline silicon based photodiodes (the size of the photodiodes varies between chip generations) [21]. Figure 1.2 (a) depicts the entire chip with a hole which enhances the flow of nutrients through the implanted chip to the underlying retina tissue. In Figure 1.2 (b), an enlarged part of the chip is shown and individual c-Si photodiodes and stimulation electrodes are distinguishable. The device is implanted in a way that the inner retina cell layers remain intact and come in close contact with the device's electrodes. See references [23, 24] for surgery methods. Kohler et al [25] presented a

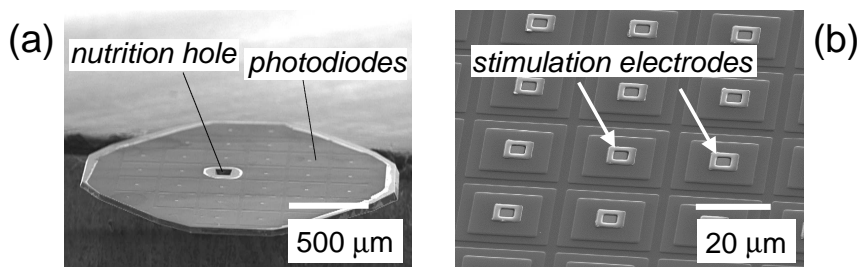


Figure 1.2: Scanning electron microscope views of sub-retinal implant chips. (a) The entire silicon chip is about 2 mm in diameter and 40 μm thin. The sharp edges are removed in a wet etch process to avoid injuries of the retina tissue during implantation. (b) Enlarged view: The chip consists of an array of individual crystalline silicon (c-Si) photodiodes, each featuring a stimulation electrode made from titanium nitride (adapted from [22]).

histological verification of the biocompatibility of the device following an implantation. With the epiretinal approach, an electrode array (which itself is not light-sensitive) is mounted onto the ganglion cells and directly stimulates their axons which form the optic nerve [26, 27, 28]. The epiretinal stimulation electrodes [29] are controlled by a camera and an image processing unit (including artificial neural networks [30, 31], both carried outside the human's body [32]). Subretinal- and epiretinal devices have been tested with animal models, see references [33, 34, 35] for Yucatan micropig, [36, 34] for chicken, [37, 34, 35] for rats, [24, 34, 38] for cats and [34, 33] for rabbits.

1.1.2 Stimulation of neural activity

Stett performs in-vitro experiments³ with rats' [37, 39] and chicken's retinae [36] to determine effective electrical stimulation patterns to initiate neural network activity. The stimulation threshold depends on the polarity of the electric pulses, the amplitude and the duration of time of application of the pulses, among other things. Generally, the injection of a stimulation charge $Q \approx 0.4$ nC per electrode into the distal retina site (ie. electrodes face the bipolar and horizontal cells) is sufficient to trigger ganglion cell responses⁴.

Stelzle [22] described a physical model for the stimulation of neural cells using photodiodes. Essentially, the subretinal device must provide for a (local) voltage drop associated with a stimulation current I_s across the tissue resistance R_t of the inner retinal layers. The device's metal electrodes are capacitively coupled to the electrolyte environment through the Helmholtz double layer capacitance C_{HH} . When light is switched on, the *micro-photodiodes* (MPD) charge the capacitance C_{HH} ⁵. The peak current at the beginning of the light pulse is determined by the current-voltage characteristics I/V of the MPD and the resistance R_t . The larger the interface capacitance C_{HH} at the stimulation electrode, the more charge Q , ($Q = \int I dt$), is transferred through the tissue before the electrode is fully polarized with the polarization voltage V_{ch} (i.e., the MPD reaches its open circuit voltage V_{oc}). Thus, the effective surface area of the stimulation electrodes should be maximised. In a sequence of light pulses, the forward and reverse currents across the retinal tissue as a result of the charging and discharging of the capacitance C_{HH} cancel one another (charge balanced pulses).

Silicon-to-neuron junctions were also developed by Fromherz, Stett and Braun [40, 41, 42]. In contrast to the silicon-metal-electrode-electrolyte interface described above, the capacitive coupling of single neurons to the silicon chip is achieved through a SiO_2 dielectric, thus avoiding any faradaic currents (see chapter 5.2.2) across the junction.

³While the initiation of inner retina layer activity is studied by research groups for both the epiretinal and subretinal devices, this paragraph focuses on experiments designed to emulate the subretinal stimulation by technical devices.

⁴In the experimental setup, living retinal tissue is placed onto a *MicroElectrode Array* (MEA) with the bipolar and horizontal cells facing the electrodes. The current injection pattern is determined by the choice of the stimulation electrodes on the array, the time-characteristics and amplitude of electric pulses. An extracellular Ag/AgCl glass-electrode serves to record the ganglion cell activity. In a different experiment, the MEA is replaced by the MPDA in order to test the performance of the chip implant. A light pattern is focused onto the chip through a microscope.

⁵Both Helmholtz capacitances, at the stimulation electrode and at the common counter electrode, are charged. Since $A_{se} \ll A_{ce}$, the time behavior of the current is determined by the stimulation electrode and C_{ce} is omitted in the following summary.

1.2 Encapsulation of a retina implant & Aim of this work

A retinal implant must have an encapsulation layer which serves two purposes:

(i) It prevents the direct contact of the surrounding tissue to the electrical components of the chip. Since several materials used in the device's manufacturing may not be biocompatible, it must also inhibit any leakage of chip components into the tissue. Naturally, the encapsulation layer itself must be *biocompatible*.

(ii) The encapsulation must protect the device against its biological environment. Not only is the device exposed to the biological media, but – as a foreign body – the implant faces immune response reactions of the organism [43]. Moreover, living cells that grow on the device's surface may lead to harsh and largely unknown chemical environments (eg. in presumed micro-volumina between the cell and the encapsulation layer) which may trigger or accelerate degradation processes of the implant.

Both aspects – the protection of the living tissue against chip materials and the protection of the chip against the biological environment – demonstrate the importance of an encapsulation (or passivation) material which is *biostable* over the intended lifespan of the implant of several years. Clearly, the long term biostability must be ensured before a chronic implantation of the device in a human being.

This work evaluates three biocompatible materials with regard to their overall long-term biostability. The candidates for a future retina implant encapsulation – $\text{SiO}_x\text{:C/SiN}_y$, dry-etch benzocyclobutene (BCB) and polyimide 2611 (PI) – have previously been suggested for medical applications. The verification of their biostability focuses on

(i) the chemical resistance against biological media,
 (ii) a low "diffusion" of surrounding media into the material which might negatively affect the adhesion of the encapsulation layer to the chip, and

(iii) available technologies to ensure "water-tight" sealing of the material's interface with the stimulation electrodes. In order to be able to detect *early stages* of changes at the polymers' surface, a process for the fabrication of ultra-thin samples with a thickness $d_{or} \approx 50$ nm is developed. Of the chosen analytical tools, X-ray photoelectron spectroscopy (XPS) is a highly surface sensitive measurement technique for the analysis of the chemistry of the sample layers. Volume- and surface sensitive Fast Fourier infrared spectroscopy (FTIR) complements the XPS analysis by providing absorption data of specific chemical bonds. The XPS- and FTIR data of the dielectrics are

interpreted based on literature spectra. Most research found in the literature focused on the materials' application as dielectrics, the mechanical stress and adhesion properties in multilayer systems, and (plasma-) surface modifications such as polishing or roughing. Moreover, polyimides, BCB and SiN_x layers have been employed as diffusion barriers against sodium and potassium ions and moisture in semiconductor industry. Stelzle [44] and Fromherz [45] observe the degradation of SiO_x layers after in-vivo and in-vitro contact with neural tissue, respectively. This study for the first time presents a XPS and FTIR analysis of the materials after exposure to cell culture media in order to explore the bio-chemical degradation mechanism. Apart from chemical degradation, the structural integrity of the test layers as well as the water uptake of the material affect the long-term biostability of the implant device. Impedance spectroscopy as the third main experimental technique reveals the electrical behavior of the dielectric encapsulation layers. Thus a higher limit for the density of pin holes is determined and water (dipole-) molecules are observed as they enter polymer surface regions. Based on a physical model for the polyimide layer, this work develops an electric equivalent circuit for the PI-electrolyte system in the frequency range $f = 10^{-3} \dots 10^7$ Hz. This work concludes with a ranking of the three materials in terms of their suitability for the long-term biostable encapsulation of a retina implant.

1.3 Organization

Chapter 2 presents prototypes of amorphous silicon based micro-photodiodes that are designed and manufactured in this work for the in-vitro stimulation of retinal tissue. Following a brief characterization of amorphous silicon, the fabrication process is described and current/voltage characteristics are given. The device cannot be applied to living tissue, however, because the low-temperature SiN_x encapsulation layer does not withstand the electrolyte environment.

Chapter 3 first summarizes the current status of the encapsulation of in-vivo retinal implants. Pit corrosion and gradual dissolving of SiO_2 demonstrate the importance of research focused on alternative encapsulation materials and technologies. Among those new materials, this thesis concentrates on $\text{SiO}_x\text{:C/SiN}_y$ and two polymers which are presented in the remainder of the chapter.

The analytical measurements to explore the biostability of encapsulation layers require a size $A_s \geq 8 \times 8 \text{ mm}^2$ of the test samples. Hence not all specimens can be evaluated in in-vivo trials. In order to partly simulate the in-vivo conditions of animal tests, this work devises in-vitro cell culture

experiments with tumor celllines which are presented in chapter 4.

After the cell culture tests, the encapsulation test samples are analysed using bulk- and surface- sensitive measurement techniques. Chapter 5 introduces to impedance spectroscopy as a means of observing the electronic behavior of the encapsulation candidates. Infrared spectroscopy and XPS serve to explore changes in the bulk and surface chemistry of the samples. After an introduction into both complementary techniques, the effects of X-ray radiation damage in the polymers for the interpretation of XPS spectra are analysed (chapter 5.4.2).

Chapter 6 presents the main experimental results of this work. At the outset, a detailed list of the examined samples demonstrates the high reproducibility of the XPS- and FTIR analysis following the cell culture treatments. The observed alterations of the surface chemistry lead to a model for the progressive SiN_x degradation. For the first time, a dissolution rate dss for SiN_x in biological growing media is given with $dss \approx 1 \dots 2 \text{ nm d}^{-1}$. The evaluation of the FTIR and XPS spectra for the polymers reveals the superior biostability of the polyimide samples. A XPS water rinse experiment is performed to explore the effects of potential "surface contamination" of polyimide test samples through cell culture residues. The time-series of XPS spectra support the model of a evolving polyimide-electrolyte interface region where cell culture media residues are embedded into the PI's (BPDA /- PPD) matrix. Subsequently, impedance spectroscopy serves to analyse the electronic behavior of hot-oven sterilized polyimide samples which are exposed to an electrolyte. Based on a physical model of the polyimide layer with a columnar-like bulk structure and a high surface roughness, this work develops an electric equivalent circuit for the PI-electrolyte system in the frequency range $f = 10^{-3} \dots 10^7 \text{ Hz}$. In agreement with the XPS analysis, numerical fits of the impedance spectra indicate a diffusion-like process of electrolyte components into a evolving surface layer of the material.

The summary of this work presents a ranking of the $\text{SiO}_x:\text{C}/\text{SiN}_y$, BCB and polyimide 2611 with regard to their overall suitability as an encapsulation layer for a future retina implant and points to unresolved issues which need further investigation.

Chapter 2

Thin-film micro-photodiodes for retina stimulation

This chapter serves two purposes: (i) It demonstrates the feasibility of amorphous silicon based micro-photodiodes with a high output voltage for the in-vitro stimulation of neural tissue and (ii) it motivates the search for biostable, low-temperature deposited encapsulation layers.

*(i) As outlined in chapter 1.1.2, the stimulation of neural activity depends on the charge transfer through the neural tissue. As the implant's electrodes are capacitively coupled to the neural tissue, the charge transfer is maximized by increasing the interface capacitance C_{HH} of the Helmholtz double layer and by increasing the output voltage of the photodiodes. Previous generations of subretinal implants consisted of an array of single *c*-Si photodiodes which reach an open circuit voltage $V_{oc} \approx 0.6$ V. In order to test neural stimulation with higher voltages, amorphous silicon (*a*-Si:H) based micro-photodiodes (MPDs) with $V_{oc} \approx 2$ V are designed in this work: Section 2.1 summarizes amorphous silicon basics. The following sections 2.2 and 2.3 describe the design of *a*-Si:H micro-photodiodes and the fabrication steps of prototypes of 2×4 MPD arrays, respectively. Finally, section 2.4 presents the standard I/V characteristics of the device in a dry environment.*

*(ii) The above described *a*-Si:H MPD arrays are also tested in an electrolyte environment, section 2.4.1. Here, the low-temperature SiN_x encapsulation layer proves an insufficient protection which underlines the importance of research on new encapsulation materials and -designs.*

2.1 Amorphous silicon basics

The following description is taken from standard semiconductor and solid-state textbooks: Street [46], Lucovsky [47], Ashcroft & Mermin [48] and Fonash [49]. Amorphous silicon exhibits only a short range order between neighboring Si-atoms. The high absorption coefficient in the visible spectral range as well as the higher band gap are the consequence of the absence of long-range order within the a-Si:H material. In contrast to the diamond-like unit cell which describes the Si-crystal including bond angles and mean atomic distances, the Si atoms in a-Si:H form a network with a distribution of angles between Si-Si bonds [50], a wider spectrum of atomic distances and many Si valence electrons that do not form all four covalent bonds with neighboring Si atoms but instead exhibit a so called "dangling bond" [51, 52]. Most device-quality a-Si contains hydrogen which saturates many of these dangling bonds [53, 54].

In crystalline silicon (c-Si), the absorption of a photon which provides the energy for the excitation of an electron from the valence to the lowest conduction band is a three particle process. During excitation, the electron changes its momentum and must therefore interact with a phonon (which supplies that momentum) in order to keep their overall momentum constant. In a-Si, the distribution of Si-Si neighbor arrangements (see above) means, that there is no $E = E(\mathbf{k})$ relationship for the electrons in the entire material¹. By the same token, there is no unique dispersion relationship between the energy of a permitted phonon, $E_p = \hbar\omega$, (ω = the angular frequency) and the wave vector \mathbf{k} of the vibration mode, $E_p = E_p(\mathbf{k})$, either. As a consequence, the momentum conservation laws for the absorption of an photon are somewhat relaxed. Thus, the amorphous material is termed a quasi-direct semiconductor in analogy to crystalline semiconductors. The quasi-direct character of a-Si:H leads to a 20 to 30 times higher light absorption than crystalline silicon. Consequently, one can deposit very thin photodiodes (several hundred nm thin) and potentially use flexible polymer substrates. The latter argument also depends on the technology to grow high-quality a-Si:H layers at relatively low temperatures, as will be shown in the following section. Moreover, with a typical a-Si:H bandgap² $E_g \approx 1.8$ eV, a-Si:H based photodiodes reach open-circuit voltages $V_{(a-Si),oc} = 0.8 \dots 1$ V compared with $V_{(c-Si),oc} \approx 0.6$ V for their c-Si counterparts.

¹Since there is no crystal, a-Si:H does not feature a Brillouin zone (defined as the unit cell of the reciprocal lattice, i.e., the lattice in the k space).

²Street [55] and Goldstein [56] describe the energy distribution of the density of states for a-Si:H. Tauc [57] formulates a mathematical expression for the optical band gap of a-Si:H material.

The next section builds on the main advantages of the a-Si:H material – (i) low temperature thin film deposition and (ii) high open circuit voltage – and present a new design of a-Si:H MPDs for experiments to explore effective electrical stimulation patterns for retinal tissue³.

2.2 Photodiode design

This section presents a prototype of a 4×2 array of novel thin film a-Si:H-based micro-photodiodes which is designed and manufactured in this work for in-vitro stimulation tests of retinal tissue [59]⁴.

Previous work on a-Si:H photodiodes focused mostly on the "conventional" a-Si:H growth process at temperatures above $T_{(a-Si),d} = 200^\circ\text{C}$. Yang [60] achieved world record stable efficiencies of $\eta_{a-Si} = 13\%$ for n-p-n-i-p triple cells deposited at $T_{(a-Si),d} = 220^\circ\text{C}$ (stainless steel-TCO-nipnip(a-SiGe)nip(a-Si)-TCO-structure). Conde et al [61] and Koch et al [62] pioneered a-Si:H layers and a-Si:H solar cells at $T_{(a-Si),d} = 45 \dots 100^\circ\text{C}$ for large scale applications on plastic substrates. For an earlier design for an a-Si:H based retina implant, see Schubert [63]. This work presents the first micro-patterned array of high output voltage a-Si:H photodiodes which are deposited at $T_{(a-Si),d} = 100 \dots 150^\circ\text{C}$.

The design of the chip focuses on the following biological requirements and physical / electrical challenges.

(i) High output voltage. As mentioned in chapter 1.1.2, the stimulated ganglion cell activity depends on the amplitude and time characteristics of the current which is injected by a subretinal device (resulting in a stimulation threshold expressed as the minimum charge transfer, $Q = \int I dt$, necessary to evoke neural activity). The current amplitude I is determined by the load resistance R_t of the electrolyte and the retinal tissue (which is either a fixed parameter, or difficult to control), the electrode polarisation V_{ch} (con-

³Moreover, a-Si:H based micro-photodiodes can be fitted quickly with a variety of stimulation electrode sizes (i) and -materials (ii): (i) The charge *density* which is injected into the tissue can be altered using a variety of "geometric sizes" of the electrodes. (ii) In order to minimize electrode charging during a light pulse of a given amount of time, the electrode's effective surface area should be maximized. Sputtered TiN features a fractal internal morphology and is now preferred to the conventional Au material. Alternatives include iridium oxide [58], among others.

⁴Parallel to the presented a-Si:H based device, project partners at the IMS and at the NMI develop a new CMOS process for a new c-Si subret implant chip. Here, each stimulation electrode is connected to four laterally series connected c-Si photodiodes in order to obtain $V_{oc} \approx 2 V$. The characteristics of the chip will soon be published by the IMS and NMI.

Table 2.1: *Prototypes of thin film micro-photodiodes based on low-temperature amorphous silicon, designed and manufactured in this work.*

MPD type	a-Si:H diodes	Deposition temperature	MPD dimensions
A	nip	150°C	690 x 690 μm^2 , 1x1 mm ²
B	nipnip	100°C	690 x 690 μm^2 , 1x1 mm ²

trolled by the state of *charging* of the Helmholtz capacitance) and by the I/V characteristics of the MPD [22]:

$$I = \frac{V_{MPD}(I) - V_{ch}}{R_t}. \quad (2.1)$$

In an attempt to increase the output voltage V_{MPD} , single and tandem a-Si:H photodiodes (nip or nipnip) are laterally series connected.

(ii) Low deposition temperature. A process temperature of below 150°C facilitates the use of polymer substrates or even bioresolvable polylactate foils. Ultrathin flexible devices would reduce the impact of a future device in the subretinal space [64].

(iii) Micro-patterning. The process design must include the micro-patterning of the chip in order to obtain an array of individual photodiodes.

(iv) Protection against electrolyte environment. A low-temperature deposited encapsulation layer must seal the device against the environment.

Table 2.1 lists the two types of micro-photodiodes along with the layer sequence, deposition temperature and geometric size, that are designed and fabricated in this work. Two laterally series-connected n-i-p diodes (deposition temperature $T_{(a-Si),d} = 150^\circ\text{C}$) form the type (A) MPDs. The photodiodes of the type (B) MPD are themselves stacked nipnip cells ("tandem cells")⁵, $T_{(a-Si),d} = 100^\circ\text{C}$).

Figure 2.1 shows the common design of type (A) and (B) MPDs prior to the deposition of the encapsulation layer and the stimulation electrodes. Figure 2.1 (a) shows an optical microscope view of an array of four MPDs (the depicted MPDs are part of a 4×2 MPDA). Each MPD consists of a central square a-Si:H cell and a surrounding outer photodiode. The outer and the inner photodiodes have the same area size to achieve an optimal current match. Figure 2.1 (b) depicts the upper left corner of a laterally series-connected MPD. The back contact (Cr) as well as the areas of the

⁵For a description of the working principles of nip and n-i-p-n-i-p a-Si:H based photodiodes see references [65, 66, 67, 68]

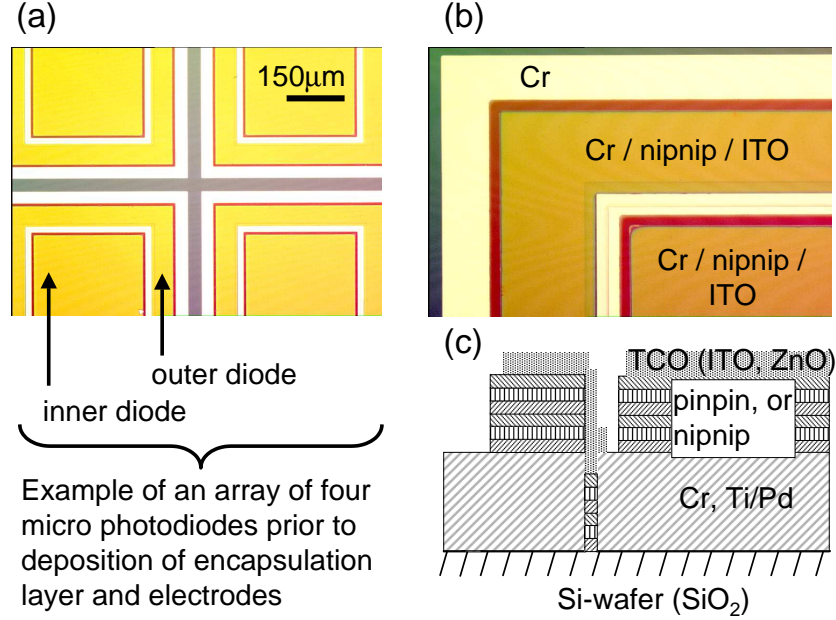


Figure 2.1: Micro-photodiodes, designed and manufactured in this work, consisting of two a-Si:H nipnip-structures which are laterally series connected. (a) Top view of four laterally series-connected a-Si:H tandem cells, compare with c-Si MPDA in Figure 1.2 (b). (b) Enlarged part of the upper left corner of a MPD. (c) Cross section of the MPD, corresponding to the part shown in (b).

single nipnip photodiodes are indicated. In Figure 2.1 (c), a schematic view of the cross section of the device is presented. The part shown corresponds to Figure 2.1 (b).

In the tandem structure of MPD type B, most light in the blue spectral range is absorbed in the top cell. As a result of the decreasing absorption coefficient of a-Si:H towards longer wavelengths (the external quantum efficiency decreases rapidly above $\lambda_l \approx 600$ nm), incoming "redish" light penetrates deeper into the material and contributes to the carrier generation in the bottom cell. For the same reason, the i-layer of the bottom cell is approximately three times as thick as the i-layer of the top cell⁶. Light that reaches the back contact is reflected back into the device.

⁶This is an optimization between the demand for high absorption even in the redish spectral range and the requirement, that the generated electron-hole-pairs actually make it to the doped layers of the bottom cell.

2.2.1 The size of micro-photodiodes & achievable resolution

Naturally, the design of a chip implant should aim at restoring the highest possible visual resolution. The size of the individual photodiodes as well as the size of the electrodes limit the spatial resolution that can be achieved with an implant (rods and cones are several μm in diameter) [4]. In in-vitro tests as well, a stimulation chip should have a sufficient number of individual MPDs to trigger spatially ordered ganglion cell activity upon stimulation by specific light patterns. Apart from technological reasons, however, there is an – yet unknown – upper limit N to the useful number of individual MPDs per chip⁷: The higher the MPD density, the lower the local charge density which is injected into the tissue in the vicinity of each stimulation electrode. At some point, a small individual photodiode becomes insufficient to elicit local neural activity. Thus a large number of photodiodes might actually lead to a sort of global stimulation of the tissue facing the chip and the detection of the above mentioned spatially ordered ganglion cell activity would be difficult. Since N is not precisely known yet (it is the goal of in-vitro tests to find out the exact stimulation parameters), it is reasonable to start with larger photodiodes, see "MPD dimensions" in Table 2.1.

2.3 Fabrication steps

Figure 2.2 outlines the fabrication sequence for the micro-photodiodes. Partly based on standard thin-film deposition techniques, photolithography- and etching procedures, the technological process was developed in this work. After the evaporation and patterning of the Cr- or Ti/Pd - back contact, the a-Si:H cells are grown in a three-chamber ultra-high-vacuum system using plasma enhanced chemical vapor deposition (PECVD) with the feedstock gases SiH_4 , PH_4 , B_2H_6 and H_2 [69]. All doped layers are approximately 15 nm thick. The intrinsic layers (i-layers) of the type (B) MPDs, $T_{(a-si),d} = 100^\circ\text{C}$, are deposited with a hydrogen dilution of $r_H [(\text{SiH}_4 + \text{H}_2) / \text{SiH}_4] \approx 10$ [70, 71, 72]. Both i-layers exhibit the same band gap $E_g \approx 1.8$ eV (i.e., no methane is added to optimize the bandgap of the bottom cell). No hydrogen is added during the deposition of the type (A) MPDs. Reactive ion etching (RIE) using SF_6 or CF_4 is the favored method for patterning the a-Si:H

⁷Only a qualitative argument can be given, as there are ongoing in-vitro and in-vivo experiments to explore efficient electrical stimulation patterns of the retina, see also chapter 1.1.2.

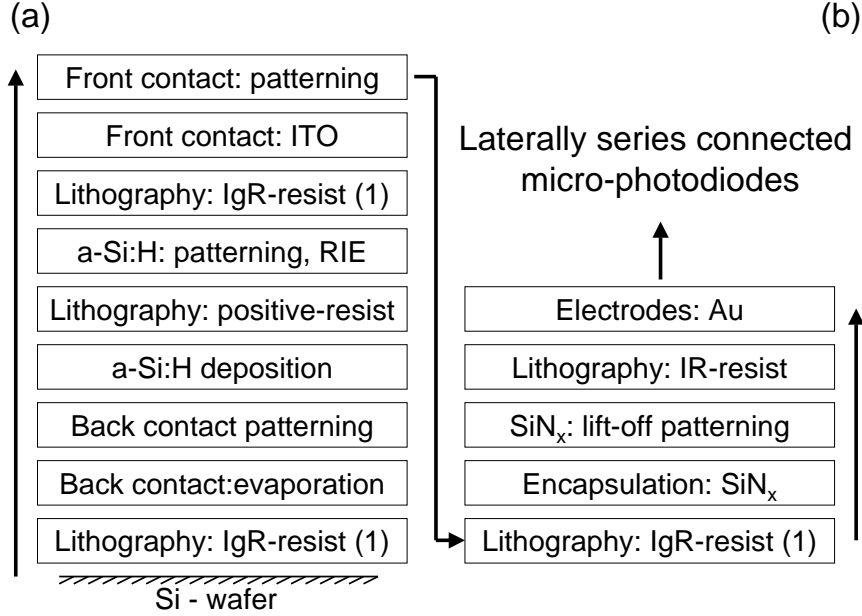


Figure 2.2: Process sequence which is developed in this work for thin-film MPDAs for retina stimulation. (a) A series of deposition processes forms two laterally series connected a-Si:H cells. Image reversal (IgR) lithography serves to pattern the back contact and the front contact in a lift-off procedure. Positive resist lithography provides the mask for the RIE etching of the a-Si:H layers. (b) Patterning of the encapsulation layer and the stimulation electrodes. (1) The lift-off technique may be replaced by etching, switching from IgR lithography to positive photoresist.

absorber⁸ [73]. For a discussion of plasma-etch mechanisms see reference [74]; for a survey of RIE applications to Si see reference [75]. Although low-temperature a-Si:H deposited at $T_{(a-Si),d} = 100^\circ\text{C}$ is suitable for the lift-off technique [76], lift-off results in a reduced geometric accuracy of the device compared to the RIE etch process. Sputtered Indium-tin-oxide (ITO) serves as the front contact of the photodiodes [77]. Alternatively, sputtered Al-doped ZnO which is embedded into two thin intrinsic ZnO layers can be used as the front contact material⁹. The 200 nm thick SiN_x encapsulation layer is deposited in a PECVD process using SiH₄, N₂ and H₂ as the feedstock gases.

⁸The RIE etching of the a-Si:H material was performed with the help of J. Egelhaaf at the Institute for Systems Theory and Display Technology (LfB).

⁹ITO and ZnO are the most commonly used front contact materials within the group of *Transparent Conductive Oxides* – TCO.

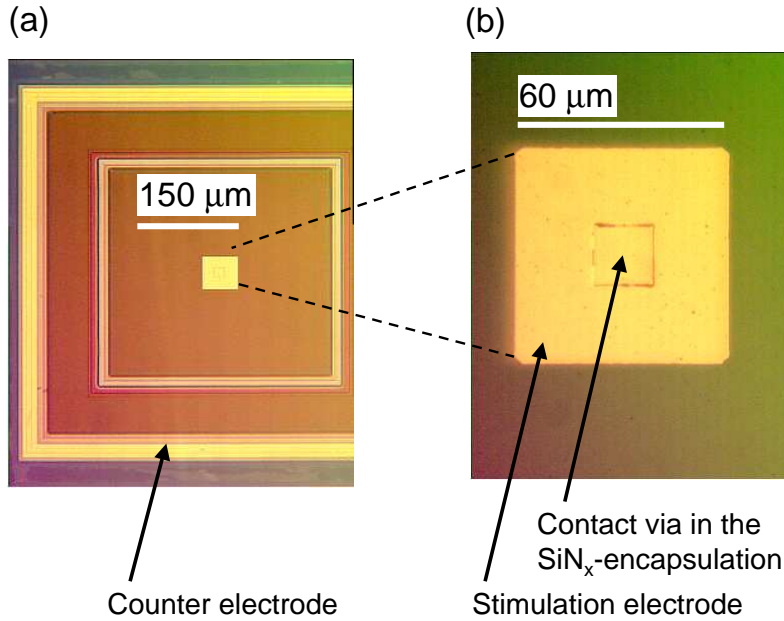


Figure 2.3: Example of a complete MPD including the SiN_x encapsulation layer and the Au- stimulation electrodes. (a) The outer counter electrode connects to the back contact of the outer nipnip photodiode. (b) The inner central electrode (=stimulation electrode) is evaporated onto the front contact of the inner photodiode. Both electrodes overlap the contact vias in the PECVD- SiN_x encapsulation layer.

The deposition temperature is limited to that of the a-Si:H layers. Lastly, the Au electrodes are evaporated and patterned in a lift-off process.

Figure 2.3 (a) shows an example of a complete MPD including the SiN_x encapsulation layer and the Au stimulation electrodes. The stimulation electrode as well as the counter electrode face the inner retina layer in the in-vitro experiments¹⁰. The outer ring electrode (=counter electrode) connects to the back contact of the outer nipnip (nip-) photodiode. Figure 2.3 (b) depicts the central stimulation electrode with an area $A_{se} = 60 \times 60 \mu\text{m}^2$ which is evaporated onto the front contact (i.e. the ITO layer) of the inner photodiode. Clearly visible is the contact via in the PECVD – SiN_x passivation layer with an area $A_{cv} = 20 \times 20 \mu\text{m}^2$.

¹⁰Such a design is referred to as "bipolar" in contrast to the "unipolar" configuration, where the counter electrode sits at the opposite side of the chip. Both designs have been tested with c-Si MPDAs. The current chip generation is of the bipolar type.

2.4 Current-voltage measurements

In a first step, the standard current / voltage characteristics of the thin-film MPDs are recorded. A Karl Suss Analytical Probe System facilitates the contacting of the Au electrodes with microprobe needles. The microscope lamp serves as the light source. By approximation, the spectrum of the halogen lamp is a 3000 K black body radiation. The higher reflectivity of the lamp's reflector for shorter (bluish) wavelengths results in a shift of the spectrum's maximum from $\lambda_{max} \approx 970$ nm ($\lambda_{max} = 2.898 \times 10^{-3}$ m K / 3000 K) towards ≈ 600 nm, though the exact value is unknown¹¹. The light intensity of the microscope lamp is below 100 W m^{-2} .

Figure 2.4 shows the I/V curve for an MPD of type (B) consisting of two laterally series-connected nipnip tandem cells. The general equation for a photodiode,

$$I = I_0 \left(\exp \left\{ \frac{q(V - IR_s)}{nkT} \right\} - 1 \right) - I_{sc} + \frac{V - IR_s}{R_p}, \quad (2.2)$$

includes the series resistance R_s and the shunt resistance R_p of the photodiode's equivalent circuit¹². I_0 is the saturation current, q the elementary charge, k the Boltzmann constant, T the absolute temperature and n the (phenomenological) ideality factor. The algorithm developed by Werner [79] yields a parallel (or shunt-) resistance $R_p \approx 1.2 \times 10^4 \Omega \text{ cm}$. A numerical fit of the I/V data with equation 2.2 ($n = 8$, $I_0 = 6 \times 10^{-6} \text{ mA cm}^{-2}$, $I_{sc} = 0.72 \text{ mA cm}^{-2}$) gives for the series resistance $R_s \approx 1 \times 10^3 \Omega$. Thus, the shunt resistance R_p is 1 to 2 orders of magnitude lower than that of a typical non-patterned laboratory a-Si:H cell [67]. The series resistance R_s is about three orders of magnitude higher than that of the above mentioned typical cell [80].

The open circuit voltage as well as the short circuit current are mostly determined by the amorphous silicon material's properties and the a-Si:H deposition parameters. In contrast, the design of the MPD and the processing steps have a large effect on the shunt- and series resistance of the device.

¹¹The manufacturer does not give further spectral information and no spectrum was recorded from that specific lamp.

¹²The I/V characteristics are recorded with a two contacts measurement setup. Hence, the series resistance of the cable and of the needle – device contacts show up in the curves. Such series resistances would be excluded in a four-point setup, where the current passes through two points on the probe and the voltage between the second pair of contacts is measured [78]. However, as $R_{(a-Si),s}$ is usually larger than the "external" series resistances, the two point setup does give an accurate I/V characteristic.

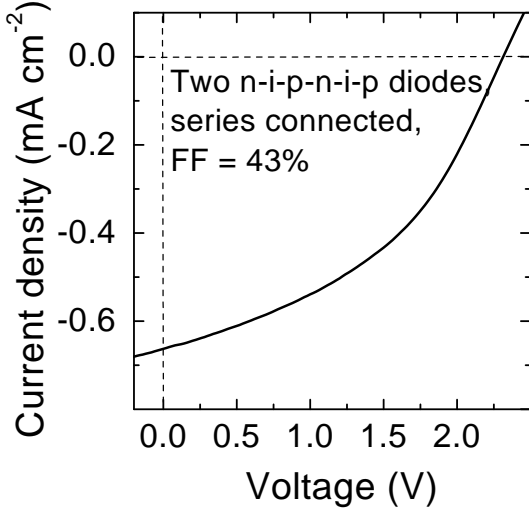


Figure 2.4: Current-voltage characteristics of prototypes of micro-photodiodes based on low-temperature amorphous silicon. MPD type (B) consists of two stacks of nipnip diodes which are laterally series-connected, reaching an open circuit voltage of $V = 2.3$ V.

Both, R_s and R_p , largely determine the fill factor FF defined as

$$FF = \frac{V_{mpp} I_{mpp}}{V_{oc} I_{sc}}, \quad (2.3)$$

with the voltage and current at the point of maximum power output V_{mpp} and I_{mpp} , respectively, the open circuit voltage V_{oc} and the short circuit current I_{sc} .

The low shunt resistance is most likely caused by pin-holes in the a-Si:H layers and small holes and spikes in the evaporated Cr-back contact¹³. As the subsequently deposited a-Si:H layers form around these shapes, small-scale back-to-surface short circuits remain which lower the overall shunt resistance. The high series resistance of the device points to a low conductivity of the doped layers. The low current density is the result of the low external quantum efficiency of the a-Si:H cell above $\lambda_l \approx 600$ nm. The spectrum of the employed halogen microscope lamp with $\lambda_{max} \approx 600$ nm (see the beginning of this section) is insufficient for a-Si:H cell illumination. A mercury lamp with several emission lines in the ultraviolet and blue spectrum [81] should be added to the I/V recording setup to better simulate a solar-like spectrum.

Experiments by Koch [82] showed that the annealing (in ambient atmosphere at a temperature T_{an} , $T_{an} > T_{(a-Si),d}$) of low-temperature deposited a-Si:H solar cells enhances the fill factor and short circuit current of the devices. Here, neither annealing is attempted¹⁴, nor the reverse bias "burn

¹³The evaporation system used produces high variations in the evaporation rate. A switch to a sputtered material would much enhance the homogeneity of the back contact.

¹⁴Basically, the annealing at elevated temperatures supports thermally activated processes in a-Si:H, such as the break up and re-formation of covalent bonds. The density of localized energy states which provide the main recombination pathway is reduced. How-

out” of leakage current paths which might enhance the shunt resistance of the MPD.

2.4.1 Failure of conventional low-temperature deposited SiN_x encapsulation

In order to record the performance of a-Si:H MPDs in an electrolyte environment, the ”micro-droplet contacting method” developed by Stelzle [22] is employed at the Institute of Natural and Medical Sciences at the University of Tübingen (NMI)¹⁵. A droplet of physiological sodium chloride solution (*Phosphate buffered Saline*, PbS, see Appendix 7.1), is placed onto a MPD stimulation electrode and contacted with an Ag/AgCl electrode in a pipette. A pulsed halogen lamp (using a chopper) illuminates the MPD.

Within minutes, before a light-pulse– electric current pattern is recorded on the computer, the stimulation electrode is damaged as shown in Figure 2.5 (a). Although the PbS- droplet covered almost the entire inner a-Si:H cell, most damage occurs in the vicinity of the Au stimulation electrode. See Figure 2.3 (a) and (b) for comparison with the intact device. Figure 2.5 (b) depicts the schematic cross-section of the electrode on the MPD. As described in chapter 2.3, the SiN_x encapsulation layer is patterned to obtain a contact via for the electrode material. The electrolyte test reveals that the flanks of those contact holes are not sufficiently covered by the evaporated Cr-Au electrode. The electrolyte can thus leak underneath the SiN_x layer and reach the ITO which most likely starts electrolytic reactions caused by the potential difference to the Ag/AgCl electrode¹⁶. Moreover, the low-temperature PECVD-deposited SiN_x exhibits structural defects – pin holes – which result in similar reactions at the ITO-electrolyte interface.

The findings of the electrolyte experiment with the a-Si:H MPD underlines the importance of a new encapsulation design and new materials. A sputter process for the deposition of the electrode material improves the homogeneity of the layer, particularly at the SiN_x flanks of the contact via (In a plasma sputter process, the movement of the atoms from the target to the

ever, at temperatures higher than $T_{(a-Si),d}$, the hydrogen content in the material decreases which counteracts the desired reduction in the density of dangling bonds. Thus, the annealing process has to be optimized for any given set of a-Si:H deposition parameters [83].

¹⁵The micro-droplet contacting experiment was performed by Dr. M. Stelzle.

¹⁶The experiment was performed under ambient light conditions, i.e., the chopped halogen light added to a constant illumination $D \approx 10 \dots 30 \text{ Wm}^{-2}$. Assuming a capacitance of the solid-electrolyte interface of the order of $C_{HH} \approx 1 \times 10^{-7} \text{ F}$ and a photo-generated current (under ambient light) $I_{ph} \approx 1 \times 10^{-8} \text{ A}$, the potential between the stimulation electrode and the Ag/AgCl counter-electrode reaches $V_{se-ce} = 1 \text{ V}$ within seconds.

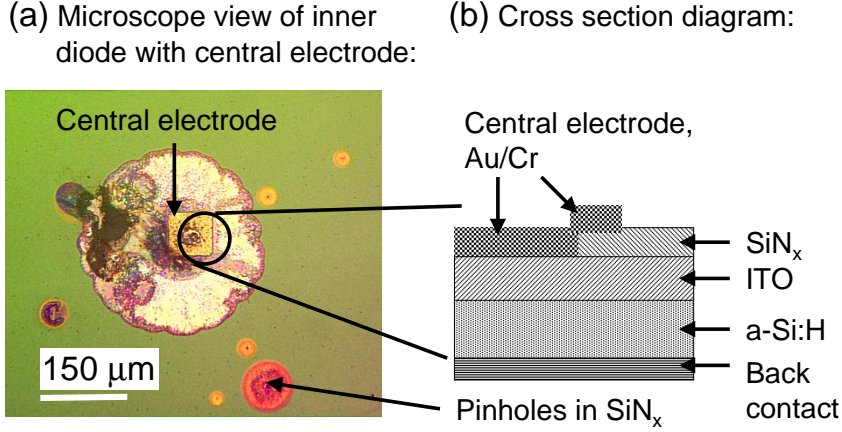


Figure 2.5: The central stimulation electrode of one micro-photodiode after current injection into an electrolyte environment. (a) Optical microscope view showing the heavily damaged vicinity of the central stimulation electrode and a number of pinholes in the SiN_x encapsulation layer, compare with Figure 2.3 (a) and (b). The PbS droplet which covered the entire area in order to contact the electrode was removed with N₂ before the recording of the picture. (b) Schematic diagram of the cross section of the device. The buffer solution reaches the ITO layer at the edges of the contact via in the SiN_x layer as well as through pinholes in the PECVD SiN_x layer.

substrate is far less directional than that of thermally evaporated atoms.). The micro-patterning must be optimized to yield positive flanks, see chapter 3.3. Moreover, research must focus on alternative materials – biocompatible, transparent, pin-hole free, compatible with micro-patterning techniques – to ensure the long-term biostability of the implant. In the following chapters, after an analysis of the currently used "high temperature" SiO₂ encapsulation material, sputtered SiO_x:C/SiN_y and two organic polymers will be evaluated as new coatings for a retina implant. The deposition and curing temperatures of the SiO_x:C/SiN_x and the Benzocyclobutene (BCB) are compatible with the fabrication of conventional thin film a-Si:H photodiodes at $T_{(a-Si),d} \leq 250^\circ\text{C}$. Taking advantage of the high glass transition temperature T_{gtt} of the biocompatible polyimide PI 2611, $T_{gtt} \approx 400^\circ\text{C}$ [84], a flexible [85] and biostable a-Si:H based MPDA might be feasible in the future [86, 87].

Chapter 3

Biostability of a Retina implant

The first section of this chapter demonstrates the inadequacy of today's SiO_2 to protect retina implants. In the following section, three alternative encapsulation materials are presented. The deposition process and chemistry of the layers are outlined. Finally, a new technological design opens the way for positive etch flanks in the encapsulation layer, thus facilitating a homogeneous coverage of the corrosion-sensitive electrode material-encapsulation layer interface.

3.1 Current status

The last chapter ended with a prototype device of micro-photodiodes which function in a dry environment, but do not withstand the electrolyte "attack". The current retina implant devices which are designed for implantation are based on crystalline silicon (c-Si), see Chapter 1.1.1, Figure 1.2. Their encapsulation layer SiO_2 is made from *tetra-ethyl-ortho-silicate* (TEOS) at a temperature $T_{(TEOS),d} \approx 300^\circ\text{C}$ [88]. The SiO_2 does not exhibit pin-holes and it is stable under most in-vitro conditions. However, after the explantation from rabbit's and pig's eyes, the scanning electron microscope (SEM) and energy dispersive X-ray diffraction (EDX) analysis of the surface reveals progressive degradation of the encapsulation layer as shown in Figure 3.1 (b) - (d) [44]. The upper parts of (a), (b) and (d) show optical microscope views of the (entire) chip. The lower parts of (a), (b) and (d) and all parts of (c) depict SEM recordings: (a) Three weeks after implantation, no morphological damage is visible in the SEM pictures. In the optical microscope view of the entire chip, the encapsulation layer appears in a homogeneous color, confirming the overall integrity of the chip. (b) Beginning after six month, the SiO_2 thickness decreases. In the light microscope, the originally

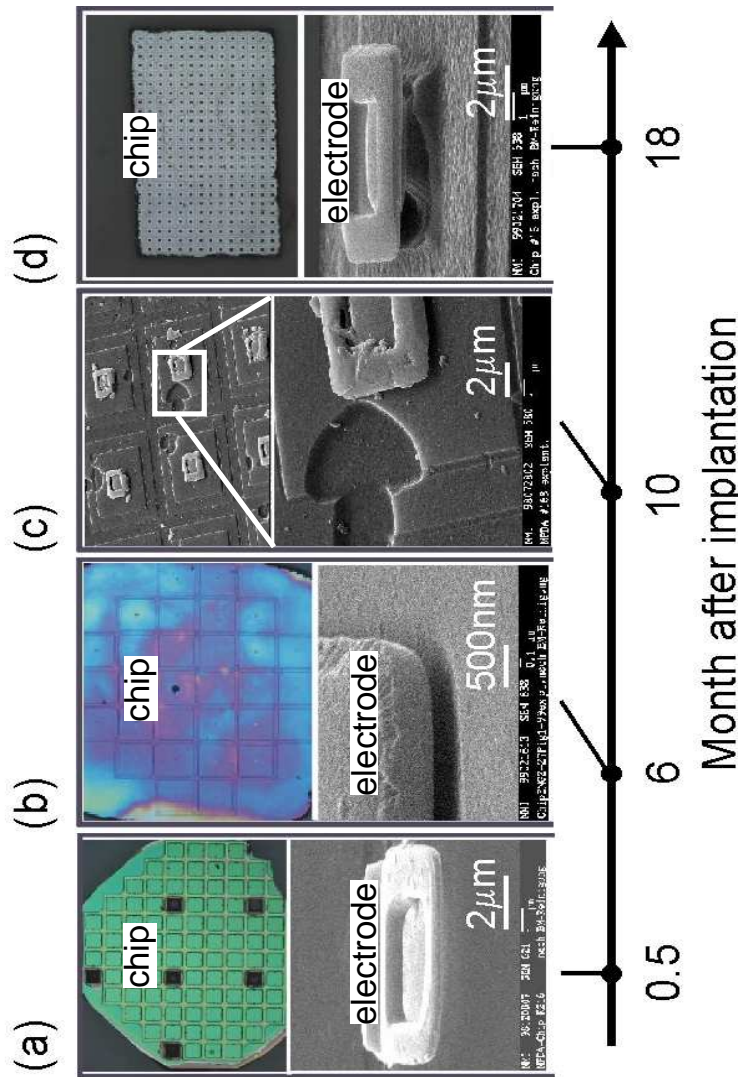


Figure 3.1: SEM (lower parts) and optical microscope (OM) views (upper parts) of MPDAs explanted from animals (adapted from Stelzle [44]). (a) MPDA explanted after three weeks. No morphological damage is observed. SEM shows the electrode embedded in the SiO_2 encapsulation. (b) After six month. SEM reveals a decreased thickness of the SiO_2 passivation. The OM shows a color (grey) gradient and a gap between the electrode and the encapsulation evolves. (c) After 10 month. SEM pictures show pit-corrosion in the passivation layer, compare with Figure 1.2 (b). (d) After 18 month. The passivation layer is completely removed. The originally embedded electrode stands out as an "island". Compare SEM views in (d) and (a).

homogeneous color of the passivation layer has changed and exhibits strong lateral variations on a typical length scale of 20 μm to 100 μm . Later on, after 10 month, pit-corrosion of the underlying Si photodiode is observed, Figure 3.1 (c). (d) Finally, after 18 month, the encapsulation is almost completely lost and the silicon shows general signs of progressive corrosion. In contrast to the SiO_2 , the TiN stimulation electrodes show no sign of morphological damage, indicating the biostability of the electrode material.

Fromherz [45] observed a similar degradation of SiO_2 layers after exposure to brain tissue. There, the SiO_2 serves as the gate dielectric of field effect transistors in an experimental setup to record neural cell action potentials [89, 90, 91]. The bio-chemical mechanisms which causes the degradation is largely unknown.

3.2 Novel encapsulation materials

As outlined in Chapter 1.2, the encapsulation layer of a retina implant serves two purposes: (i) It protects the surrounding tissue against inner components of the chip which may not be biocompatible. (ii) It protects the chip against its (aggressive) biological environment which would dissolve an uncoated silicon device.

The search for alternative encapsulation layers is based on decades of extensive research on implant materials [92]. Related issues include the immune response to silicone implants [43], the material technology [93] and the formation of biofilms [94] on hydrophilic and hydrophobic materials such as contact lenses [95, 96] and the intended biodegradation of polymers [97]. Among biodegradable polymers, poly(DL-lactic-co-glycolic acid) films are used as synthetic temporary substrates for retinal pigment epithelium cell cultures [98] and poly(anhydride-imides) are currently investigated for orthopedic applications [99]. Nafion (DuPont) perfluorosulphonic acid polymer (a close relative to Teflon) was found biocompatible and is being tested for biosensor applications [100].

In addition to the obvious requirement of biocompatibility – for which standardized tests are required (international standard "Biological Evaluation of Medical Devices", ISO 10993, and USP-23 [101, 102, 103, 104, 105]) –, the new materials for the light sensitive subret-chip must be transparent in the visible and near infrared range. Moreover, their deposition and patterning techniques must be compatible with the overall manufacturing of the device in a commercial CMOS-line of a chip fab.

The verification of the biostability of the novel materials focuses on (i) the chemical resistance against biological media, (ii) a low "diffusion" of sur-

rounding media into the material which might negatively affect the adhesion of the encapsulation layer to the chip, and (iii) available technologies to ensure "water-tight" sealing of the material's interface with the stimulation electrodes.

3.2.1 $\text{SiO}_x\text{:C/SiN}_y$

The first candidate for an improved implant encapsulation is a further development of the well known $\text{SiO}_x\text{:C}$ - and SiN_y - dielectrics. The sputter- and PECVD processes to grow dense layers with a very low pin-hole density for the $\text{SiO}_x\text{:C/SiN}_y$ sandwich structure were optimized by Bucher at the NMI¹ and by Vetter [106].

Besides its use as dielectric, the SiN_y serves to electronically passivate Si surfaces [107] and is employed as a diffusion barrier for water vapor [108] and ions such as sodium and potassium in semiconductor industry. Similarly, low-temperature $\text{SiC}_x\text{:H}$ layers are deposited for moisture and corrosion resistance [109]. In medical–engineering applications, this sandwich structure or very similar layers are used to protect micro-electrode arrays (MEAs) for the recording of nerve-cell signals at the *Natural and Medical Science Institute* at the University of Tübingen (NMI). The long-term survival of retinal cell cultures on Si_3N_4 - as well as on TEOS SiO_2 - layers was demonstrated [110].

Figure 3.2 displays the atomic configuration of the top SiN_x layer of the $\text{SiO}_x\text{:C/SiN}_y$ sample [111, 112]. XPS analysis in chapter 6.1.3 reveals an almost stoichiometric composition of the top SiN_x layer. (a) The 3-dimensional Si_3N_4 structure. Solid lines represent the covalent bonds. The ellipses designate parts of the structure which demonstrate the geometric arrangement of the atoms: The nitrogen atoms position themselves tetrahedrally around the silicon atom with an angle of about 109° between the N–Si covalent bonds, see Figure 3.2 (b). Similarly, the silicon atoms form a planar equilateral triangle with the N-atom at its center, shown in (c) [113]. Each Si atom forms four sp^3 hybrid orbitals which overlap with the three sp^2 orbitals of the N atoms, see reference [114]. The resulting covalent bonds are polarized due to the higher electronegativity of the Si. The formations of covalent bonds based on sp^3 and sp^2 hybrid orbitals results in a rigid Si_3N_4 structure (more rigid than SiO_2 , for instance) which is also harder and exhibits higher values of mechanical stress than SiO_2 . Though the material is amorphous it is very dense. As a direct consequence, Si_3N_4 exhibits a low diffusion coefficient for ions.

¹All $\text{SiO}_x\text{:C/SiN}_y$ test samples are prepared by V. Bucher at the NMI.

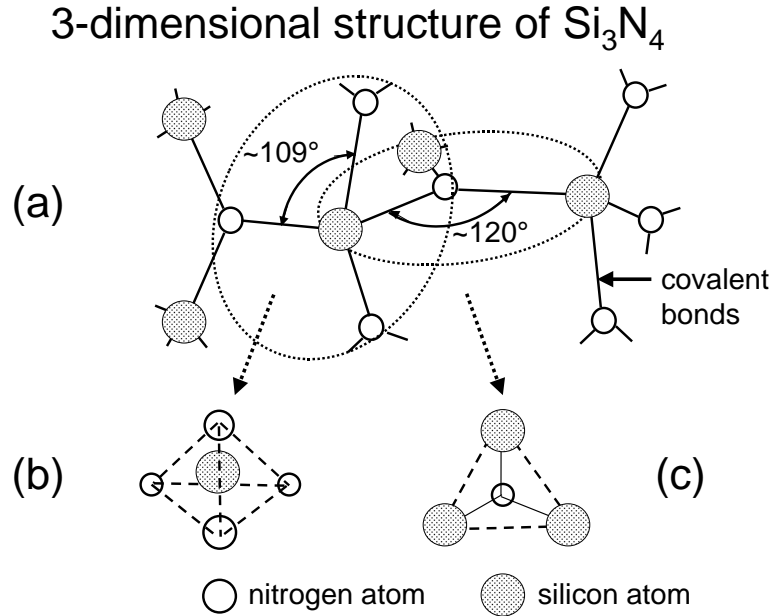


Figure 3.2: The atomic configuration of stoichiometric Si_3N_4 . Solid lines represent covalent bonds. (a) 3-dimensional structure. The approximate bond angles in the amorphous network are indicated. The dashed ellipses and arrows highlight the geometry of parts of the network: (b) The nitrogen atoms (open circles) are arranged tetrahedrally around the silicon atom (greyish patterned circles). The dashed lines emphasize the tetrahedral geometry. (c) From the perspective of the nitrogen atom, the silicon atoms sit at the vertices of a planar triangle centered around the nitrogen. Solid lines represent covalent bonds, dashed lines indicate the geometry.

Similar to the a-Si:H material described in chapter 2.1, the amorphous SiN_x exhibits a distribution of inter-atomic distances and binding angles. Thus, the SiN_x network exhibits a high density of bonds, particularly at the surface, which are energetically less stable than the ideal crystalline Si_3N_4 structure of Figure 3.2 suggests. The hydrogen content of PECVD-deposited SiN_x is typically much higher than that of the sputtered material [115]. Depending on the formation of Si-H or N-H bonds, the H-content may correlate with mechanical stress in the films [116, 117, 118, 115]. Moreover, the corrosion rates of SiN_x in "harsh environments" increase with increasing H-content [119]. The sputtered SiN_x used here does contain small amounts of hydrogen, as is evident in the N-H stretching bands in the FTIR spectra, see chapter 6.1.2.

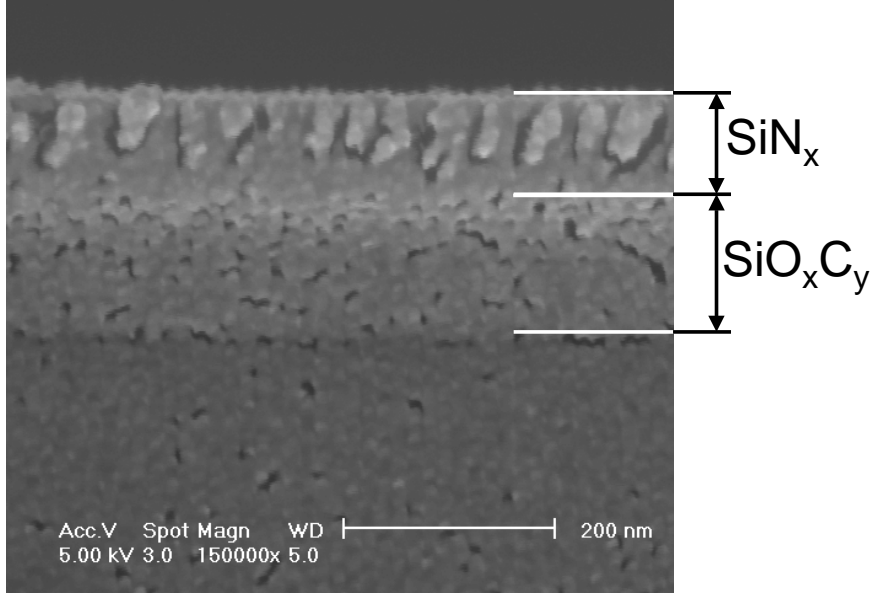


Figure 3.3: SEM cross section view of a $\text{SiO}_x\text{:C}/\text{SiN}_x$ sample.

This first study uses two different substrates: (i) Highly doped wafer, Wacker, (100), CZ, p-type, B-doped, resistivity $\rho_{(w),l} \geq 0.01 \Omega\text{cm}$ are employed for samples to be analysed with impedance spectroscopy. (ii) Both-side polished, high resistivity wafer, $\rho_{(w),h} \leq 10.000 \Omega \text{ cm}$, (111), FZ, p-type, B-doped, serve as the substrate material for samples for FTIR analysis. XPS is independent from the substrate material.

In a first step, following a cleaning (i.e. "etching") of the test sample wafer substrate in Ar atmosphere, the $\text{SiO}_x\text{:C}$ layer is deposited from Hexamethyldisiloxan (HMDSO) and O_2 in a PECVD system. In a second vacuum system (i.e., there is an air-break between the deposition of the $\text{SiO}_x\text{:C}$ and that of SiN_x), the samples are first cleaned again by short-time Ar sputtering. The subsequent sputter process using Ar and N_2 and a SiN sputter target gives the top SiN_x layer with a thickness $d_{\text{SiN}_x} \approx 100 \text{ nm}$. No chemical-mechanical polishing of $\text{SiO}_x\text{:C}/\text{SiN}_y$ test layers is performed [120].

Figure 3.3 shows a SEM cross section view of a $\text{SiO}_x\text{:C}/\text{SiN}_x$ test sample. Both dielectric layers are indicated. Between them, an interface zone is observable. The top layer exhibits column-like fragments which most likely result from the breaking of the material for the SEM cross-section recordings. SEM shows a total thickness d_{io} of the $\text{SiO}_x\text{:C}/\text{SiN}_x$ test samples of $d_{io} \approx 200 \text{ nm}$.

The meander-like "patterns" in the cross section view can be explained by the SEM preparation: After breaking the sample, the cross section is exposed to a short Au-sputtering to enhance the conductivity of the dielectric (Au deposition rate $r_{Au} \approx 1.5 \dots 3 \text{ \AA min}^{-1}$). The Au forms clusters [121, 122] which are also observed on BCB and polyimide samples. As artifacts of the Au sputtering, those "textures" do not indicate inhomogeneities in the respective dielectric.

3.2.1.1 Optimum thickness of $\text{SiO}_x\text{:C/SiN}_y$ test layers

In order to detect alterations of the SiN_x surface by way of transmission FTIR, the fraction between the affected surface region and the bulk material should be kept high. Differences in the surface chemistry between a reference sample and the test sample are simply more likely to be detectable if inevitable variations in the dielectrics' thickness, for example, do not overwhelm the sought-after effects. A thin test layer is therefore desirable.

The impedance spectroscopy technique yields results about the capacitive elements of the proposed equivalent circuit. In the experimental setups described in chapter 5.2, the thicker the $\text{SiO}_x\text{:C/SiN}_x$ dielectric, the lower the total capacitance of the system and the more difficult it is in the available frequency range to distinguish additional capacitive elements at the surface of the material. However, the pin-hole density increases with decreasing $\text{SiO}_x\text{:C/SiN}_x$ thickness which introduces "artificially" low shunt resistances of the dielectric. Thus, a balance with regard to the optimum thickness for the test samples must be found which is in any case lower than the thickness of the encapsulation of an actual implant device.

3.2.2 Benzocyclobutene – BCB

Dry-etch 3000 series *Benzocyclobutene* (BCB) from Dow Chemical are used in the electronics industry as passivation layers (moisture uptake $< 0.25 \%$ at 85 % relative humidity [123]) [124, 125], planarization layers [126, 127], dielectrics ($\epsilon_{r,BCB} = 2.65$) [128, 129, 130, 131, 132, 133, 134], optical interconnects [135, 136], among other applications. Although no standard ISO procedures (see polyimide section) are reported, preliminary cytotoxicity tests indicate the biocompatibility of the material [137, 138]. Moreover, in technological trials conducted during this work, positive etch flanks for stimulation electrode via are achieved, see chapter 3.3. Positive via flanks allow for a homogeneous coverage of the encapsulation material – electrode interface. Thus, the BCB dry-etch characteristics point to a promising long-term sealing of those parts of the device which have been particularly "corrosion"

sensitive in the current encapsulation regime.

BCB resins are derived from B-staged bisbenzocyclobutene monomers which are shown in Figure 3.4. The arrows indicate the main chemical bonds:

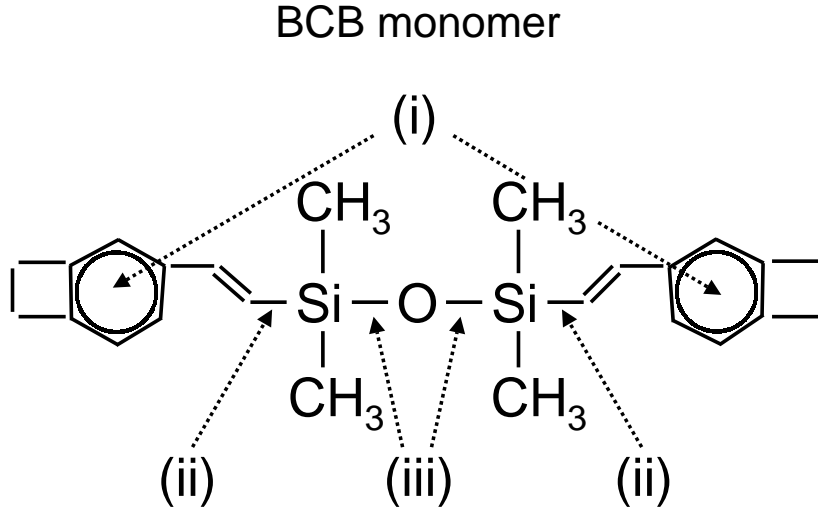


Figure 3.4: Structural formula of the BCB monomer. The arrows indicate the main chemical bonds between the carbon, silicon and oxygen: (i) C-C bonds. (ii) Si-C bonds. (iii) Si-O-Si ether group bonds. The polymer forms during the thermal curing through Diels-Alder polycondensation (not shown).

(i) "C-C" aromatic bonds, (ii) Si-C bonds, (iii) C-Si-O siloxan bonds. The BCB polymer forms by way of Diels-Alder polycondensation [139] during the thermal curing of the material (not shown).

After the application of the adhesion promoter AP8000 (3-aminopropyltriethoxysilane) [139], the solution of BCB in mesitylene is spin coated onto the wafer substrate². For an analysis of the spin-coating of polymer films including the planarization of uneven substrate topography see [140, 141, 142]. With the commercially available BCB-mesitylene solutions, a polymer thickness between $d_{(BCB),cm} \approx 1 \dots 25 \mu\text{m}$ is obtained, depending on the (final) rotations per minute (rpm) of the spin-dry process. For the cell-culture experiments in this work, samples with a much reduced film thickness are prepared, see section 3.2.4. All films are cured in a high vacuum ($p_{(BCB),c} \leq 1 \times 10^{-5}$ mbar) chamber with the identical final temperature

²In this work, the BCB is deposited at (i) the University of Kaiserslautern, Dept. of Physics, research group of Prof. Fouckhardt for integrated optoelectronics, with the help of S. Wolff and colleagues and (ii) at the Institute of Physical Electronics.

$T_{(BCB),c} \approx 250^\circ\text{C}$. The temperature ramp varied between the BCB deposition series which may result in variations of the surface roughness of the sample layers (yet no AFM measurements are conducted in this work).

BCB samples ($d_{(BCB),cm} \approx 5.5 \mu\text{m}$) for implantation in rabbit's eyes at the University of Regensburg by Kobuch and subcutaneous implantation in rats (BSL Bioservice Scientific Laboratories GmbH, Planegg, D-82152 Germany) are manufactured in this work. No final results can be presented for the ongoing implantation and evaluation trials. However, preliminary histological examination of the surrounding tissue by Kohler confirm the material's biocompatibility [143].

3.2.3 Polyimide 2611 – PI

Polyimide 2611 from DuPont/HD MicroSystems is chosen because of its tested biocompatibility (international standard "Biological Evaluation of Medical Devices", ISO 10993, and USP-23 [101, 102, 103, 104, 105]) and for its lowest moisture uptake within the group of Pyralin (HD Microsystems) polyimides [84, 144, 145]. The material is supplied in the form of a liquid precursor of polyamic acids and N-Methyl-2-pyrrolidone (NMP) as the solvent. The spin-coat process of the liquid onto the wafer substrate yields a thickness of several micrometer, depending on the final rpm ³. As with BCB samples, the PI specimen deposited for the cell-culture experiments are only some $d_{PI-1,2} \approx 50 \text{ nm}$ thin, see section 3.2.4. In the curing process at $T_{(PI),c} \approx 350^\circ\text{C}$, the polymer based on biphenyldianhydride / 1,4 phenylenediamine (BPDA/PPD) forms by way of a condensation reaction.

Figure 3.5 shows the structural formula of the BPDA/PPD backbone of the PI2611 polyimide (HDMicrosystems) [146, 84]. The arrows indicate the main chemical bonds: (i) aromatic C-C, (ii) carbonyl groups C=O and (iii) imide groups (O)=C-N. The sp^2 hybrid orbitals of the benzene carbon atoms overlap to form σ -bonds between neighboring C atoms and the hydrogen atom [147]. The overlap of the remaining carbon p-orbitals give a π orbital system encompassing the benzene ring 'above' and 'below' the plane of the six C atoms. This system of delocalized π electrons contributes to the relatively high stability of the benzene ring. The carbonyl groups form a plane between the oxygen and the carbon and the two more atoms – N and C – bound to the carbon. They exhibit a high dipolarity as a result of the relatively high electronegativity differences between oxygen and carbon. Thus, electrophilic groups attack the oxygen- and nucleophilic groups the

³All PI test samples for this work are deposited at the *NMI* with the help of S. Bauerdick.

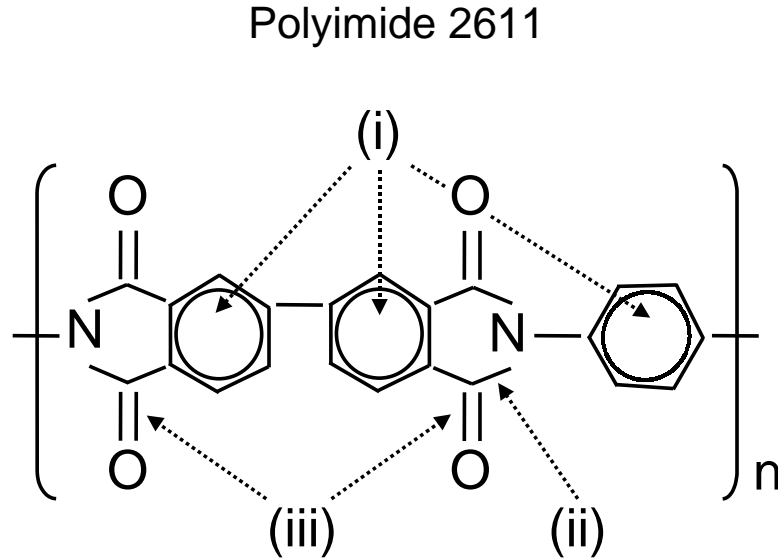


Figure 3.5: Chemical backbone structure BPDA/PPD of polyimide 2611 (HD Microsystems). The arrows indicate the main chemical bonds between carbon, nitrogen and oxygen: (i) C-C bonds in the benzene rings. (ii) C-N bonds. (iii) C=O carbonyl groups.

carbon-side group. The nitrogen forms four sp^3 hybrid orbitals which result in non-planar bonds with the three neighboring C atoms plus one N(2p) lone pair orbital. The cured PI films may be patterned in a dry etch process using an Al mask (see also section 3.3 for dry-etch BCB patterning) and a O_2 - CF_4 or O_2 - SF_6 gas composition [148, 84].

BPDA/PPD polyimide is a further development of the PMDA / ODA structure which is still the most widely used polyimide, commercialized as "Kapton" by DuPont. In contrast to PMDA / ODA, the BPDA/PPD structure does not have a (highly flexible) ether linkage (C-O-C). The dielectric constant of PI 2611 (BPDA/PPD backbone), $\epsilon_{r,PI} = 2.8$, is lower than that of PMDA / ODA. Both polyimides find application in the semiconductor industry as passivation and planarization layers and dielectrics (BPDA/PPD).

3.2.4 Ultra-thin PI- and BCB layers

As already mentioned, the transmission infrared spectroscopy spectroscopy is more sensitive to changes at the surface if the bulk material is kept rela-

tively thin. Thinness of the test sample facilitates also the impedance spectroscopy technique, described in chapter 5.2: In polyimide (probably also in BCB, though the reproducibility of the spectra is much lower) the infiltration of electrolyte components after hot-oven sterilization leads to changes in the electronic behavior of a thin surface region of the sample, see chapter 6.3.4.3. Alterations of the bulk material take place on a much longer time-scale. Therefore, in order to be able to observe diffusion-like processes in a thin polymer–electrolyte interface region in the available frequency range $f = 10^{-3} \dots 3 \times 10^5$ Hz, a thin (bulk) material layer is favored.

To this end, both commercially available organic solutions for BCB and PI are further diluted with the respective pure organic solvent. The solvent is filtered (0.1 μm) and the new solution is given about 24 hours time before it is applied to the wafer substrates. Two dilution-series serve to determine the necessary precursor concentrations to yield an approximate layer thickness of $d_{org} \approx 30 \dots 60$ nm as determined by surface profiling (SLOAN Dektak) and SEM cross section measurements. The chemistry of neither polymers are affected by this dilution process: The FTIR- as well as the XPS studies confirm the chemical structure of the test layers as compared to the literature data, see chapters 6.2.2 and 6.3 for BCB and PI, respectively.

3.2.5 Morphology of the polymers

Both polymers consist of highly cross-linked networks after the curing process. With the exception of etch tests for stimulation electrode via, see chapter 3.3, neither patterning steps, nor surface polishing, see [149, 150, 151] for BCB chemical-mechanical polishing, or deliberate surface modification [152] of any sort is attempted in this work.

The test layer's morphology is directly only observed in SEM measurements. Figure 3.6 presents a cross-section view of a thin PI sample. The meander-like "patterns" on the wafer can again be attributed to Au coagulation [121, 153, 154], compare with Figure 3.3 in section 3.2.1 (for polymer metallization see references [122, 121, 153]). Apart from those Au- artefacts, a vertical, almost columnar structure in the PI film is clearly distinguishable [155, 156]. On this SEM scale, hillocks are apparent with lateral dimensions of the order of $d_{hill} \approx 20 \dots 50$ nm.

Most literature focuses on topics such as the adhesion of metals on the polymer dielectrics [157, 158, 159, 160, 161, 162, 163, 164, 165] and on the related issue of modifying the surface through etch processes [166, 167, 165, 168, 169, 170]. Such etch steps include UV irradiation [171, 172, 173, 174], Ar sputtering [175], SF₆-, CF₄, O₂ plasma etch [176, 177], among others. Quantitative data for surface roughness vary widely for different substrate pretreat-

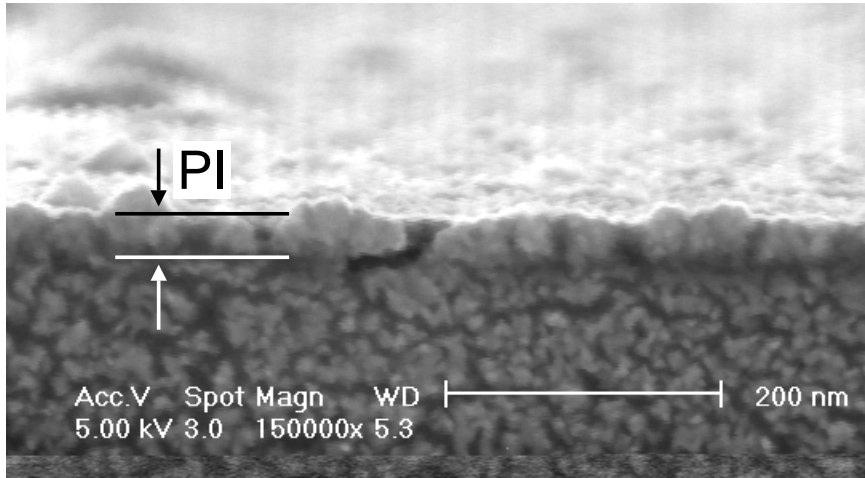


Figure 3.6: SEM cross section view of an ultra-thin polyimide test sample.

ments and (etch) treatments of the deposited layer. Amagai [163, 164] gives for *untreated* spin-coated PMDA-ODA a maximum "peak-to-valley" distance of $d_{max} = 4 \dots 60$ nm. Neiryneck [149] calculates a *rms* surface roughness for as-deposited BCB ("best region") of 0.41 nm. Borst [178] present similar AFM observations. Moreover, a certain degree of polymer crystallinity (sometimes supported by XRD measurements of polyimide [166]) is often presented as explanation for grass-like surface features after plasma-etch procedures. Patel [179, 180] reports on mechanical anisotropy of the cured PI 2611 film.

The surface roughness of the samples affects the experiments in this work: Small-scale variations in the thickness of the films increase the capacitance of the dielectric as observed in impedance spectroscopy, see chapter 6.3.4.3. Moreover, cracks and fissures on a fine *nm* scale in PI support the model of electrolyte infiltration following hot-oven sterilization, see chapter 6.3.4.3. XPS studies in chapter 6.3.2.3 make also reference to the test sample's morphology.

3.3 Sealing of stimulation electrodes

In order to apply electrical pulses to the neural tissue, the stimulation electrodes on the silicon chip must go through the encapsulation layer and reach the outer surface. The general problems regarding the adhesion of the metal electrodes to the dielectric material are well known from the design of inter-

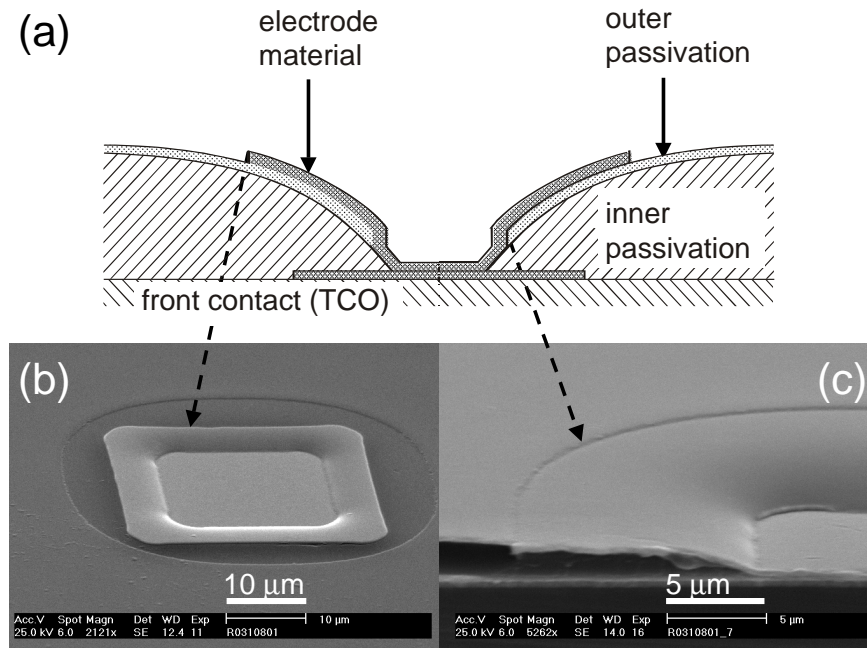


Figure 3.7: Design study of electrode-via through encapsulation layer(s). (a) Schematic cross-section. The electrode is embedded into an inner and outer passivation layer. (b) SEM top view of a model electrode. (c) SEM cross section view of a similar electrode design. See text for deposition procedures.

connects in chip fabrication. However, in the context of the retinal implant, a long term sealing of the electrode–encapsulation interface against ion diffusion from the electrolyte environment must be accomplished. Today’s TEOS SiO_2 (made from *tetra-ethyl-ortho-silicate*) features \approx vertical etch flanks and the thickness of the sputtered TiN electrodes reduces considerably at the SiO_2 edge (see the non-flat inner surface of the stimulation electrodes in the SEM views of Figure 3.1 (a) and (d)).

Figure 3.7 presents a design study for electrode feed-throughs (via) which is performed in this work. (a) On the photodiode’s transparent conductive oxide (TCO) a first layer of the gold electrode material is deposited and patterned in a lift-off technique. The usual lithography of the photoresist which forms the inner passivation is followed by a temperature ramp (preferably under low-oxygen conditions) which results in ”smooth” resist-flanks. A SiN_x layer serves as the outer passivation which would provide enhanced scratch-resistance of the encapsulation during the forceps- handling of the device in the implant-surgery. The SiN_x is patterned in HF [181]. Lastly, the positive edge of the inner passivation provides the basis for the homogeneous

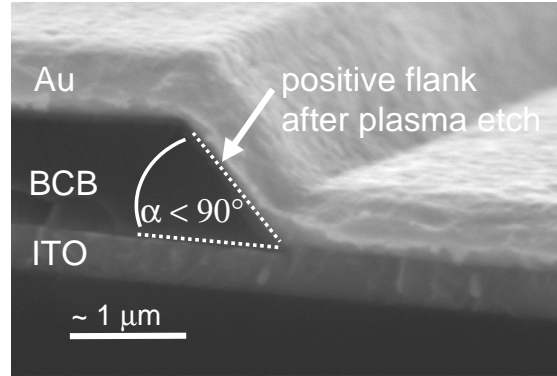


Figure 3.8: Au-electrode – BCB encapsulation interface. A dry-etch process for the BCB material results in positive via flanks ($\alpha < 90^\circ$). The sputtered Au homogeneously covers the encapsulation material.

second deposition of the Au layer which is patterned to obtain the final geometry of the stimulation electrode. Figure 3.7 (b) shows a top view (with a certain inclination) of a model electrode embedded in hardened photoresist encapsulation. In (c) the cross section of the electrode is depicted. The arrows indicate the outer edge of the Au electrode – in (b) – and of the SiN_x outer passivation – in (c). In (c) the outer Au edge lies beyond the displayed SEM window. Samples in (b) and (c) have a different geometry.

For a real implant, photoresist can, of course, not be used as the inner passivation. Figure 3.8 shows a similar design using BCB as the encapsulation layer. The BCB layer is patterned in an optimized O_2 & CF_4 dry etch process [182, 183, 184, 185] using an aluminum mask⁴. The Al mask may be patterned in a lift-off or wet-etch process. References [188, 189, 190] describe RIE processes with PECVD SiN_x and SiO_2 etch masks, reference [191] presents a photoresist soft mask process. The first Au electrode layer seen in Figure 3.7 is omitted and the "outer" Au layer directly contacts the ITO. The arrow highlights the positive etch flank in the BCB, $\alpha < 90^\circ$, which provides the basis for the homogeneous coverage by the Au.

The handling of the implant device during surgery may lead to scratches in the polymers' surface which might impair the long-term stability of the

⁴Technological remark: The CF_4 component in the etch gas attacks Si-O bonds in BCB, see Figure 3.4 [186, 187]. Consequently, no SiO_2 passivated substrate may be used for BCB etch trials.

encapsulation. Similar to the design study in Figure 3.7, future technological work on the polymer encapsulation may include an outer inorganic SiN_x - or SiO_xC_y - based layer with much enhanced scratch resistance. The idea of a inorganic / organic double layer encapsulation appears in the semiconductor industry for the passivation of thin film hybrid circuits [192], the protection of space craft [193, 194] among others. Reference [195] aims at improving the adhesion of PECVD SiO_2 and SiN_2 on BCB by analysing mechanical stresses in multilayer systems [196, 197, 193, 198].

Chapter 4

Cell-cultures for in-vitro tests

This chapter describes the in-vitro cell culture experiments which are employed to simulate the effect of living tissue on the test sample encapsulation layers. The cell cultures are characterized and the last section presents the experimental procedures for the in-vitro experiments.

4.1 Cell-cultures

As outlined in chapter 1.2, the long-term integrity of the implant encapsulation must be tested before the application of the device to human beings. Current observations include on the one hand the degradation of the TEOS - SiO₂ encapsulation after implantation in different animal models for up to 18 month, see chapter 3.1. Also, multi-electrode-arrays (MEA) with a SiO_x:C/SiN_y passivation show a decrease of the SiO_x:C/SiN_y- thickness where rat's brain tissue was in close contact with the device for approximately 3 month [199]. On the other hand, in-vitro experiments with PbS at elevated temperatures show no such "corrosion" of SiN_x encapsulation layers [199]. Moreover, the exact (bio-) chemical processes which lead to the failure of SiO₂- or SiO_x:C/SiN_y- layers are largely unknown [45].

While test-sample implantations in animal retinae come as close as possible to a device implantation in the human retina, they are also the most expensive and morally critical available tests. Moreover, XPS and FTIR experiments require a minimum size of the test samples of $A_s \geq 8 \times 8 \text{ mm}^2$, which precludes retinal- or subcutaneous implantations. In this work in-vitro cell culture experiments are devised to partly simulate the in-vivo conditions of animal tests. The cells attach to the test layers, reproduce, form networks and release enzymes and metabolites into the culture medium (see reference [200] for a description of various substances which are produced by cells and

”exported” into the extracellular domain.). The choice of the cell cultures is determined by (i) the necessary development of a relatively homogeneous cell coverage over the entire sample area. All three main experimental techniques, particularly the XPS and the FTIR spectroscopy, require a minimum geometric size of the test samples of the order of $A_s \geq 8 \times 8 \text{ mm}^2$. (ii) The cell cultures must be well established in the biology community in terms of handling, proliferation rates, etc. (iii) The retina environment cannot be ”reproduced” by in-vitro cell cultures. Therefore, different cell types should be used in parallel experiments to check for culture-specific changes in the encapsulation layers [201]. At the time of the experiments no nerve cell culture was available for in-vitro tests. The following section presents the two cell cultures chosen for this work that are available at the Department of Biology, University of Stuttgart, research group of Prof. D. Hülser ”Biophysics” .:

BICR /M1R_k, ”Marshall cells”

In 1969, the BICR /M1R_k cells – throughout this work called ”Marshall cells” – were established as an in-vitro cellline derived from a transplantable tumor BICR/M1 which had been cultivated from the spontaneous mammary tumor of a femal Marshall rat [202]. The Marshall cellline grows under standard culture conditions in Dulbecco’s medium at $T_{inc} = 37^\circ\text{C}$ under $c_{CO_2} = 8 \%$ atmosphere. Rajewsky & Grueneisen [203] give a doubling time $t_{(BICR),d} \approx 14 \text{ h}$ up to a saturation density of $\rho_{(BICR),s} \approx 14 \times 10^4 \text{ cells cm}^{-2}$. The Marshall cells are of a fibroblastoid type.

HeLa cells

The HeLa cellline originates from a human cervix carcinoma. The in-vitro cellline was first cultivated in 1953 [204]. HeLa cells exhibit an epithelial morphology, see references [205, 206]. More specifics may be obtained from the ”American Type Culture Collection” (ATCC), a non-profit bioresource center. (<http://www.atcc.org>).

Figure 4.1 demonstrates the reproduction and cross-linking of Marshall cells on an exemplary polyimide sample in (a) and HeLa cells on a polyimide sample in (b). Both pictures are recorded approximately $t_{pic} \approx 20 \text{ min}$ after the petri dishes were removed from the incubator and exposed to an ambient atmosphere at a temperature of $T_{pic} \approx 15 \dots 20 \text{ }^\circ\text{C}$. In order to discern individual cells, both photos focus on border regions of clustered cells. Cell dendrites reaching out to neighboring cells indicate the two-dimensional growth of both cell cultures, eventually leading to an almost homogeneous coverage of areas of up to 1 mm^2 of the samples’ surface. Separated by

regions with a lower cell density, such islands of cell clusters cover the entire surface of the samples, $A_s = 250 \text{ mm}^2$.

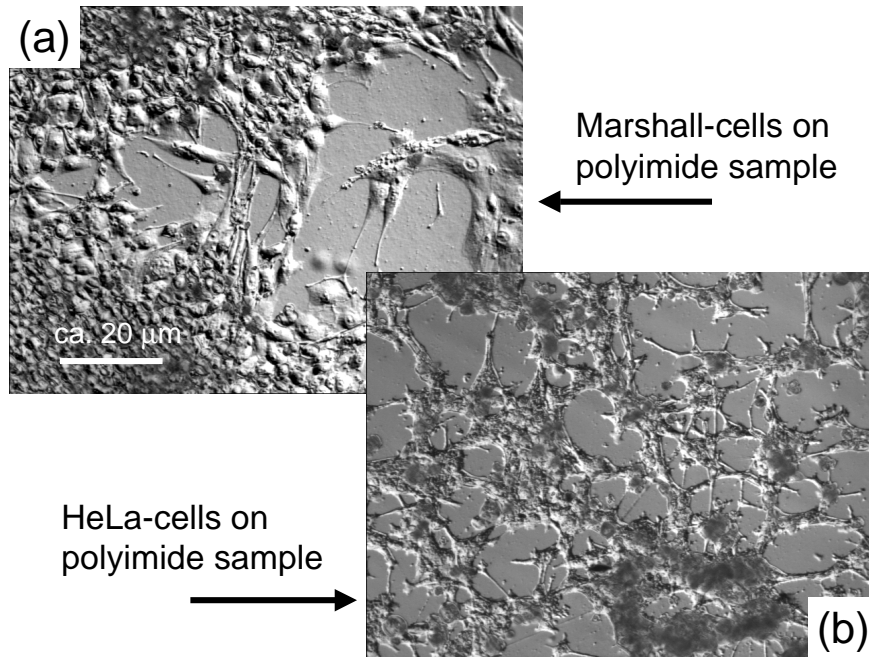


Figure 4.1: Optical microscope view of living cells on polyimide samples. (a) Marshall cell culture after 13 days. (b) HeLa cell culture after 18 days.

4.1.1 Cell culture procedures

All cell culture experiments are conducted at the Dept. of Biology of the University of Stuttgart, Institute of Biophysics, Prof. D. Hülser. The experiments are planned with the help of Dr. Brümmer and carried out in co-operation with B. Rehkopf and colleagues.

The schematic diagram in Figure 4.2 shows the sequence of process steps for the cell culture experiments. At each stage, a group of samples is analysed as described in chapter 5. The untreated samples are referred to "As deposited" in the following work. All samples that are to be treated with living cells or exposed to the control medium are sterilized in a hot-oven at $T_{h.o.} = 105^\circ\text{C}$ for $t_{st} \approx 10$ hours in ambient atmosphere. The cell culture is started by immersing the samples into the growing medium in a petri dish followed by sowing ≈ 15.000 Marshall - or HeLa - cells onto the samples' surface. The control series contains no living cells in the growing medium. All

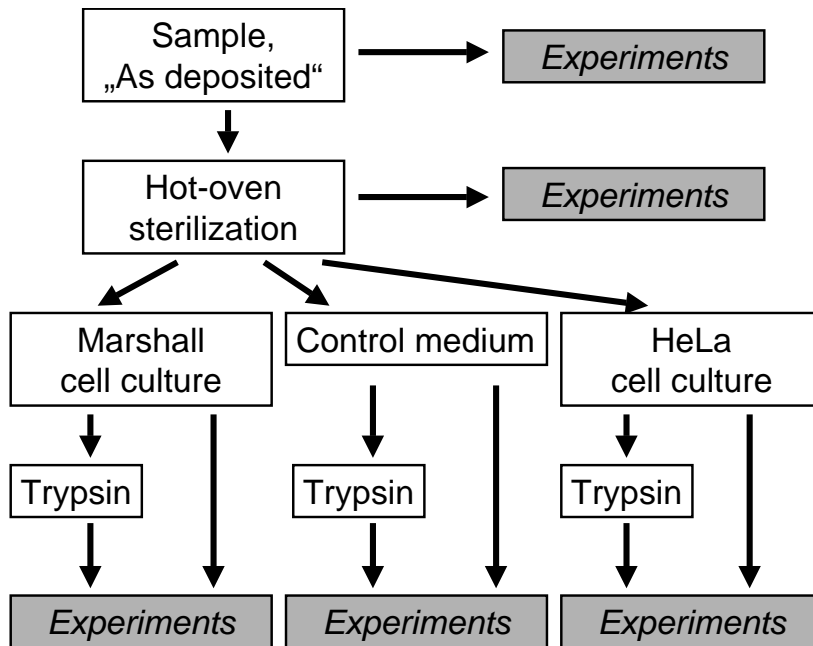


Figure 4.2: Schematic diagram of the cell culture experiments.

three sample groups are stored in an incubator at $T_{inc} = 37^{\circ}\text{C}$ and a carbon dioxide concentration of $c_{CO_2} = 8\%$. Depending on the planned duration of the celltests, the growing medium is replaced approximately every two to five days¹ The color of the growing medium serves as an indicator of its pH value. Due to the release of metabolic waste products of the cells, the pH value decreases over time reaching $\text{pH} = 6.7$ (the medium turns from red through orange to yellow) as the lowest reasonable concentration for a "healthy" cell culture. Changes in the morphology of the cells such as a rounding up of the cells or a detachment from the samples's surface indicate the deterioration of the cell culture. If detected early, a medium change can help restore the healthy status of the cells.

After the removal of the samples from the cell culture, the cells that remain attached to the surface of one group of samples are removed with PbS at $T_{PbS} \approx 35^{\circ}\text{C}$. A second group of samples is treated with *trypsin* at the end of the cell culture experiments. As a member of the protein

¹The number of cells on the samples growth exponentially with time until the saturation limit, see reference [207]. With increasing duration of the celltest, the cells exhaust the growing medium faster and produce more waste which is released into the medium. Therefore, the growth medium should be replaced more often towards the end of the celltest than at the start of the experiment.

splitting serin proteases, trypsin is a commonly used enzyme to inhibit the cell-cell adhesion². In the context of this work, trypsin reduces the cell-sample adhesion, thus lowering the amount of residual cells or cell-components on the samples surface. Following the removal from the cell medium, the samples are rinsed in PbS. In a second step, the samples are immersed in trypsin (at $T_{tryp} = 37^{\circ}\text{C}$) for 5 min. A last PbS rinsing completes the cleaning procedure. The control-medium samples are also rinsed in PbS.

Until shortly before the XPS and FTIR measurements, one group of samples is stored in PbS (at room temperature and low light intensity), followed by a last rinse in deionized water and drying with clean nitrogen. All other samples are immediately rinsed in deionized water, dried with clean nitrogen and stored under ambient atmosphere and low-light conditions.

Appendix 7.1 lists the enzymes and vitamins and the inorganic components of the Dulbecco's growing medium (throughout the text called control medium, co.-me.).

²Thus disaggregated cells may be used as seed cells to initiate a new in-vitro cell culture.

Chapter 5

Measurement techniques

This chapter presents the main techniques employed in this work to characterize the inorganic and organic encapsulation materials. The first section (5.2) focuses on impedance spectroscopy. Following a description of the experimental setups, the mathematical analysis of the impedance data based on an equivalent circuit is outlined. The next two sections (5.3), (5.4) introduce to the Fast Fourier Infrared (FTIR) spectroscopy and the X-ray photoelectron spectroscopy (XPS), respectively. The IR spectrum of the growing medium is presented and a series of XPS cycles on one polyimide sample demonstrates the radiation resistance of the polymer.

5.1 Choice of techniques

As described in chapter 3.1, current observations on explanted SiO₂ layers and by Fromherz [45] suggest a biochemical degradation mechanism of the inorganic encapsulation layers. Consequently, XPS as a highly surface-sensitive analytical tool is chosen to detect changes in the chemical binding configurations after the in-vitro cell culture tests presented in the previous chapter 4.1. Recorded spectra are compared with an extensive XPS literature data base for all three encapsulation materials used in this work and variations are assigned to an increase or a decline of specific chemical bonds¹.

The characteristic high surface sensitivity of XPS makes this method vulnerable to a distortion of results through surface contamination of the samples. Hence, in addition to a careful experimental analysis, the transmission

¹Most XPS analysis in the literature focuses on the dielectrics' adhesion properties in multilayer systems and on (plasma-) surface modifications such as chemical-mechanical polishing and roughing in semiconductor industry. Although the cell culture treatment performed in this work is of an entirely different nature, the literature XPS spectra provide a rich source for the interpretation of the spectra that are recorded in this work.

FTIR serves as the volume- and surface sensitive, complementary measurement technique to control the absolute number of the main material-specific chemical bonds.

Apart from chemical degradation, the structural integrity of the test layers as well as the water uptake of the material affect the long-term biostability of the implant device. Impedance spectroscopy as the third main experimental technique observes the electronic behavior of the dielectric materials. Thus a higher limit for the density of pin-holes in the test layers can be determined and dipol moments – such as water molecules – observed as they penetrate the polymer surface region.

Each of the three measurements techniques has its merits and disadvantages. Combined, the three techniques yield strong arguments for the evaluation of the long-term biostability of the encapsulation layers.

5.2 Impedance spectroscopy

5.2.1 Experimental setup

The measurement configurations to record impedance spectra should be chosen so as to minimize the impact of the setup on the material in terms of changes to the materials morphology or its chemical composition. Moreover, the setup must yield reproducible spectra for similar sample specimen.

Figure 5.1 presents the *electrolyte cell* setup which is used to record most of the impedance spectra of the dielectrics. The setup is adapted from reference [208] where it serves for the impedance spectroscopy of components of dye-sensitized solar cells. The silicon wafer substrate of the dielectrics serves as the back contact in the electric circuit. The front surface of the samples is contacted using Phosphate buffered Saline electrolyte (PbS), see Appendix 7.1, which minimizes the mechanical interference with the probe. Furthermore, this contact method facilitates the study of changes of the electrochemical behavior of the dielectrics over the time of exposure to the physiological PbS (in analogy to exposure to physiological solution in the human eye). A semi-transparent Cr-layer on a upper glass substrate serves as the reference electrode of the electrochemical cell. In an attempt to explore possible oxydation- or series-resistance effects of the semi-transparent Cr layer, two polyimide samples are mounted in the electrolyte cell using several hundred *nm* thick evaporated gold as the "top"-electrode. No significant spectral changes are observed. A foil based on *Ethylen/Vinyl/Acetat* copolymers (EVA foil) provides for the spacing between the dielectric/wafer – and the Cr-glass plate and seals the cavity. During the assembly, PbS is

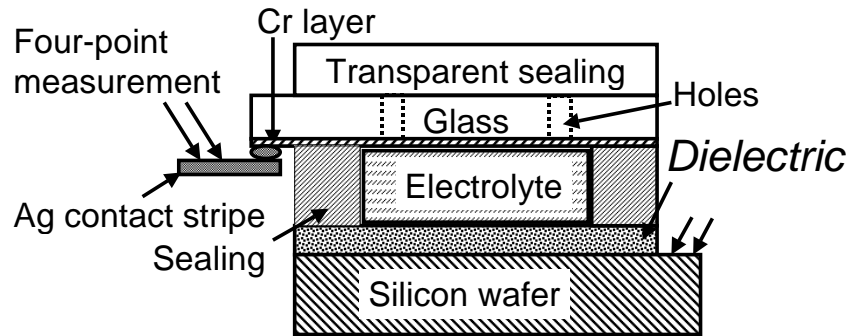


Figure 5.1: The "electrolyte cell" setup for impedance spectroscopy on dielectric layers. The front side of the dielectrics is contacted with an electrolyte solution. The highly-doped silicon wafer substrate and the thin Cr layer on the glass sheet serve as electrodes which are contacted in either a two-point or four-point measurement setup.

filled into the cavity through two holes in the glass substrate which are subsequently sealed up. 1 cm^3 PbS contains approx. 0.9×10^{20} Na^+ and Cl^- ions each. Thus, the potential drop across the highly conducting PbS is negligible and no third auxiliary electrode is necessary.

5.2.1.1 Alternative contacting methods – (A) contact evaporation

In an alternative contacting method to the electrochemical cell, a thin Au layer ($d \approx 200 \dots 300 \text{ nm}$), preceded by several monolayers of Cr is evaporated through a shadow mask onto polyimide samples [209]. The wafer substrate is contacted using an Ag contact stripe similar to the electrochemical cell. During the measurement, the one or two microprobe needle/s (in the two or four point measurement setup, respectively) directly contact the gold "top" layer on the polyimide. Depending on the varying contact pressure in the setup, the tungsten or gold needles locally deform (i.e. impress) the underlying polyimide to an unknown degree. As a result, the volume shunt resistance decreases (unreproducibly). The variation of the volume shunt resistance is most dramatic for thin polyimide layers, see chapter 6.3.4.1.

The contact evaporation is only tested with polyimide samples. It is expected that similar measurement results would be obtained with BCB

samples. The thicker $\text{SiO}_x\text{:C/SiN}_y$ layers might prove more resistant to mechanical stress during the needle contacting which would improve the reproducibility of the layer's shunt resistance. However, as with the two polymer dielectrics, the electrolyte cell appears the least invasive contacting method for the $\text{SiO}_x\text{:C/SiN}_x$ samples.

5.2.1.2 (B) Gold leaf contacting

The evaporation of the contact material requires the sample to be temporarily exposed to vacuum. Thus, the evaporation method precludes all polyimide tests involving the possible uptake of electrolyte components after the hot-oven sterilization or the exposure of the polyimide material to the growing medium of living cells.

The third contacting method explores the formation of a planar capacitor (with the polyimide as the dielectric) using gold leaves. Commercial gold leaves are cut into 1 cm^2 pieces and attached to the polyimide surface using a commercial squirrel-hair brush. Under low air-ventilation conditions, an Au wire ($\approx 20\ \mu\text{m}$ in diameter) is bonded to the gold leaf with a tiny droplet of silver conductive paint. In contrast to the standard application of gold leaves to solids, no adhesive promoter (commercial liquids of undisclosed composition) is applied. The resulting Au layer shows a "homogeneous pattern" of small-scale "wrinkles". The fraction of the gold surface which touches the polyimide surface (i.e. comes close to the theoretical separation of some 50 nm from the wafer contact) is unknown. A polyimide capacitance which is difficult to reproduce and by a factor of 30 ... 100 lower than theory requests is the result. Although the margin of error should decrease with increasing polyimide thickness, this contacting method is only tested on the thin PI-1 series. Further experimental learning might improve the applicability of the gold leaf contacting method; in this work the initial results are presented in section 6.3.4.1 but the method is abandoned in favor of the electrolyte cell experiments.

5.2.2 Equivalent circuit

Figure 5.2 depicts the likely equivalent circuit of the two-electrode electrochemical cell shown in Figure 5.1. The silicon wafer substrate and the chromium layer on the glass plate form the outer $R_g C_g$ elements shown in (a). For the electrolyte cell setup that is used throughout this work, the total surface area A_s divides into an area $A_{PbS} \approx 100\text{ mm}^2$ that is covered with the electrolyte ($\epsilon_{H_2O} = 80$ [210]) and an area $A_{EVA} \approx 150\text{ mm}^2$ used by the *E*thylen/*V*inyl/*A*acetat- based (EVA) sealing of the electrolyte cell

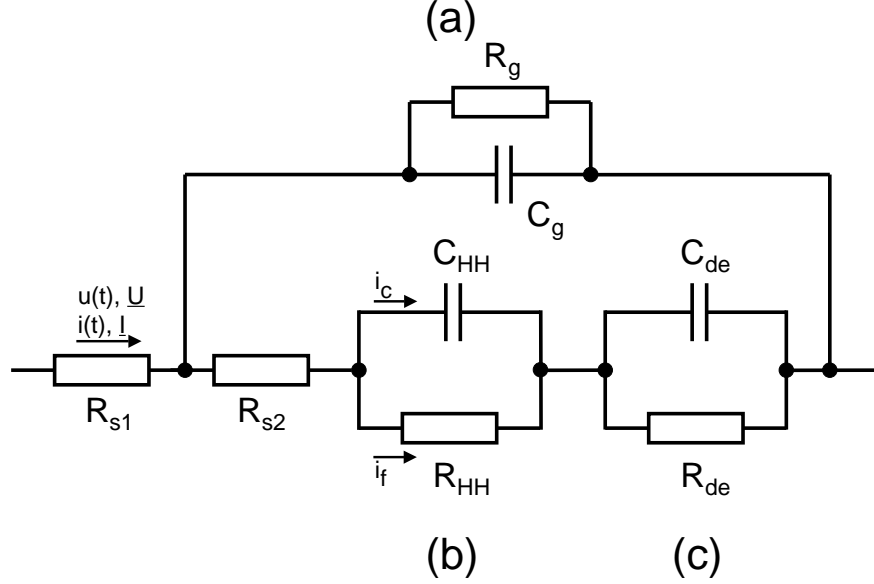


Figure 5.2: Simplified equivalent circuit of the two-electrode electrochemical cell. The silicon wafer and the Cr-glass form the outer geometric $R_g C_g$ element of part (A). Two series-connected RC-elements are identified, namely, (B), that of the Helmholtz double layer (HH) and (C) that of the dielectric material (DE). i_c indicates the component of the total current which originates in the charging of the capacitive element C_{HH} . The faradaic current through the shunt resistance R_{HH} is marked with i_f . The arrows at the R_s series resistance exemplarily indicate the uniform direction of the voltage and current across all circuit elements.

($\epsilon_{EVA} \approx 3-4$). While A_s is almost constant, A_{PbS} has a margin of error of $MOE_{(A),PbS} = \pm 20\%$. The separation of both "electrodes" is of the order of $d_{Cr-W} \approx 200 \times 10^{-6}$ m but varies between individual cell-assemblies. The general equation for a plane capacitor holds,

$$C = \epsilon_0 \epsilon_r \frac{A_{PbS,EVA}}{d}, \quad (5.1)$$

where ϵ_0 , ϵ_r are the universal dielectric constant and the dielectric constant of the material, respectively, A is the surface area of the capacitor and d is the separation between the capacitor's planes [210]. Equation (5.1) yields a geometric capacitance $C_g \approx 3 \times 10^{-10} \dots 3 \times 10^{-9}$ F.

Figure 5.2 (b) and (c) illustrate the series connection of two RC-elements, namely, that of the Helmholtz double layer (HH) at the solid-state – electrolyte interfaces, see references [211] and [212], and that of the dielectric

probe (DE), respectively. The electric current that flows through the HH layer consists of one component i_c from the charging/decharging of the almost ideal double layer capacitance C_{HH} and another component of faradaic currents i_f . For simplicity, the shunt resistance R_{HH} is regarded frequency-independent in this work. The capacitances for the inorganic and organic dielectrics are given by equation 5.1. All capacitances come close to ideal capacitive elements. The more complex behavior of the two polymers PI and BCB after sterilization requires a more detailed description of the model electric circuit which will be given in the context of the analysis of the experimentally recorded impedance spectra, see chapter 6.3.4.3.

Throughout this work, a parallel RC element plus a series resistance is termed *Randels equivalent circuit*, see reference [213, p. 376].

5.2.3 Mathematical description and fitting routine

In impedance spectroscopy, the measurement configuration is perturbed by an alternating voltage signal of small magnitude V_0 ; $V_0 = 10$ mV throughout this work. The current amplitude I_0 and phase shift ϕ relative to the applied voltage signal is recorded by the measurement instrument (HP 4192A LF impedance analyser or a Schlumberger Solatron 1250 frequency response analyser combined with an EG & G 273 A potentiostat) as described in references [213, p. 368 ff.], [214], [215].

The current–voltage correlation is conveniently described using complex notations [216]. Thus, a purely sinusoidal voltage signal \underline{U} is expressed by

$$\underline{V} = V_0 e^{j(\omega t + \phi)}, \quad \text{Im}\{\underline{V}\} = u(t) = U_0 \sin(\omega t + \phi), \quad (5.2)$$

where ω is the angular frequency, V_0 the amplitude, $v(t)$ the time-dependent voltage and j the imaginary unit, $j = \sqrt{-1}$. The correlation between a pure capacitance C (eg. $R_{sh} = \infty$, $R_s = 0 \Omega$), the time-dependent voltage $v(t)$ and time-dependent current $i(t)$,

$$i(t) = C \frac{du(t)}{dt} = CU_0 \omega \cos(\omega t + \phi) = \text{Im}\{\underline{I}\}, \quad (5.3)$$

holds also in the complex system²,

$$\underline{I} = C \frac{d\underline{U}}{dt}. \quad (5.4)$$

Thus, the complex resistance or *impedance* \underline{Z} , defined as

$$\underline{Z} = \frac{\underline{U}}{\underline{I}}, \quad (5.5)$$

²That is because $\frac{d(\text{Im}\{\underline{U}\})}{dt} = \text{Im}\left\{\frac{d\underline{U}}{dt}\right\}$.

equals

$$\underline{Z} = \frac{1}{j\omega C}. \quad (5.6)$$

For $R_s > 0 \Omega$,

$$\underline{Z} = R + \frac{1}{j\omega C} \quad (5.7)$$

holds. The *admittance* \underline{Y} of a *parallel* RC-element is defined as

$$\underline{Y} = G + j\omega C_p, \quad \underline{Y} = \frac{1}{\underline{Z}} \quad (5.8)$$

with the conductance G . From the previous equation 5.8 follows for the impedance \underline{Z}

$$\underline{Z} = \frac{G - j\omega C_p}{G^2 + \omega^2 C_p^2} \quad (5.9)$$

$$\text{Re}\underline{Z} = \frac{G}{G^2 + \omega^2 C_p^2} \quad (5.10)$$

$$\text{Im}\underline{Z} = \frac{\omega C_p}{G^2 + \omega^2 C_p^2}. \quad (5.11)$$

Thus, $\text{Im}\underline{Z}$ can be expressed in terms of $\text{Re}\underline{Z}$ and the conductance G for a parallel RC-element,

$$\text{Im}\underline{Z} = -\sqrt{\text{Re}\underline{Z}(1/G - \text{Re}\underline{Z})}. \quad (5.12)$$

Adding the inevitable series resistance R_s to the RC-circuit leads to

$$\text{Im}\underline{Z} = -\sqrt{(\text{Re}\underline{Z} - R_s)(1/G - \text{Re}\underline{Z} - R_s)}. \quad (5.13)$$

The capacitors shown in Figure 5.2 represent the special case of the more general *Constant Phase Element* (CPE), defined as

$$\underline{Z} = \frac{1}{A(i\omega)^\kappa}. \quad (5.14)$$

A represents the amplitude ($[A] = \text{F}^\kappa \text{S}^{1-\kappa} \text{cm}^{-2}$) and κ the phase angle of the circuit element. $\kappa = 1$ yields the ideal capacitor and $\kappa = -1$ results in an ideal inductance. In this work, any inductive elements in the experimental setup are neglected and κ varies between 0.5 and unity. All capacitances in the equivalent circuit of Figure 5.2 come close to ideal capacitive elements, indicated by $\kappa = 0.9 \dots 1$. A value of $\kappa = 0.5$ that occurs in the fitting procedure

of measured impedance data indicates a process which might be governed by the diffusion of electrolyte components. A more detailed equivalent circuit is then required, see chapter 6.3.4.3.

Based on a specified equivalent circuit for the experimental configuration, the fit of all circuit parameters for the entire frequency range is numerically performed using the program "Zview.exe" from Scribner Associates Inc., North Carolina, USA. However, a simple Randels equivalent circuit (i.e., a parallel RC element with a series resistance) may be fitted in a "hands-on" approach as this paragraph illustrates: The conductance G as well as the series resistance R_s of the Randels circuit are obtained by fitting $\text{Im}\underline{Z} = f(\text{Re}\underline{Z}, R_s, G)$ in equation 5.13 to the experimental data. In a similar manner, a fit of $\text{Re}\underline{Z} = f(G, \omega, C_p)$ or $\text{Im}\underline{Z} = f(G, \omega, C_p)$, equation 5.11, with the experiment, $\text{Re}\underline{Z} = \text{Re}\underline{Z}(\omega)$, or $\text{Im}\underline{Z} = \text{Im}\underline{Z}(\omega)$ yields the capacitance C_p as the only free parameter that is left in the model.

Figure 5.3 and Figure 5.4 show examples for both fit procedures. The

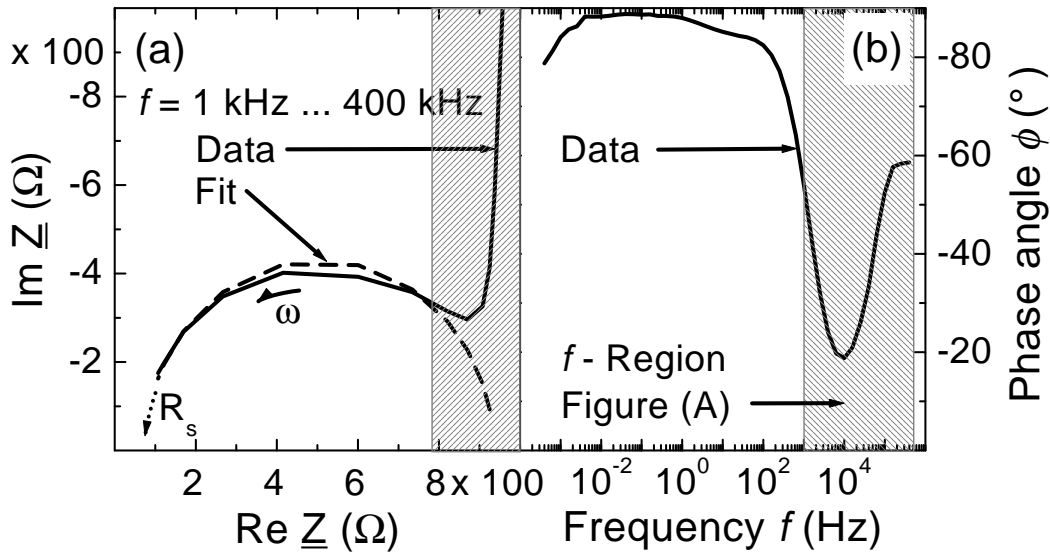


Figure 5.3: (a) Nyquist plot for the high-frequency range of the impedance spectrum of a polyimide sample. The fit curve illustrates the fitting routine for R_s and G of a Randels equivalent circuit. The shaded area indicates the onset of a second semi-circle towards lower frequencies. (b) Phase angle ϕ between the current I and the voltage V signal over the entire frequency spectrum. The shaded area indicates the frequency range of Figure (a).

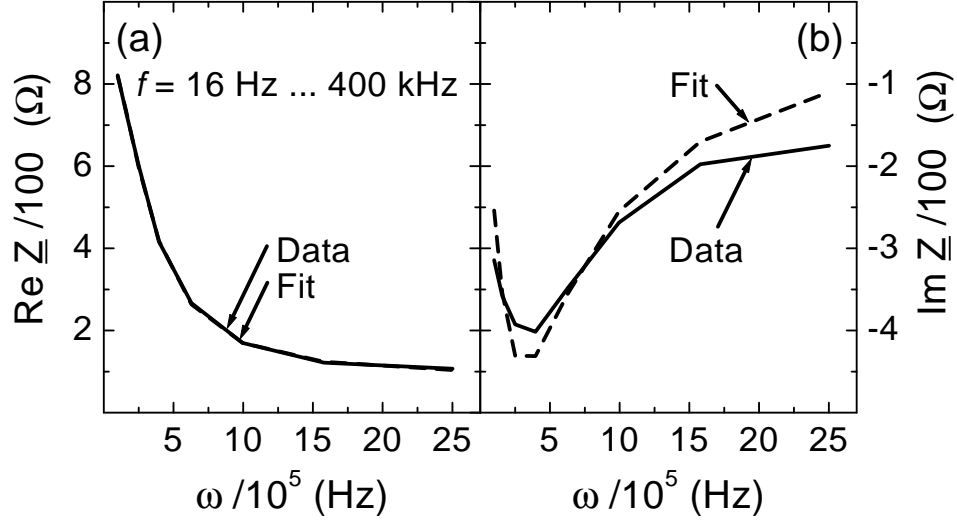


Figure 5.4: Example for the fitting routine for the capacitance C_{DE} . (a) and (b) show $\text{Re}\underline{Z}$ and $\text{Im}\underline{Z}$ plotted versus the angular frequency ω . The experimental data and the numerically fitted curves based on one parallel RC-element are given.

spectrum is recorded from a polyimide sample in the electrolyte cell setup. For simplicity, the geometric $R_g C_g$ -element of the setup may be neglected. The resulting equivalent circuit consists of two series connected RC elements: $R_{de} C_{de}$ and $R_{HH} C_{HH}$. In Figure 5.3 (a), $\text{Im}\underline{Z}$ is plotted versus $\text{Re}\underline{Z}$ for the high frequency range where the $R_{de} C_{de}$ -parallel circuit of the dielectric plus the series resistance R_s in the setup dominates the electric behavior. Following equations 5.11 and 5.11 for a parallel RC-circuit, the Nyquist plot should form a semi circle with $\text{Re}\underline{Z} = \text{Im}\underline{Z} = 0$ as the angular frequency ω approaches infinity. For $\omega \rightarrow \infty$, a series resistance R_s shows up as the minimum of $\text{Re}\underline{Z}$, see equation 5.7.

The steep part of the measured data towards a high $\text{Im}\underline{Z}$ component signals the onset of a second arc (i.e. a second semi-circle) which corresponds to the second RC-element $C_{HH} R_{HH}$ of the equivalent circuit in Figure 5.2 (b). Figure 5.3 (b) shows the phase angle ϕ ,

$$\phi = 180/\pi \arctan \frac{\text{Im}\underline{Z}}{\text{Re}\underline{Z}}, \quad (5.15)$$

for the entire frequency range $f = 10^{-4} \dots 10^6$ Hz. The shaded area denotes the frequency range used in this example of the fitting of the dielectric's $R_{de} C_{de}$ -element.

Figure 5.4 (a) and (b) show $\text{Re}\underline{Z} = \text{Re}\underline{Z}(\omega)$ and $\text{Im}\underline{Z} = \text{Im}\underline{Z}(\omega)$, respectively, for the experimental data and the fitted curves as an example for the fitting routine of the capacitance C_{DE} .

5.2.4 Electrolyte cell without a dielectric

In an attempt to characterize the electrolyte cell measurement setup, Figure 5.5 presents the impedance spectrum recorded with an uncoated Si-wafer substrate, i.e. without a dielectric layer. The spectrum does not change over time after the assembly of the electrolyte cell. The fit-curve shows the

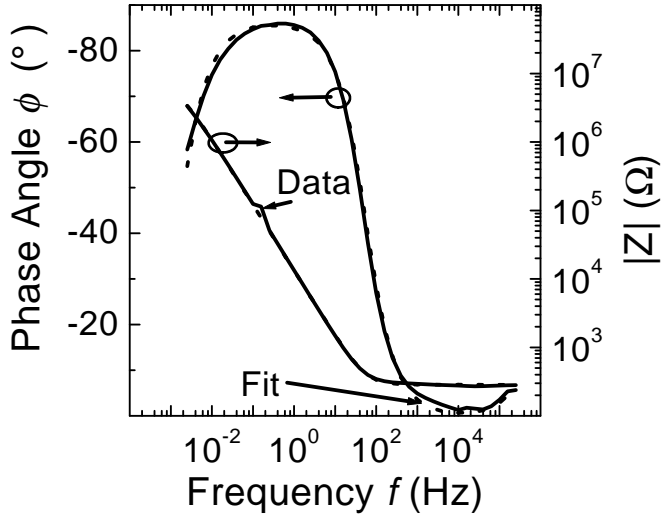


Figure 5.5: Bode plot of impedance $|\underline{Z}|$ and phase angle ϕ versus frequency for an electrolyte cell without dielectric. The measured data (solid) and the fit curve (dash) are hardly distinguishable.

result of a numerical fit of the equivalent circuit in Figure 5.2 without the dielectric's $R_{de}C_{de}$ element. The data may also be fitted with a simple Randles equivalent circuit. For the geometric capacitance C_g an upper limit of $C_g \leq 5 \times 10^{-9}$ F is obtained. Similarly, a lowest limit for the shunt resistance R_g is found, $R_g \geq 1 \times 10^6 \Omega$. Since $|\underline{Z}| \rightarrow R_{s1} + R_{s2}$ for $f \rightarrow \infty$, the total series resistance $R_{s,\Sigma} = R_{s1} + R_{s2}$ is of the order of $R_{s,\Sigma} = 250 \Omega$. However, $R_{s,\Sigma}$ varies with the thickness of the thin transparent Cr-layer on the glass sheet between different Cr-evaporation runs. The $R_{HH}C_{HH}$ element of the two Helmholtz layers is characterized by $R_{HH} \geq 5 \times 10^6 \Omega$ and $C_{HH} \approx 1 \dots 2 \times 10^{-5}$ F. It is assumed here that the electrolyte covered surface areas of the wafer and the Cr-layer are identical. However, in a setup which contains a dielectric layer, that material may exhibit a higher

surface roughness than the Cr-layer and the corresponding Helmholtz capacity $C_{HH,de}$ will be greater as well. For simplicity, both Helmholtz layers are always represented by one $R_{HH}C_{HH}$ element in this work.

5.3 Fast Fourier infrared spectroscopy

According to the quantum mechanical selection rules, see references [217, chapter 10], [218], molecules which have a non-vanishing permanent electric dipole moment interact with electromagnetic radiation. Thus, molecules which are composed of different atoms (as opposed to "homonucleus" ones, such as H_2 , O_2 , etc.) may exhibit absorption bands which correspond to specific bond stretching and / or bond bending (always accompanied by rotational bands of the molecule). As a result of the strong attractive force between the atoms (see "classical" Hooke's law for the one-dimensional harmonic oscillator: $m \frac{d^2x}{dt^2} = -k_F x$, m = mass of atoms in molecule, $k_F = 10^2 \dots 10^3 \text{ Nm}^{-1}$, x = displacement from equilibrium), all such oscillations are in the infrared frequency range.

Fast Fourier InfraRed spectroscopy (FTIR) is based on an interferometer technique which was first devised by Michelson³ [219]. Infrared light that is transmitted through the sample enters the interferometer which produces an interferogram, i.e. a plot of light intensity v the optical path difference. The *fast* Fourier transform mathematical algorithm first published by Cooley and Tukey [220] serves to calculate the frequency spectrum of sin waves which make up the interferogram.

In this work, a Bruker IFS 66 FTIR instrument⁴ and "OPUS" software is used to analyse the IR-transmission spectra of the samples. The measurements are performed under low-vacuum conditions and each spectrum represents the average of 1000 scans (aperture 0.5 mm). A spectral resolution of 4 cm^{-1} is chosen. A liquid nitrogen cooled HgCdTe element serves as the infrared detector (MCT detector ID-313/8, operating temperature $T_{FTIR} = 77\text{K}$ [221]). With bandgap of $E_g \approx 0.12 \text{ eV}$, the HgCdTe detector sets the lower limit for the frequency range. At lower frequencies, the signal to noise ratio of the detector deteriorates dramatically.

The infrared spectrum of the Dulbecco's growing medium is recorded with a Perkin Elmer spectrophotometer (Model 283) [222]. This device is a double beam optical null instrument (for a description of such techniques see

³Albert A. Michelson, 1852–1931

⁴All FTIR spectra are recorded with the help of S. Maisch, S. Seifritz and M. Schütz at the Dept. of Organic Chemistry, research group of Prof. Effenberger, at the University of Stuttgart.

reference [219]). A heated ceramic tube serves as the radiation source and the transmitted radiation is split into wavelength components with a gating monochromator. The detector is based on a bolometer technique using a blackened gold leaf as the IR absorber material.

In the context of this work, FTIR is primarily used to observe chemical groups in the encapsulation materials that *change* as a result of the cell culture experiments. Consequently, the presented plots include frequency ranges, where a reproducible decrease or increase of absorption is observed. Following this rule, material specific, well known absorption bands are identified, while other distinct bands (which may be characteristic for the examined dielectric) remain unaccounted for.

All dielectric samples that are to be analysed by way of FTIR spectroscopy are deposited on both side polished, high resistivity silicon wafers. A separate wafer from the same wafer production charge serves as the reference material⁵ (RW = reference wafer). Variations between the wafers of the identical production charge, particularly with regard to the wafer thickness, may affect the IR-transmission. Comparisons between absorption bands of Si containing bonds must be treated with caution. Thus, while a reproducible decline of Si-N bonds is observed for SiO_x:C/SiN_x samples after the celltests, see chapter 6.1.2, a similar observation for O-Si-O bonds in the BCB layer is less clear and needs further verification, see chapter 6.2.1.

All dielectric spectra S_{de} are normalized with the spectra of the corresponding reference wafer, S_{rw} ,

$$S_n = \frac{S_{de}}{S_{rw}}, \quad (5.16)$$

to give the normalized spectra S_n which are presented throughout this work.

Some spectra exhibit strong interference patterns which originate in the two parallel Si-vacuum interfaces of the wafer substrate and a slightly tilted (i.e. not 90°) incidence of the IR radiation upon the sample. Therefore, those spectra are smoothed as indicated in the text. For all plots, a baseline correction using the rubberband method is applied in the designated spectral range.

5.3.1 Infrared spectrum of Dulbecco's medium

During the exposure of the encapsulation materials to the growing medium and living cells, an enormous variety of organic molecules can adsorb at

⁵Ideally, the reference sample would be cut from the same wafer substrate. The spin-on deposition of the two polymers, BCB and PI, precludes this option since the spinning process is best performed on round, whole piece wafers.

the sample's surface, see chapter 4.1. For polyimide samples, a study of the water rinse effectiveness with regard to XPS-detectable control medium residues is undertaken, see chapter 6.3.2.3. In order to be able to identify control medium residues in FTIR spectra after cell culture treatment, an IR spectrum of dried Dulbecco's medium is recorded, see Figure 5.6.

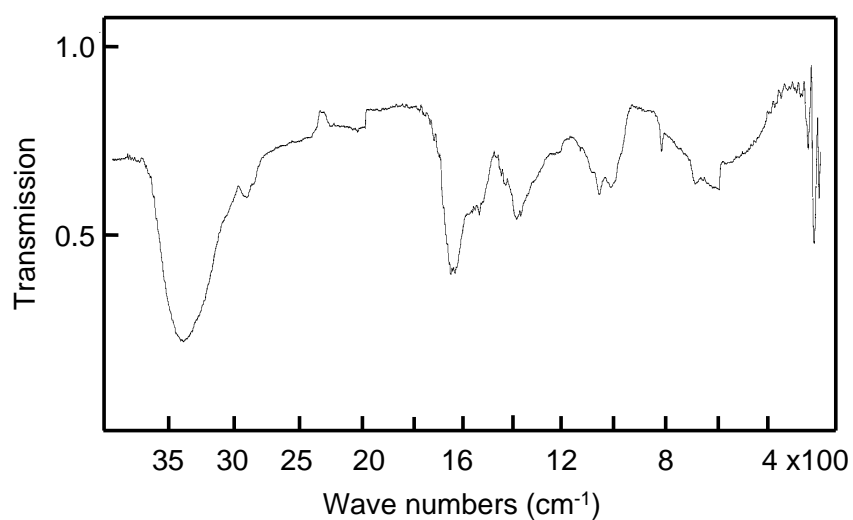


Figure 5.6: Infrared transmission spectrum of Dulbecco's growing medium. The spectrum is recorded with an IR spectrophotometer.

5.4 X-ray photoelectron spectroscopy

The XPS technique is based on the photoelectric effect discovered by H. Hertz⁶ in 1887. It was developed into a surface-analytical tool by Siegbahn et al [223]. High energy photons penetrate the sample and provide enough energy to free core-level electrons from the nucleus attractive force. X-ray sources used in this work include aluminum and magnesium which emit at $E_{Al} = 1253.6$ eV and $E_{Mg} = 1486.6$ eV, respectively. The emitted photoelectrons travel through the material and those which remain unscattered leave the surface with a kinetic energy $E_{(e^-),kin}$ given by

$$E_{(e^-),kin} = h\nu - E_b - \varphi, \quad (5.17)$$

with the photon energy $h\nu$, the binding energy of the electron E_b and the work function φ [224]. Thus, the measurement of the kinetic energy gives the binding energy of the electron. Since E_b is characteristic for all atoms, the spectrum of binding energies for a sample correlates with the atomic composition of the sample's surface. Moreover, E_b exhibits a "chemical shift" for different binding configurations of one atom, so that C-C bonds can be clearly distinguished from C-N bonds, for example.

Not all photoelectrons have a kinetic energy given by equation 5.17. The probability P that the emitted electrons reach the surface without inelastic scattering decreases exponentially with increasing emission depth d :

$$P(d) = \exp \{-d\alpha\}, \quad (5.18)$$

where α is the absorption coefficient. α mainly depends on the kinetic energy of the electrons and on the material they cross before reaching the surface. Table 5.1 lists the attenuation length for electrons with relevant binding energies after reference [225]. Clearly, the XPS technique is highly sensitive to changes in the surface chemistry. Consequently, any contamination of the sample's surface will show up in the spectra and the analysis of the spectra must include an estimate of the effects of surface contamination. Chapter 6.3.2.3 presents a study of polyimide samples which explores the effects of possible surface contamination following cell-culture experiments.

5.4.1 Mathematical fit of spectra

After correcting the XPS data with the transmission function of the analyser system, the spectrum is calibrated with the sensitivity factor of the respective photoelectrons. All samples in this work are dielectrics, ie. non-conductive.

⁶Heinrich Hertz, 1857-1894

Table 5.1: Attenuation length λ for selected chemical elements [225].

Element	Binding energy (eV)	λ (monolayers)
C	284	6
Si	103	10
O	530	5
N	398	6

The emission of photoelectrons results in a charge up of the sample which leads to a shift of the XPS spectrum. In order to obtain the accurate binding energies, the C 1s main peak (C-C bond) at $E_b = 284.6$ eV serves as the reference binding energy and the entire spectrum is shifted accordingly before a fit of the peaks is attempted. For a collection of the binding energies and chemical shifts of the relevant core electrons for this work see the Perkin-Elmer XPS Handbook [226]: C 1s – p. 38-39, N 1s – p. 40-41, O 1s – p. 42-43 and Si 2p – p. 52-53.

All peaks appear on a background noise which must be determined before peaks can be fitted to the measurement data. Assuming that each unscattered electron which forms the element peaks is associated with a certain number of scattered electrons that contribute to the background noise, the background is calculated according to Shirley's method [227],

$$b_i = k \sum_{j=i+1}^N p_j, \quad (5.19)$$

where b_i is the background at a binding energy channel i , p_j is the peak-amplitude and k is a constant. Thus, the background at a given energy is proportional to the total peak area above the background from that energy to higher energies.

In the quantitative evaluation of the spectrum, peaks of chemical bonds (eg. C-C, C=O, C-N) with known binding energies are assigned to the observed peaks (eg. C, N, O) in the spectrum. The integrals of the bond peaks are calculated and their contribution to the overall peak of a certain element is determined. Similarly, the peak areas of all elements found in the sample gives the atomic composition near the sample's surface. Thus, in this work, $S(X)$ with X = C-N subpeak, for instance, denotes the subpeak concentration in the total peak area of an element and the notation $\int X$ with

X = Si, O, N or C is used to give the concentration of an element in the total spectrum of the relevant C, N, O, Si or C, N, O elements. Only the described (*relative*) concentrations of peaks are quantitatively determined. The *absolute* peak areas are not compared. Figures 5.7 and 5.8 (a), (b) illustrate the general fitting procedure for C 1s and O 1s & N 1s, respectively. Shirley's method gives the curved background onto which peaks are fitted

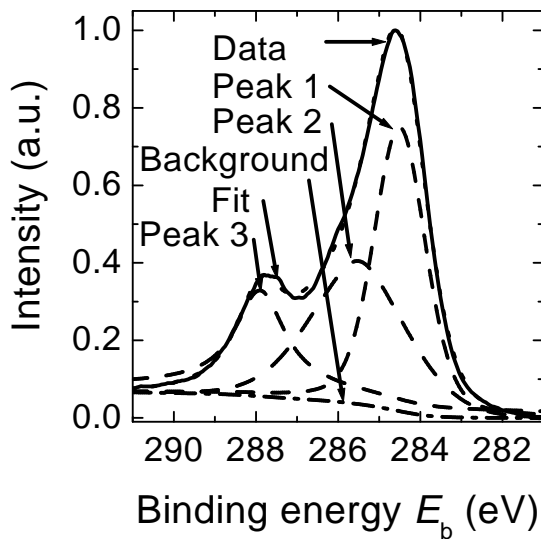


Figure 5.7: Example for fitting procedure of XPS spectra: C1s of Polyimid sample after HeLa-celltest.

that correspond to suspected binding configurations. In order to maintain transparency and comparability, only unambiguous bond peaks are included in the fitting procedure. Moreover, only peaks that the XPS method (and the detector) can truly resolve are shown and any of the given peaks may in reality comprise sub-peaks of chemical bond configurations with small binding energy differences.

Each peak consists of a Gaussian and a Lorentzian component. The mathematical fitting algorithm minimizes the χ^2 between the measured data and the function Y,

$$\begin{aligned}
 Y &= m_1 * G_1 + (1 - m_1) * L_1 \\
 &+ m_2 * G_2 + (1 - m_2) * L_2 \\
 &+ m_3 * G_3 + (1 - m_3) * L_3 + y_0,
 \end{aligned} \tag{5.20}$$

with m denoting the Gaussian portion of a subpeak, $0 \leq m_{1,2,3} \leq 1$, and the terms $G_{1,2,3}$ and $L_{1,2,3}$ representing the Gaussian and Lorentzian distri-

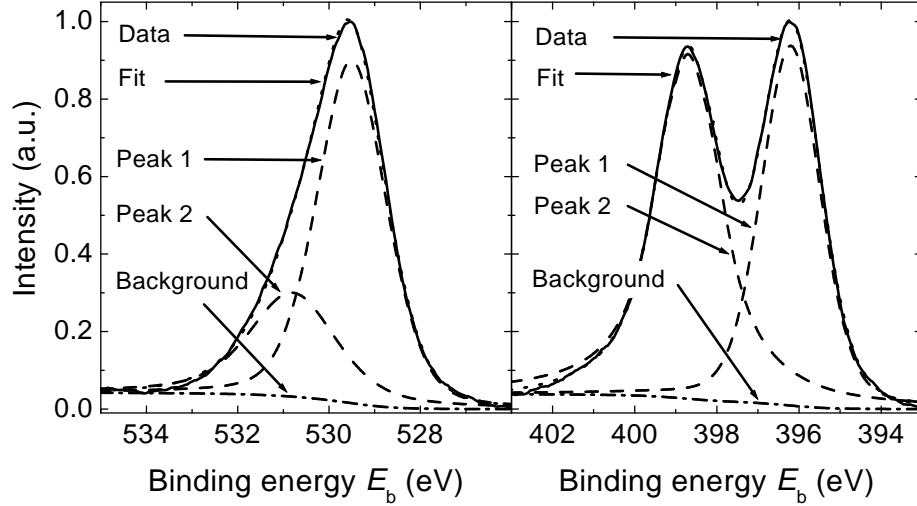


Figure 5.8: Example for fitting procedure of XPS spectra: (a) O1s of Polyimide sample after HeLa-cell test. (b) N1s of SiN_x sample after Marshall-cell test.

butions,

$$G_{1,2,3} = \frac{A_p}{w\sqrt{\pi/2}} e^{-2\frac{(E_b - E_c)^2}{w^2}}, \quad (5.21)$$

$$L_{1,2,3} = \frac{2A_p}{\pi} \frac{w}{4(E_b - E_c)^2 + w^2}, \quad (5.22)$$

with w denoting the full width at half maximum (FWHM), A = area of the peak, E = binding energy (x-axis) and the center of the peak E_c . The sum of the three peaks gives the overall fitting curve which is in good agreement with the measured data.

The Si core electrons of the 2p orbital can occupy two possible energetic states reflecting the parallel or antiparallel vectors of the spin (either $s = +\frac{1}{2}$ or $-\frac{1}{2}$) and orbital angular momentum ($l_{oam} = 1$) of the electrons. The spin-orbit-coupling leads to two values for the total angular momentum $j = l + s$ and the energy levels of the Si electrons are designated as 2p 1/2 and 2p 3/2. The energy separation is of the order of one eV and the area ratio of the 2p 1/2 and 2p 3/2 peaks is 1:2 [224]. Consequently, all Si 2p peaks exhibit an unsymmetry, i.e. a slight "shoulder" towards the high energy side, see Si 2p spectra of SiN_x in section 6.1.3.1 and Si 2p spectra for BCB in section 6.2.2.

5.4.2 Repeated measurements on *one* PI sample

The X-ray irradiation during the XPS measurement is sufficient to break chemical bonds and thus alters the surface chemistry, particularly of polymer samples. In order to assess the radiation damage, Figures 5.9 and 5.10 (a), (b) depict a time-series of C 1s and O 1s & N 1s spectra, respectively, of **one** sample. The Al- and Mg- sources are alternately used because the experiment was originally aimed at detecting spectra variations between both X-ray sources. The sample is treated with control medium for approx. 10 d,

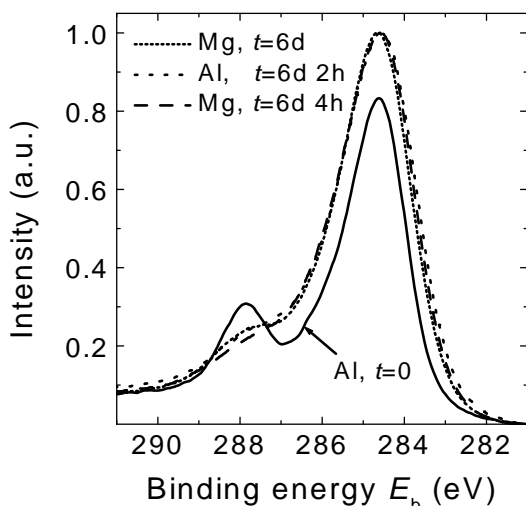


Figure 5.9: Series of C 1s XPS spectra on **one** polyimide sample. Al- and Mg-X-ray sources alternate. Time after the first measurement indicated.

followed by trypsinization (any PI sample can be used for the purpose of this experiment). There is no air-break between the measurements.

The first spectrum, Al-source, $t = 0$, depicts the typical bond configurations of co.-me. treated PI samples, see section 6.3.2. The following three spectra are all recorded six days later with a time-interval of $t = 2$ hours. Every single measurement includes approximately 50 cycles. The total carbon content $\int C\ 1s$ increases with time: $\int C\ 1s$ ($t = 0$) $\approx 70\%$ \rightarrow $\int C\ 1s$ ($t = 6d$) $\approx 79\%$. Moreover, the C-C peak / C=O peak ratio increases from $R_{C-C/C=O} \approx 2.7$ for $t = 0$ to $R_{C-C/C=O} \approx 4.9$ for $t = 6$ days ($E_{g,C=O} \approx 288$ eV). The total oxygen content $\int O\ 1s$ decreases simultaneously from $\int O\ 1s$ ($t = 0$) $\approx 17\%$ \rightarrow $\int O\ 1s$ ($t = 6d$) $\approx 12\%$. Similarly, $\int N\ 1s$ decreases from $\int N\ 1s \approx 12\%$ \rightarrow $\int N\ 1s$ ($t = 6d$) $\approx 9\%$. The spectral variations between both X-ray sources are similar to the margin of error of $c_{moe}^{abs} \approx \pm 0.5\%$ (not shown for the O 1s and N 1s spectra). A

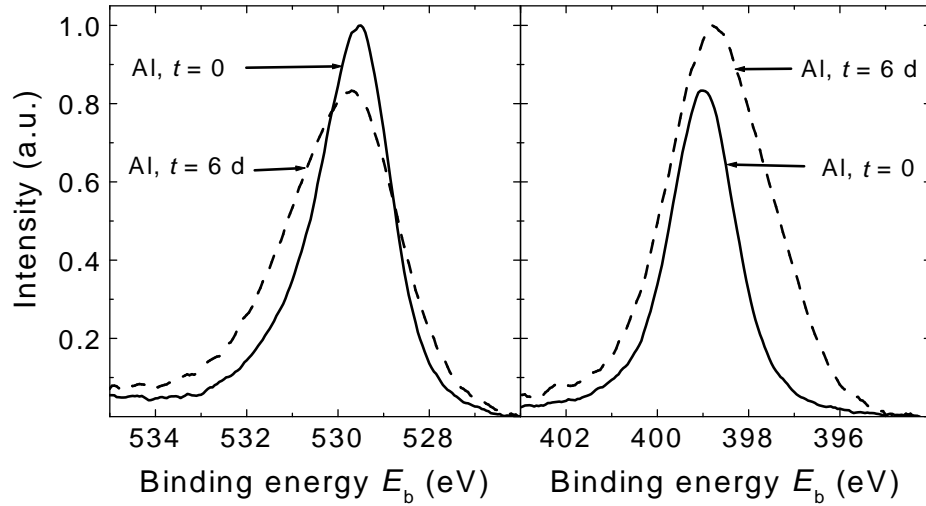


Figure 5.10: Series of XPS spectra on **one** polyimide sample. Al- and Mg-X-ray sources alternate. Time after the first measurement indicated. (a) O 1s. (b) N 1s.

more detailed analysis of the radiation damage in polyimide is not necessary for this work. However, it is important to note that an XPS analysis of a polymer sample can only be recorded once for each sample if the (excellent) comparability of the spectra is to be maintained. All XPS measurements in this work are performed with similar measurement times, hence all samples are exposed to similar radiation doses.

Chapter 6

Experimental results and discussion

The previous chapters showed the need for better long-term biostability of encapsulation materials for retinal implants. Alternative materials are proposed along with evaluation techniques aimed at detecting material degradation at an early stage after the samples are exposed to in-vitro cell cultures.

The first section (6.1) of this chapter presents the results of the material tests of the inorganic $\text{SiO}_x:\text{C}/\text{SiN}_x$ layers. Following a description of the electronic behavior of the layer, the material is analysed in terms of its chemical composition using FTIR and XPS. Both complementary techniques show a decrease of the total Si–N bond concentration after cell culture treatment and a model for the degradation process is presented.

In the second and third section, (6.2), (6.3), the results of the tests of both organic polymers are given. FTIR and XPS measurements point to alterations in the materials' surface chemistry after short-time exposure to the control medium. A sequence of water-rinse experiments explores the possible adhesion of control medium residues on the polyimide surface. The results of the impedance spectroscopy indicate a transient diffusion-like process when the samples are submersed in an electrolyte after they have been hot-oven sterilized. A physical model for the surface region of the polyimide and a modified equivalent circuit is described in order to explain the time-dependent impedance spectra.

6.1 Inorganic $\text{SiO}_x\text{:C/SiN}_x$

6.1.1 Impedance spectroscopy

The inorganic $\text{SiO}_x\text{:C/SiN}_x$ layers exhibit a thickness $d_{io} \approx 200 \times 10^{-9}$ m. From equation 5.1 for a plane capacitor, a bulk capacitance C_{io} , $io =$ inorganic, of the order of $C_{io} \approx 2 \times 10^{-8}$ F is to be expected. The theoretical bulk resistivity R_{io} is $R_{io} \geq \times 10^{12}$ Ω . Thus, a second, series connected RC element which might origin in a distinct surface layer with a thickness of the order of several nm cannot appear in the impedance spectrum in the available frequency range $f = 10^{-1} \dots 3 \times 10^5$ Hz. Consequently, the IS technique mainly serves to evaluate the pin-hole density of the bulk $\text{SiO}_x\text{:C/SiN}_x$ layers which correlates with the shunt resistance R_{io} .

Figure 6.1 displays the Bode plot of recorded impedance data of a sterilized sample and three fit curves. The spectrum does not change over time after the assembly of the electrolyte cell. Fit (A) is obtained using the equiv-

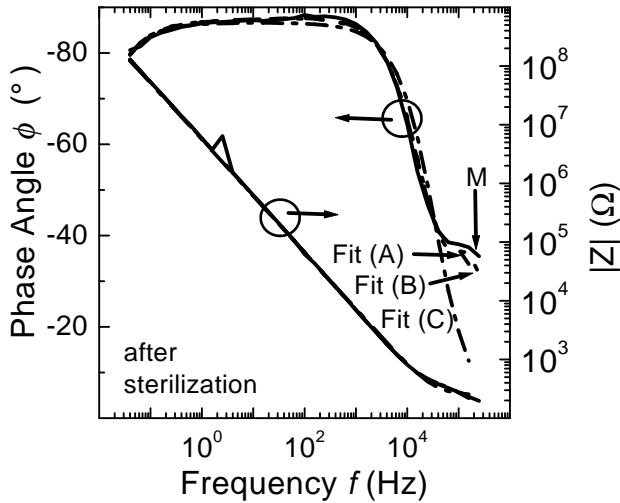


Figure 6.1: Impedance spectra of a $\text{SiO}_x\text{:C/SiN}_x$ sample. (M) Recorded spectra after sterilization of the sample. Fit (A), (B), (C) refer to numerical fits of the measurement data using three different equivalent circuits, see text for details.

alent circuit depicted in Figure 5.2. For fit (B) the Helmholtz $R_{HH}C_{HH}$ element is omitted and the shunt resistance R_{de} of the $\text{SiO}_x\text{:C/SiN}_x$ set $R_{de} = \infty$. The geometric R_gC_g element is set according to the estimation given in chapter 5.2.2. Both resulting fits are hardly distinguishable. Both

fits yield a capacitance of the $\text{SiO}_x\text{:C/SiN}_x$ layer $C_{io} = 2 \times 10^{-7}$ F. Fit (A) gives $R_{de} \approx 10^{11} \Omega$. Neither the HP- nor the Schlumberger measurement unit can resolve smaller current amplitudes, hence the fitted value for R_{de} must be considered a lowest limiting "estimate". The high shunt resistance indicates a low, possibly zero, pinhole density. A simple Randels equivalent circuit with a series resistance and a parallel RC element results in Fit (C). One Randels circuit cannot simultaneously accommodate the impedance spectrum in the "low" frequency range, $f = 10^{-1} \dots 10^5$ Hz, which is governed by the dielectric, and in the higher frequency range. However, the dielectric's capacitance is reproduced (with slightly less accuracy), $C_{(io),c} \approx 3 \dots 3.5 \times 10^{-8}$ F.

Figure 6.2 shows impedance spectra of sterilized samples (the impedance spectra of untreated and sterilized samples are identical) and samples after cell culture treatment. The characteristics are similar to the above described

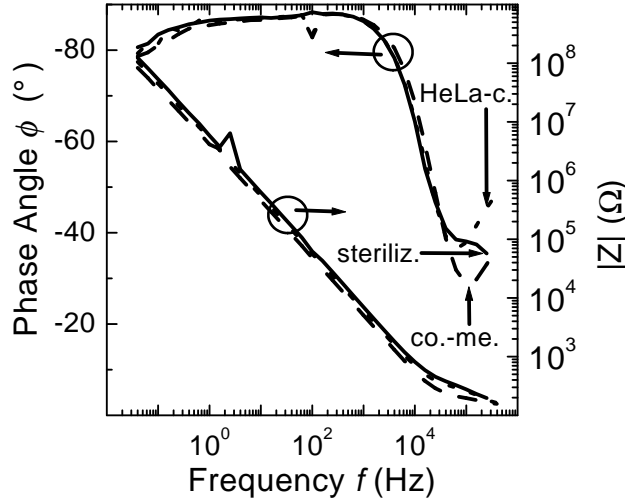


Figure 6.2: Impedance spectra of three $\text{SiO}_x\text{:C/SiN}_x$ samples: One sample after the sterilization, one after two weeks exposure to the control medium and one sample after a HeLa cell culture experiment.

sterilized specimen. However, numerical fits yield slightly higher values for the dielectric's capacitance after HeLa cell culture and co.-me. exposure, $C_{(io),H} \approx 3.5 \times 10^{-8}$ F, $C_{(io),cm} \approx 4 \dots 4.5 \times 10^{-8}$ F, respectively. Moreover, the shunt resistance R_{de} of the HeLa- or cell culture treated samples is of the order of $R_{de} \approx 10^8 \dots 10^9 \Omega$, one or two orders of magnitude lower than for the sterilized sample. The higher capacitance can be explained by a decrease in the thickness of the material. The lower shunt resistance after cell culture

treatment (ie., co.-me. or HeLa cells) indicates an increase of the pin-hole density. Again, more samples ought to be tested to validate this preliminary result.

In the high frequency range above $f \approx 2 \times 10^4$ Hz, the reproducibility of the spectra is low. Consequently, the observed differences between cell-culture treated samples cannot be ascribed to specific fit-parameters.

With regard to the **biostability** of the material, the impedance data alone are not sufficient for a quantitative estimate for the decline of the thickness since the observed trend is close to the general variations in the fitting routine. The analysis of the FTIR and XPS spectra in the following sections includes an estimate for the dissolution rate of the SiN_x top layer in control medium.

6.1.2 Fast Fourier Transform Infrared Spectroscopy – FTIR

Table 6.1 lists the treatments of the two $\text{SiO}_x\text{:C/SiN}_y$ series along with the corresponding XPS- and FTIR measurements. This chapter describes the results of the infrared spectroscopy; the following chapter 6.1.3 presents the XPS observations.

Both $\text{SiO}_x\text{:C/SiN}_x$ series – (1) and (2) – are prepared at the NMI with nominal identical parameters. One sample of each deposition series is exposed to the control medium (co.-me.) after sterilization. For the purpose of providing a reference for cell culture samples treated with trypsin, two control medium samples are also "cleaned" using the enzyme. Two samples (both from deposition run (1)) are analysed after Marshall cells have developed on their surface for approx. two weeks. Similarly, three samples are evaluated after exposure to HeLa- cell culture. All three samples are treated with trypsin in order to reduce cell adhesion to the SiN_x surface before rinsing the samples with PbS and clean water. No correlations between IR characteristics and the storage of the samples in either PbS or at ambient atmosphere, see chapter 4.1.1, are observed.

Figure 6.3 (a), (b) shows the IR spectrum of $\text{SiO}_x\text{:C/SiN}_x$ samples before and after the cell culture experiments. (a) depicts the frequency range $\nu = 800 \dots 1100 \text{ cm}^{-1}$, where the dielectric as well as the wafer substrate exhibit absorption maxima. The baseline correction of the spectrum, mentioned in chapter 5.3, leads to a transmission $t = 1$ (= 100 %) in the lower and upper frequency range of any plotted spectrum. In reality, of course, t ($\nu = 800 \text{ cm}^{-1}$) is much lower than unity. Figure 6.3 (b) shows the frequency range $\nu = 1600 \dots 1770 \text{ cm}^{-1}$. Figure 6.4 presents the IR spectra for

Table 6.1: Overview of XPS- and FTIR analysis of $\text{SiO}_x\text{:C/SiN}_x$ samples. See text for explanation of the XPS measurement series. The "+" signs in the FTIR column indicate the number of samples measured in a treatment- and deposition series group.

Deposition Series	Treatment	XPS series	FTIR
1	no treatment	4	+
2	no treatment	4	-
2	sterilization	4	+
1	17 d co.-me.	1	+
2	17-21 d co.-me.	-	++
2	21 d co.-me., Trypsin	3	+
2	20 min co.-me.	5	-
2	90 min co.-me	5	-
2	6.5 h co.-me.	5	-
2	1d co.-me.	5	-
1	≥ 10 d Marshall-c.	1, 4	++
2	≥ 10 d HeLa-c.	4	-
2	≥ 10 d HeLa-c., Trypsin	1, 3	+++

$\nu = 2800\text{--}3500 \text{ cm}^{-1}$.

The absorption peak around $\nu = 830 \dots 950 \text{ cm}^{-1}$ is attributed to Si-N stretching modes, see [107] for rf magnetron-sputtered SiN_x , [228] for dual-ion-beam deposited $(\text{B}_{0.5-x}\text{Si}_x)\text{N}_{0.5}$, [229, 230, 108, 231] for PECVD deposition, including low-temperature ($T_{(\text{SiN}_x),d} = 120^\circ\text{C}$) PECVD [232], and [233] for tungsten-wire catalytic CVD deposition of SiN_x . It decreases for all samples that are treated with the growing medium. A tendency towards a lowest absorption for the control medium treated samples is observed. No further correlations between Marshall- or HeLa-cell cultures or storage conditions and the magnitude of the Si-N absorption peak can be made.

Between $\nu = 1600 \dots 1700 \text{ cm}^{-1}$, a new absorption peak appears which is probably caused by carbonyl groups (C=O). Many enzymes and vitamins in the growing medium contain C=O groups, see chapter 4.1.1. The IR spectrum of the Dulbecco's medium exhibits a corresponding absorption peak around $\nu = 1590 \dots 1630 \text{ cm}^{-1}$, see chapter 5.3, and it is plausible that the observed absorption on the samples is the result of control medium

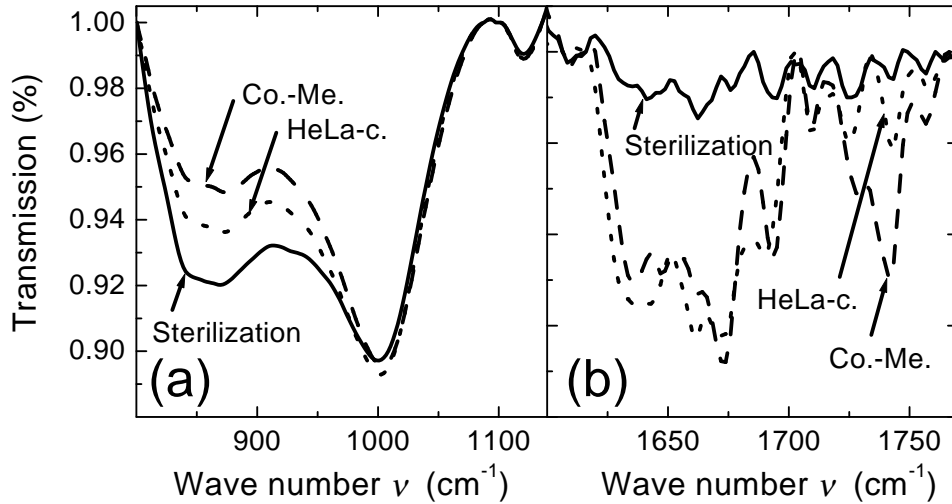


Figure 6.3: FTIR spectra of $\text{SiO}_x\text{:C/SiN}_x$ samples before and after the cell culture experiments: (a) $\nu = 800 \dots 1100 \text{ cm}^{-1}$ (b) $\nu = 1600 \dots 1770 \text{ cm}^{-1}$

left-overs from the rinsing process. For a discussion of the effectiveness of the water rinse with regard to control medium residues, see chapter 6.3.2.3. Again, though control medium treated samples may exhibit a specific sub-peak around $\nu = 1740 \text{ cm}^{-1}$, no clear cut assignment of the peak magnitude to different sample treatments is possible.

Two absorption peaks are observed between $\nu = 2800 \dots 3500 \text{ cm}^{-1}$, peak (A) at $\nu = 2830 \dots 3100 \text{ cm}^{-1}$ and peak (B) at $\nu = 3200 \dots 3450 \text{ cm}^{-1}$, Figure 6.4. Peak (A) can be divided into a subpeak (A-1) at $\nu = 2850 \text{ cm}^{-1}$ and a second subpeak (A-2) at $\nu = 2920 \dots 2970 \text{ cm}^{-1}$ (the latter may be subdivided further into (A-2-a) at $\nu = 2930 \text{ cm}^{-1}$ and (A-2-b) at $\nu = 2960 \text{ cm}^{-1}$). It is probably the result of amine-groups ($-\text{N}-\text{H}_2$) and / or hydroxyl groups ($-\text{OH}$). Peak (A) may be more pronounced for control medium treated samples (higher absorption with three of the four samples). Clearly, though, the number of samples is small, hence the statistics poor and further verification needed. Peak (B) can most likely be attributed to N-H stretching modes [232], [107]. Despite the sputter deposition of the top- SiN_x layer using N_2 and Ar, a certain amount of N-H bonds are present in the untreated material.

Peak (A) as well as peak (B) are found (in almost the exact same shape, though varying magnitudes) in the IR spectra of all inorganic and organic samples that came into contact with the growing medium for prolonged periods of time. In the IR spectrum of the Dulbecco's medium, however, the

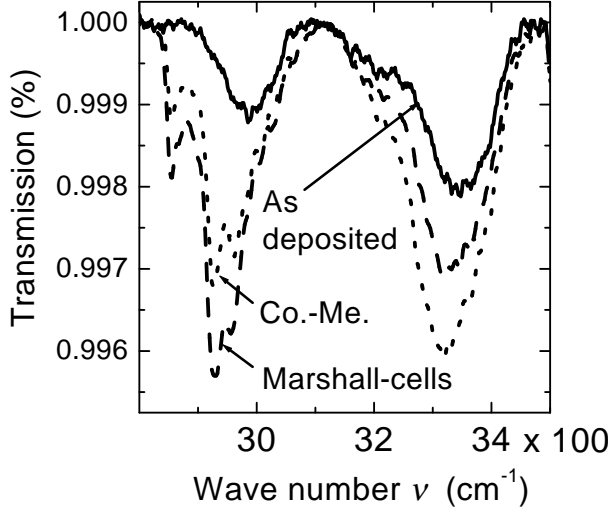


Figure 6.4: FTIR spectra of $\text{SiO}_x\text{:C/SiN}_x$ samples before and after the cell culture experiments: $\nu = 2800\text{-}3500 \text{ cm}^{-1}$

absorption peak which might correspond with the peak (A) of the samples, is much smaller than the broad peak around $\nu = 800 \dots 3700 \text{ cm}^{-1}$. In the medium's spectrum, the smaller peak appears almost overlapped by the main absorption band. Thus, though control medium residues seem a credible explanation for both IR absorption features of the samples, the formation of new bonds including N-X (X = H, O, C), cannot be ruled out.

In the context of the analysis of the **biostability**, the important result of the FTIR spectra is the decrease of the total number of Si-N stretching bonds in the $\text{SiO}_x\text{:C/SiN}_x$ samples. A fit of the Si-N bands in Fig. 6.3 (A) with three Gauss-Lorentz distributions as given by equations 5.20 to 5.22, see "Mathematical fit of XPS spectra" in section 5.4.1, using a straight-line background, shows a reduction of the Si-N stretching bonds by $c_{(IR),\text{Si-N}} \approx -20 \%$ after 21 d HeLa cell culture (plus trypsinization) and a reduction by $c_{(IR),\text{Si-N}} \approx -27 \%$ after 21 d exposure to the control medium (plus trypsinization). Starting from an initial thickness $d_{\text{SiN}_x} \approx 100 \text{ nm}$, the SiN_x layer dissolves by $d_{ss} \approx 1 \dots 2 \text{ nm d}^{-1}$ according to the transmission FTIR data.

FTIR does not reveal how the silicon nitride "crystal" structure is attacked, only the result is observed. The XPS experiments in the next section specifically look at the surface region of the top SiN_x layer in order to explore a degradation mechanism of the material in cell cultures.

6.1.3 X-ray Photoelectron Spectroscopy

In contrast to the volume and surface sensitive FTIR spectroscopy, the XPS analysis of the $\text{SiO}_x\text{:C/SiN}_y$ samples reveals alterations in the chemical composition only in the surface region of the samples, see section 5.4. Thus as long as the top SiN_x layer of the sandwich structure is at least a dozen *nm* thick, see Figure 3.3, the bottom $\text{SiO}_x\text{:C}$ layer does not contribute to the XPS spectra.

Table 6.1 in the previous chapter 6.1.2 lists the treatments of the two $\text{SiO}_x\text{:C/SiN}_y$ series along with the corresponding XPS- and FTIR measurements. In addition to the cell culture treatments described in the FTIR chapter, a short-time series of exposure to the control medium is performed for XPS experiments.

All measurements are carried out using a Mg-X-ray source within an eight months period of time. The measurement series¹ is given in the table to indicate the origin of spectra which are compared in this paragraph. The differences in the quantitative fitting data between equally treated samples (see above) are of the order of 0.3 – 0.5 absolute percentage points of the total element concentration, much lower than the observed variations between samples of different treatment groups.

6.1.3.1 Cell culture experiments

As described in chapter 5.4.1, the quantitative fit of the elemental peaks in the X-ray photoelectron spectrum gives the contribution of each bond configuration to the total peak area of the element. Moreover, when all major peaks in the spectrum are fitted, the share of a specific element in the overall spectrum of the sample can be calculated. The following paragraph describes the observed elemental peaks as they change in the course of the cell culture experiment.

Figure 6.5 (a) and (b) show the carbon C 1s and oxygen O 1s spectra, respectively, of samples before and after cell culture experiments. Figure 6.6 (a) depicts the corresponding silicon Si 2p spectrum and (b) the nitrogen N 1s spectrum. The unsymmetry of the Si 2p peaks is caused by the 2p 1/2 and 2p 3/2 splitting of the energy levels (due to spin-orbit coupling), see section 5.4.1. Both, the Si 2p and the N 1s spectra, show the photoelectrons of the Si-N bonds for the Si and the N, respectively. Table 6.2 summarizes the quantitative data of the XPS-fitting procedure. From an element's peak ratio in the overall spectrum, the element's ratio in the actual composition of the

¹An XPS measurement series consists of up to eight samples which are simultaneously mounted in the XPS chamber.

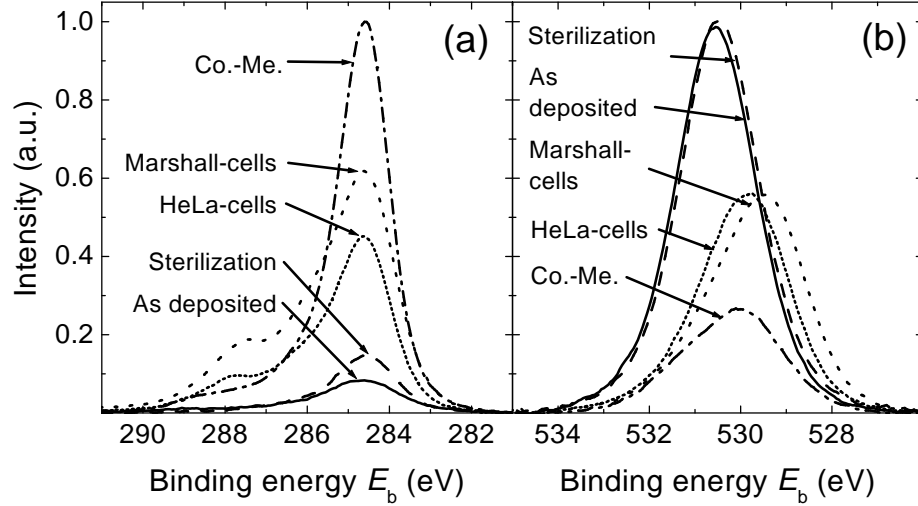


Figure 6.5: XPS spectra of SiN_x samples before and after cell culture experiments: (a) C 1s, (b) O 1s.

sample can be estimated by taking into account the specific attenuation depth of the emitted photoelectrons. For a Mg-X-ray source, the mean attenuation length for Si and N is $\lambda_{\text{Si}} \approx 10$ monolayers and $\lambda_{\text{N}} \approx 6$ monolayers, respectively, see table 5.1, chapter 5.4. Thus, the ratio of the Si and N-peaks in the overall spectrum of the untreated samples indicate a stoichiometric Si_xN_y ($x \approx 3$, $y \approx 4$). Contact of the sample with ambient atmosphere results in the carbon concentration \int C 1s of the untreated sample and of the sample after sterilization (adsorption of carbon containing functional groups). The total oxygen concentration \int O 1s remains unchanged during sterilization.

The samples that are exposed to the control medium exhibit a simultaneous reduction in the total Si and N concentration, \int Si 2p and \int N 1s, respectively, by $c_{\text{Si,N}}^{\text{abs}} \approx -21$ percentage points (pp). The N-Si peak at $E_b = 396.5$ eV decreases and a new peak at $E_b = 398.8$ eV appears as a shoulder on the high energy side of the main N peak. It represents a new bond with an element with a higher electronegativity than N (hence the shift towards higher binding energy), most likely N-Cl. The carbon concentration increases by $c_{\text{C}}^{\text{abs}} \approx 57$ pp and shows only a small shoulder at $E_b = 286$ eV. The oxygen spectrum shows a decrease of the total concentration by $c_{\text{O}}^{\text{abs}} \approx 10$ pp, equivalent to a reduction by $c_{\text{O}}^{\text{rel}} \approx 40\%$ which is similar to the relative decline of the Si and N concentration.

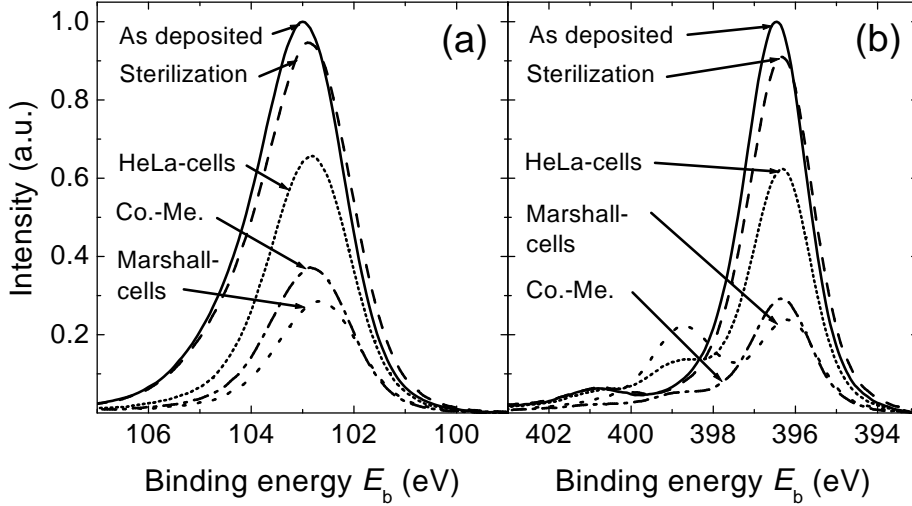


Figure 6.6: XPS spectra of SiN_x samples before and after cell culture experiments: (a) Si 2p, (b) N 1s.

After Marshall- and HeLa cell cultures have developed on the samples, \int Si 2p is reduced by $c_{(M)Si}^{abs} \approx 27$ pp and $c_{(H)Si}^{abs} \approx 13$ pp, respectively. The trypsinization of the HeLa cell-culture leads to a stronger reduction of \int Si 2p by $c_{(H,t),Si}^{abs} \approx 20$ pp which is close to that after Marshall-cellculture and after pure growing medium treatment. The N 1s spectrum exhibits a decrease of \int N 1s by $c_{(H)N}^{abs} \approx 7$ pp after HeLa- and $c_{(M)N}^{abs} \approx 17$ pp after Marshall cellculture, respectively. The N-Cl peak at $E_b = 398.8$ eV, that also appears in the growing medium, increases for both cell cultures. It is most distinct for the Marshall cells sample. The carbon concentration increases after both cell cultures, but does not reach the level (neither in terms of share in the overall element concentration, nor in terms of the total amount of C-bonds detected) of the samples that are exposed to the growing medium without the cells. Moreover, the "living cells" samples exhibit a subpeak at about $E_b = 287.8$ eV plus a more pronounced shoulder between the subpeak and the main peak of C-C. The oxygen concentration is equally reduced after both cell cultures. The decrease is not as strong as after treatment with pure growing medium. Whereas the O 1s peak of the "As deposited" samples is symmetrical, a shoulder appears at the high energy side of the peak for all growing medium or cell culture samples (difficult to see in the plots, yet significant in the quantitative sub-peak analysis.).

Table 6.2: Summary of fit results of XPS spectra: $\text{SiO}_x\text{:C/SiN}_y$ samples before and after celltest-experiments. The listed carbon concentration of the untreated samples represents the maximum value found. Samples treated with trypsin are not included. Where trypsinization affects the spectra, reference is given in the text.

Sample	C 1s \int (%)	O 1s \int (%)	Si 2p \int (%)	N 1s \int (%)	$S(\text{Si-N})(\%)$	$S(\text{N-Cl})(\%)$
as deposited	6	17	37	38	95	–
Sterilization	9	18	36	36	95	–
Control Medium	64	7	15	14	70-80	30-20
Marshall-cells	56	13	11	20	45	55
HeLa-cells	34	12	24	30	70-80	30-20

Regarding the **biostability** of the $\text{SiO}_x\text{:C/SiN}_y$ samples, the XPS spectra demonstrate a chemical degradation of the top SiN_x layer: \int Si 2p and \int N 1s decrease because the carbon concentration \int C 1s increases. As the FTIR analysis reveals a decrease in the total number of Si-N bonds, see section 6.1.2, this XPS result cannot be explained by carbon containing co.-me.- or cell residues on the SiN_x surface. Instead, the Si-N structure is attacked and Si atoms are replaced by carbon. Moreover, the treatment of the $\text{SiO}_x\text{:C/SiN}_y$ samples with Marshall cells leads to a significantly higher reduction of the Si concentration accompanied by the decline in N-Si bonds than is observed for samples treated with HeLa cells.

6.1.3.2 Time series of exposure to control medium

In order to investigate the mechanism that leads to the chemical bonding variations during celltest experiments, a series of $\text{SiO}_x\text{:C/SiN}_y$ samples is exposed to pure control medium in the incubator for various amounts of time, see table 6.1. Matching the observations of the previous cell culture tests, the carbon concentration \int C 1s increases gradually over time while the oxygen concentration \int O 1s decreases (no plots shown). In a similar manner, the total Si concentration \int Si 2p as well as the total N concentration \int N 1s decline, as seen in Figure 6.7 (a) and (b), respectively. The N 1s spectra confirm again the development of the N-X peak at $E_b = 398.8$ eV. That peak is also observed for HeLa cell culture treatments and particularly strong after Marshall cell cultures, see Fig. 6.6. Figure 6.8 displays the total element concentration \int X, X = Si 2p, C 1s, O 1s, as determined from

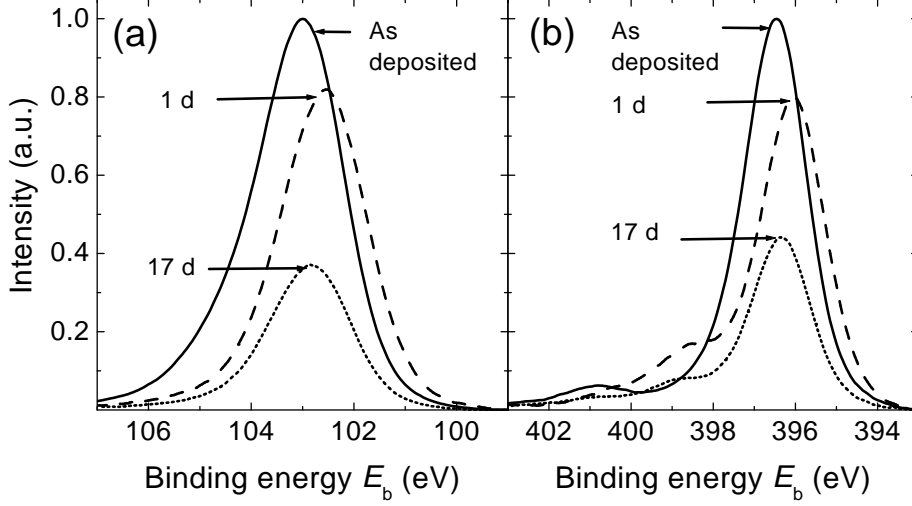


Figure 6.7: XPS spectra of SiN_x samples. Time series of exposure to control medium. (a) Si 2p and (b) N 1s.

the integral of the XPS spectra, versus time of co.-me. exposure. Untreated samples, $t = 0$, exhibit the composition which is listed in table 6.2. After one day, the carbon concentration increases, whereas the silicon and the oxygen concentration decrease. This trend continues as the next available data after more than two weeks show. The element concentration c at any given time is fitted with an exponential function,

$$c = c_0 + a \exp \left\{ -\frac{t_{\text{co.-me.}}}{\tau} \right\}, \quad (6.1)$$

with the initial element concentration c_0 and the prefactor a . The time constant τ for the presented fits is $\tau_{(XPS),\text{Si}} = 2.2$ d, $\tau_{(XPS),\text{O}} = 1.2$ d and $\tau_{(XPS),\text{C}} = -3.5$ d for \int Si 2p, \int O 1s and \int C 1s, respectively. The nitrogen concentration (not shown) can be inferred from the plotted data as \int C 1s, \int O 1s, \int Si 2p and \int N 1s must add up to 100%. However, \int N 1s does not seem to exhibit the exponential behavior described in equation 6.1. The nitrogen concentration remains unchanged at \int N 1s $\approx 36\%$ after one day of treatment before it is reduced to \int N 1s $\approx 14\%$ after two weeks.

The time span t_2 indicates the timeframe where the SiN_x surface composition reaches a new equilibrium and no major changes are observed within the XPS information depth if the samples are exposed to the co.-me. for longer periods of time. t_2 depends on the chemical element: $t_{2,\text{O}} \approx 4$ d, $t_{2,\text{Si,C}} \approx 8$ d.

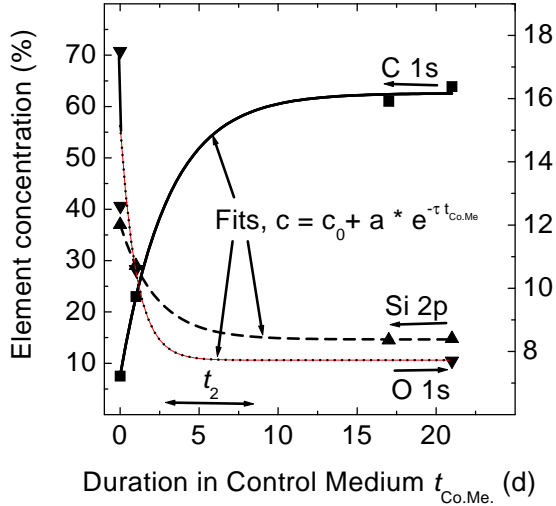


Figure 6.8: The quantitative XPS analysis of $\text{SiO}_x:\text{C}/\text{SiN}_x$ samples reveals changes in the elemental composition with increasing duration of the sample's exposure to control medium. The arrows indicate the ordinate-axis which corresponds to the respective chemical element.

6.1.4 Model for surface degradation

Based on the observed time-behavior of the XPS spectra, Figure 6.9 illustrates a model for the degradation of the SiN_x surface due to co-me. exposure. Following the untreated material (0) at $t = t_0$, three stages of degradation are depicted. In the initial stage t_1 , the uppermost surface layers of the material (1) are attacked by components of the control medium. The chemical resistance of SiN_x strongly depends on the material's composition and structure which are determined by the deposition parameters. Section 3.2.1 describes the deviation of the "real" sputtered SiN_x from the ideal Si_3N_4 crystal depicted in Figure 3.2. Following that characterization, weak bonds are cracked by the control medium and replaced by energetically more stable new C-N bonds. Thus, Si-N bonds with relatively low binding energies are cracked first and a Si-N "skeleton", including C-N components, with relatively high binding energies remains. This model is supported by the transmission FTIR spectra, see chapter 6.1.2, which show a decrease of the total number of Si-N bonds.

As the depth of the affected surface region of the material increases, more photoelectrons are emitted which represent the new surface chemistry. However, the fraction of photoelectrons which reach the surface unscattered decreases exponentially with increasing depth, see equation 5.18 in chapter 5.4. This situation is depicted in the plot of the probability P that a photoelectron e_{ph}^- which is emitted at a certain depth d reaches the surface

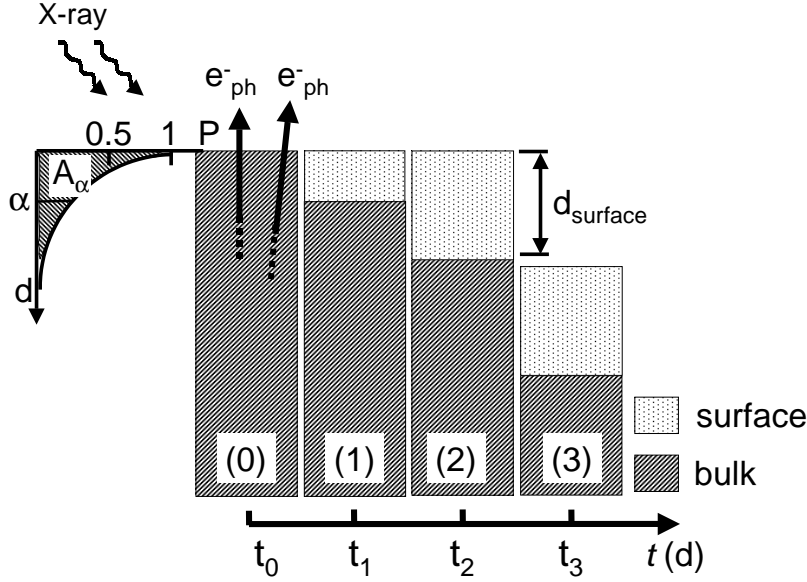


Figure 6.9: Schematic diagram, based on XPS analysis, for SiN_x degradation. The graph plots the probability P for a photoelectron e_{ph}^- emitted at depth d to reach the surface without inelastic collisions. Beginning with the untreated material (0), three stages of degradation are depicted. At $t = t_1$, top monolayers are attacked by the co.-me.. Weak bonds break and the surface composition changes as observed by XPS. From $t = t_2$ on, the thickness of the chemically altered material's surface exceeds the average depth of origin of the photoelectrons which are detected with XPS. $t = t_3$ signals the onset of the progressive dissolution of the SiN_x material.

without inelastic scattering. α represents the absorption coefficient. Whereas $A_\alpha = 63\%$ of all photoelectrons emitted between $d = 0 \dots \alpha$ contribute to the XPS signal, this share drops to 23% for a doubled thickness (not shown in the plot). After $t = t_2$, the surface region of the SiN_x with a depth $d = d_{\text{surf}}$ has been altered by the control medium. Changes in the binding chemistry further into the bulk material cannot be observed with XPS. From t_2 on, the elemental composition of the SiN_x appears constant.

A lower limit for the thickness d_{surf} of the chemically altered SiN_x surface layer can be calculated from the XPS data: For an *ideal binary layer system* where the photoelectrons are emitted from the bottom Si layer and must travel through the top C layer to the surface, the mean free path *MFP* of the Si 2p photoelectrons in the carbon layer and the \int Si 2p and \int C 1s concentrations from the XPS analysis determine the thickness of the top C

layer [225, 234]. Thus the thicker the (in the binary layer model presumed) top C layer, the higher is the carbon concentration and the lower is the Si concentration in the XPS spectrum. The MFP for Si 2p electrons (Mg X-ray source) in carbon is taken from a literature data base [225, 234]. The thickness of the top Si layer d_{tl} is obtained from the following equation,

$$d_{tl} = MFP_{(Si),C} \cos \vartheta \ln \left(1 + \frac{\int C \ 1s}{\int Si \ 2p} \right), \quad (6.2)$$

with the detection angle ϑ of the XPS analyser. For control-medium treated samples, d_{tl} increases from $d_{(tl),t=0} \approx 2.5 \dots 4 \text{ \AA}$ for untreated or sterilized samples to $d_{(tl),t=1 \text{ d}} \approx 10 \text{ \AA}$ after one day and to $d_{(tl),t=17 \text{ d}} \approx 28 \dots 30 \text{ \AA}$ after 17 d. The simple growth of a layer of co.-me. residues cannot explain the decrease of the Si-N bonds observed in transmission FTIR. Moreover, the SiN_x surface is known to degrade when in contact with living brain tissue (observable with unaided eyes after two to three month) [235]. Following the model depicted in Fig. 6.9, a simple carbon cover on the SiN_x surface is dismissed. Hence, the above described ideal binary layer system (with a step function) must be replaced by a smooth interface. Clearly, the thickness of that interface region d_{surf} , Fig. 6.9, is larger than d_{tl} .

The last stage at $t = t_3$ involves the gradual dissolving of the Si-N skeleton. The total thickness of the SiN_x layer decreases while the thickness of the surface region remains constant. At this stage, the XPS signal stays constant until the $\text{SiO}_x\text{:C}$ bottom layer of the $\text{SiO}_x\text{:C/SiN}_y$ sandwich structure is reached.

6.1.5 Summary: $\text{SiO}_x\text{:C/SiN}_y$

Figure 6.10 summarizes the analysis of the biostability of the $\text{SiO}_x\text{:C/SiN}_y$ test samples. FTIR, XPS and impedance spectroscopy show that the $\text{SiO}_x\text{:C/SiN}_y$

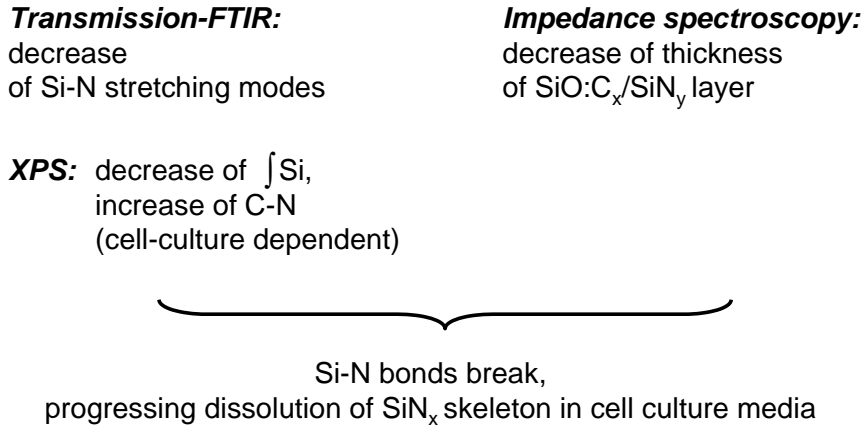


Figure 6.10: Summary of experimental results which show the progressive degradation of the $\text{SiO}_x\text{:C/SiN}_y$ test samples. Surface and volume sensitive transmission FTIR data show a decrease of the Si-N stretching bonds. Surface sensitive XPS gives a more detailed picture of the decrease of Si-N bonds with a simultaneous – cell culture specific – increase in the observed C-N bond density. Impedance spectroscopy indicates a decrease of the $\text{SiO}_x\text{:C/SiN}_y$ layer thickness.

test samples are not biostable. Rather, they dissolve in control medium and cell culture treatment at an approximate rate of $dss \approx 1 \dots 2 \text{ nm d}^{-1}$, according to the FTIR transmission spectra. The XPS analysis shows that the degradation process starts with a surface region in the SiN_x where weak Si-N bonds break and carbon is incorporated into the Si-N skeleton. That surface region reaches a thickness $d_{surf} \geq 30 \text{ \AA}$ after approximately four to eight days. The impedance spectroscopy confirms the decrease of the total layer thickness but a quantitative estimate for the decrease from the impedance data alone is less accurate than based on the FTIR and XPS data.

6.2 Benzocyclobutene

In analogy to the experiments with the $\text{SiO}_x\text{:C/SiN}_y$ samples, table 6.3 lists the treatments of three BCB sample series along with the corresponding XPS- and FTIR measurements. Both BCB series – (1) and (2) – are prepared at

Table 6.3: *Overview of XPS- and FTIR analysis of BCB samples. For the XPS measurements, the "measurement series" is given, see explanation in chapter 6.1.3. The "+" signs in the FTIR column indicate the number of samples measured in a treatment- and deposition series group.*

Deposition-Series	Treatment	XPS series	FTIR
1	no treatment	1, 2, 3	+
2	no treatment	6	+
1	sterilization	3	+
2	sterilization	-	+
1	$\geq 10\text{d}$ co.-me.	2	++
2	$\geq 10\text{d}$ co.-me.	4, 5	++
3	10 s co.-me.	7	-
3	20 min co.-me.	7	+
3	90 min co.-me.	7	+
3	6.5 h co.-me.	7	+
3	1d co.-me.	7	+
1	10d Marshall-c.	2	++
1	17d Marshall-c.	3, 3	++
2	17d HeLa-c.	4, 5	++

the *ipe* with nominal identical parameters with regard to the (liquid) resin and the spinning process. The final curing temperature is also kept constant, but the temperature ramp (i.e., $T(t)$) varied slightly, see chapter 3.2.2.

One of the XPS and FTIR samples of deposition series (2) that are exposed to the controm medium and HeLa cells, respectively, is cleaned with Mucasol (2%) after each treatment. This "cleaning" procedure neither significantly affects the XPS spectra nor the FTIR absorption bands.

6.2.1 FTIR

The presented FTIR spectra focus again on absorption bands that change in the course of the cell culture experiments. Figure 6.11 shows the IR absorption spectra for the frequency range $\nu = 950 \dots 1900 \text{ cm}^{-1}$. Two

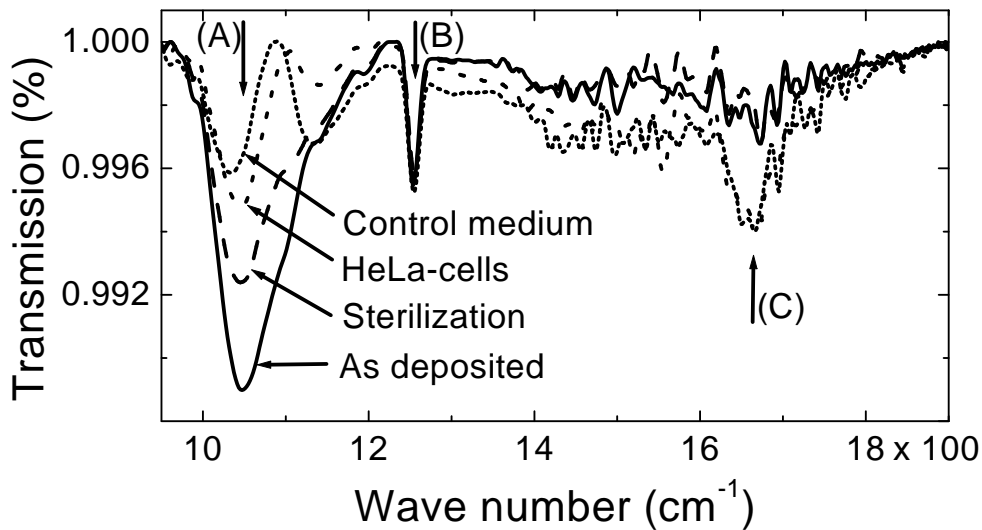


Figure 6.11: FTIR spectra of BCB samples before and after celltest experiments.

characteristic absorption peaks for BCB are observed [190]: Peak (a) at $\nu \approx 1050 \text{ cm}^{-1}$ which is attributed to the stretching vibrations of the ether Si–O–Si bonds [236, 237] and peak (b) at $\nu \approx 1250 \text{ cm}^{-1}$ which is attributed to the stretching vibrations of the silicon methyl group (Si–CH₃) [236, 238]. Both groups are labelled in the structural formula of the BCB monomer, see chapter 3.2.2, Figure 3.4, as (iii) and (ii), respectively.

Peak (a) decreases significantly after the cell culture experiments, particularly when the samples are only exposed to the control medium. Assuming that the broad original peak is composed of subpeaks (with the resulting total maximum absorption at $\nu \approx 1050 \text{ cm}^{-1}$), the drop in absorption is strongest at $\nu \approx 1070\text{--}1080 \text{ cm}^{-1}$. The cleaning of the samples with Mucosol after the water rinse does not significantly alter the IR spectra. Peak (b) may drop slightly after treatment with the growing medium, but further verification is needed. Peak (c) is very similar to the absorption band in Figure 6.3 (b). Again, it most likely represents carbonyl groups C=O which either originate from control-medium residues, or have been newly formed on the BCB surface. The virgin BCB structure does not contain C=O groups.

In an attempt to emulate a possible oxydation of the BCB surface during exposure to living cells, several samples are exposed to a stream of ozone (O_3) and simultaneously irradiated with UV light for 3 ... 5 min (Hg lamp, $O_3 = 100 \text{ l min}^{-1}$). The IR spectra show unmistakably $-COOH$ bands at $\nu \approx 1715\text{--}1720 \text{ cm}^{-1}$ (spectra not shown). Since no such carboxyl groups appear in the spectra after cell culture tests, the oxydation of the material can be excluded from the degradation process.

Figure 6.12 depicts the spectral range $\nu = 2800\text{--}3500 \text{ cm}^{-1}$. As mentioned for the $SiO_x:C/SiN_y$ samples, see Figure 6.4, the absorption bands around $\nu = 2800\text{--}3050 \text{ cm}^{-1}$, peak (d), and $\nu = 3200\text{--}3450 \text{ cm}^{-1}$, peak (e) appear for all samples treated with the control medium. In contrast to the $SiO_x:C/SiN_y$ samples, the absorption band (e) which is attributed to N-H stretching modes, does not exist before cell culture treatment because the "pristine" BCB network does not contain N. For further explanations see chapter 6.1.2.

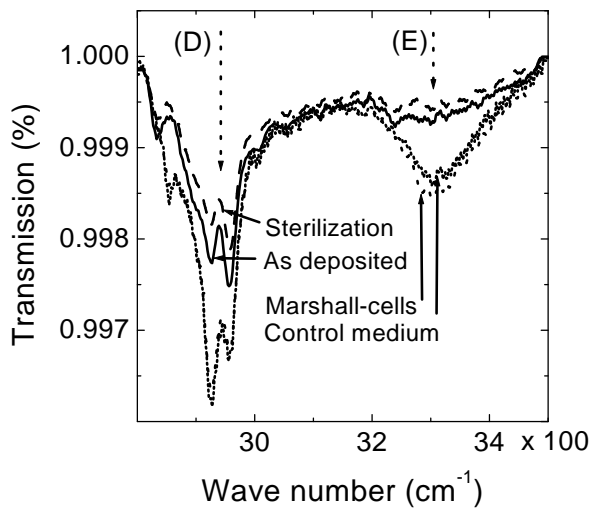


Figure 6.12: FTIR spectra of BCB samples before and after cell test experiments.

6.2.2 XPS-analysis

The XPS analysis of the BCB samples follows the same procedure as for the $\text{SiO}_x\text{:C/SiN}_y$ samples. The first paragraph focuses on the results of the cell culture experiments. In a second paragraph, the findings of a short-time series of exposure to control medium are presented.

Figure 6.13 (a) presents the C 1s and (b) the O 1s spectra of BCB samples before and after cell test experiments. In a similar manner, Figure 6.14 (a), (b) shows the binding energy spectra for Si and N, respectively. The

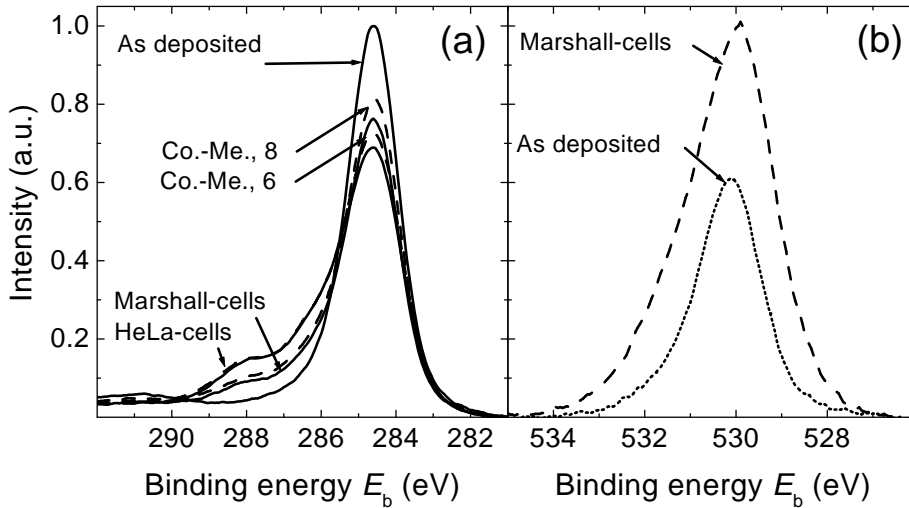


Figure 6.13: XPS spectra of BCB samples before and after cell test experiments: (a) C 1s and (b) O 1s.

elemental atomic composition of the "as deposited" BCB layers is as follows: $\int \text{C } 1s = 86\%$, $\int \text{O } 1s = 6\%$, $\int \text{Si } 2p = 8\%$. All values represent the average over the examined samples, see table 6.3. If not indicated otherwise, the variation between corresponding values of separate samples is of the order of $c_{moe}^{abs} = \pm 0.5\%$. This composition is in good agreement with the chemical composition of the BCB structure as depicted in Figure 3.4 and with references [236, 149, 184]. The almost symmetrical C 1s peak exhibits an C-C component at $E_b = 284.6$ eV and a marginal second peak at $E_b = 290.8$ eV which is attributed to $\pi-\pi^*$ transitions (π and π^* being the binding and non-binding molecular orbit of the delocalized electrons in the benzene ring, see chapter 3.2.3) [239, 150]. The O 1s peak for the Si-O-Si linkage is almost symmetrical, with a small component at the high-energy side representing a number of O-C bonds [184]. The Si atom is bonded to oxygen, Si-O-Si,

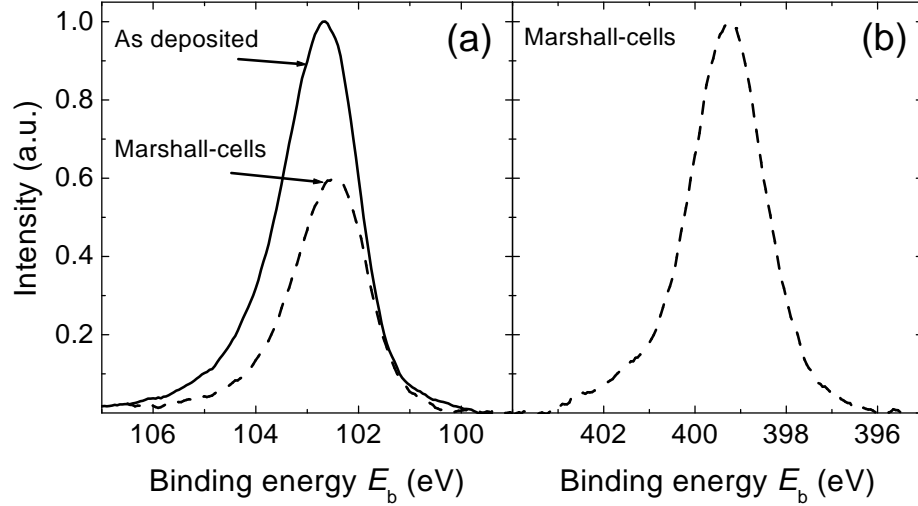


Figure 6.14: XPS spectra of BCB samples before and after cell test experiments: (a) Si 2p and (b) N 1s.

which gives a single peak at $E_b = 102.5$ eV. However, as observed for the Si 2p spectra of the SiN_x , see section 6.1.3.1, the spin-orbit coupling leads to a split of the energy levels into 2p 1/2 and 2p 3/2 which explains the unsymmetry of the Si peak, see also section 5.4.1. Untreated BCB does not contain nitrogen. One of the four BCB samples does exhibit a N peak ($\int \text{N } 1s = 5\%$), indicating a certain contamination of the sample.

The sterilization of the BCB samples has no discernable effect on their chemical bonding configurations. After the samples are exposed to the growing medium, the small $\pi-\pi^*$ subpeak disappears. The total carbon concentration $\int \text{C } 1s$ decreases by about $c_C^{abs} \approx -6 \dots 13 \%$. The reduction unmistakably correlates with the deposition series of the BCB, whereas the addition of living cells does not seem to have an effect: Series (1) samples treated with Marshall cells and the control medium show a $c_{(M),C}^{abs} = -6 \%$ reduction, series (2) samples with HeLa cultures and co.-me. a $c_{(H),C}^{abs} = -13 \%$ decline in $\int \text{C } 1s$. The deposition conditions also affect the shift of the subpeak contributions from the C-C main peak towards newly developing C-N and C=O subpeaks at $E_{(b),C-N} \approx 286$ eV and at $E_{(b),C=O} \approx 288$ eV, which form a shoulder at the high energy side of the peak [151, 149, 184]: The ratio $R_{C-C/(C-N+C=O)}$ between the C-C main peak and the sum of the C-N and C=O subpeaks reaches $R_{C-C/(C-N+C=O)} \approx 2.5$ for series (1) and $R_{C-C/(C-N+C=O)} \approx 1.7$ for series (2). Again, no distinction between co.-me.

treated samples and such with living cells can be made. The oxygen peak grows as a result of the cell tests. Again, the change of magnitude is determined by the deposition series and independent of living cells, $c_{\text{O}}^{\text{abs}} \approx 4\%$ for series (1) and $c_{\text{O}}^{\text{abs}} \approx 8\%$ for series (2) (not shown in the plot). With increasing O concentration, the portion of the subpeak (see above) increases, pointing to the formation of O-C bonds. Irrespective of the addition of living cells, the treatment with growing medium reduces the Si peak to $\int \text{Si } 2\text{p} \approx 4 \dots 5\%$ (only shown for Marshall cell treatment). The shape of its slight asymmetry, see above, remains constant. However, the formation of Si-N bonds – with a very similar binding energy – cannot be ruled out. The emerging N peak is almost symmetrical and can be attributed to the formation of C-N bonds, $\int \text{N } 1\text{s} \approx 5\%$ for series (1) and $\int \text{N } 1\text{s} \approx 8 \dots 9\%$ for series (2) (exemplarily shown for Marshall cell treatment).

6.2.2.1 Short-time exposure to control medium

Similar to the $\text{SiO}_x\text{:C/SiN}_x$ material, short-time control medium tests are performed in order to examine the kinetics of the BCB-surface reactions. For each exposure time to the co.-me., only one sample is XPS-analysed. The margin of error for XPS measurements of identically treated samples is low, see above. However, particularly at $t = 10$ s, errors with regard to the exact time of exposure (including the time between taking the sample out of the glass dish and beginning to rinse the sample in water) and with regard to the reproducibility of the water rinse aggravate. As a consequence, the following *quantitative* observations should be treated with caution.

Figure 6.15 (a) displays the experimental results for the C 1s peak and (b) for the O 1s peak. The Si 2p and N 1s spectra are shown in Figure 6.16 (a) and (b), respectively. $\int \text{C } 1\text{s}$ reduces by $c_{\text{C}}^{\text{abs}} \approx -3\%$ after 10 s and by $c_{\text{C}}^{\text{abs}} \approx -6\%$ (final status for this deposition series) after 90 min. Deconvolution of the C 1s peaks reveals subpeaks at $E_b \approx 286$ eV, attributed to C-N bonds, and $E_b \approx 288$ eV for C=O bonds, already after $t = 10$ s exposure to the control medium. With a decreasing total amount of carbon, the ratio $R_{\text{C-C}/(\text{C-N}+\text{C=O})}$ of those subpeaks to the main peak at $E_b = 284.6$ eV increases. A final ratio $R_{\text{C-C}/(\text{C-N}+\text{C=O})} \approx 2.2$ (for deposition series (3)) is reached after $t = 20$ min. The peak at $E_b \approx 290.8$ eV has disappeared after 10 s. The oxygen peak increases by $c_{\text{O}}^{\text{abs}} \approx 4\%$ after 10 s and by $c_{\text{O}}^{\text{abs}} \approx 5\%$ after 90 min. The final concentration of nitrogen is reached after 20 ... 90 min. Three quarters of $\int \text{N } 1\text{s}$ are already found after 10 s. The silicon concentration declines by $c_{\text{Si}}^{\text{abs}} \approx -5\%$ to $\int \text{Si } 2\text{p} \approx 3\%$ in the first 10 s of control medium exposure. As several samples exhibit $\int \text{Si } 2\text{p} \approx 5\%$ after prolonged exposure, eg. after 1.5 h, the lower silicon concentration of

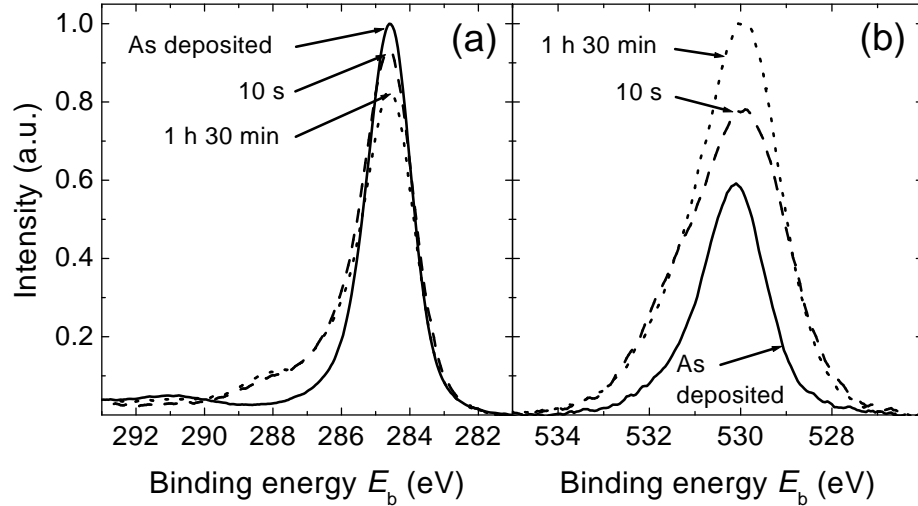


Figure 6.15: XPS spectra of BCB samples before and after short-time control-medium exposure: (a) C 1s and (b) O 1s.

the 10 s treated sample is considered a sample-specific exception.

6.2.3 Impedance spectroscopy

As mentioned in chapter 3.2.2, visual examination of the "as deposited" ultra-thin BCB layers reveals morphological inhomogeneities such as grain-like structures, rings, etc. In sharp contrast to the polyimide material, see chapter 6.3.4, the impedance spectra of the BCB samples are much less reproducible. Samples (A) that are treated with the control medium or exposed to PbS for several days, and have their surface dried using a nitrogen pistol immediately before the assembly of the electrochemical cell, exhibit an evolution of the impedance spectra over time which cannot be explained (i.e., quantitatively fitted) in terms of the equivalent circuit of Figure 5.2. BCB specimen (B) that are not exposed to any electrolyte before the electrolyte cell setup feature a different, more reproducible time-behavior of the impedance spectra.

Due to the lack of reproducibility no quantitative analysis of the impedance spectra for BCB samples is attempted. The time characteristics of the spectra of samples (A) and (B) points to a water-uptake mechanism of the polymer. Though the analytical model which is given in chapter 6.3.4.3 can only be quantitatively validated for polyimide samples, it may in principle also hold for the BCB polymer. Morphologically more homogeneous samples and pos-

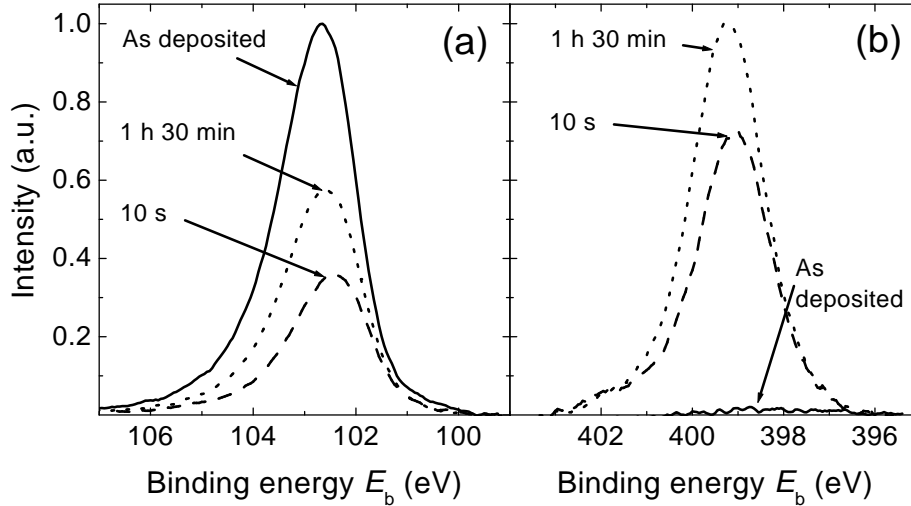


Figure 6.16: XPS spectra of BCB samples before and after short-time control-medium exposure: (a) Si 2p and (b) N 1s.

sibly an alternative measurement setup are needed to further investigate the electronic behavior of this material.

6.2.4 Summary: BCB

Benzocyclobutene is clearly more **biostable** than the $\text{SiO}_x\text{:C/SiN}_y$ sandwich structure. Although the volume- and surface sensitive FTIR analysis shows a decline of the total number of O–Si–O groups, see Fig. 6.11 and the BCB monomer structure in Fig. 3.4, those changes are one order of magnitude smaller than the decline of the Si–N bonds observed for the $\text{SiO}_x\text{:C/SiN}_y$ material. Moreover, the FTIR peak representing the Si–CH₃ group remains constant. The XPS analysis reveals only minor changes in the surface composition: In contrast to the untreated samples, those that are exposed to the cell culture contain small amounts of nitrogen which is bonded to carbon. The slight decrease of the \int Si 2p concentration as well as the decrease of the C–C main peak can be explained by control medium which penetrates into the surface region of the material. The resulting smooth interface in effect constitutes a "diluted" BCB structure, and co.-me. components, see Appendix 7.1, contribute to the XPS spectrum. See also section 6.3.2.3 which presents a discussion of co.-me. residues on polyimide samples and co.-me. penetration into the surface region of polyimide.

6.3 Polyimide

Similar to the $\text{SiO}_x\text{:C/SiN}_y$ – and BCB samples, table 6.4 lists the polyimide samples for the XPS and FTIR analysis. All samples are prepared at the NMI in the same deposition run. Moreover, with the exception of the sample that is exposed to living HeLa cells, all FTIR- samples are cut from the same wafer.

In contrast to the $\text{SiO}_x\text{:C/SiN}_y$ - and BCB samples, only one PI sample per treatment is analysed with XPS and FTIR. Only of the untreated and sterilization samples, the XPS spectra of two test specimen are recorded in different XPS series. The FTIR spectra are recorded twice in order to find out about the possible "evaporation" of components on the PI surface. Between the first and the second measurements, the samples are stored in ambient atmosphere under low-light conditions for four days. As the second measurement does not reveal spectral changes, the chemical groups on the PI surface after cell culture treatment are stable in ambient atmosphere.

Table 6.4: *Overview of XPS- and FTIR analysis of polyimide samples. For the XPS measurements, "measurement series" is given, see explanation in chapter 6.1.3. All FTIR measurements are performed twice, see text.*

Treatment	XPS series	FTIR
no treatment	1, 5	
sterilization	1, 6	2x
≥ 10 d co.-me.	1	2x
≥ 10 d co.-me., trypsin	1	2x
10d Marshall-c.	1	2x
10d Marshall-c., trypsin	1	2x
17d HeLa-c.	1	2x
17d HeLa-c., trypsin	1	2x
Glutamine	5	–
Glukose	5	–
Glutamine + Glukose	5	–
short-time co.-me., rinse	6	–
PbS, rinse	6	–

6.3.1 FTIR Spectroscopy

Figure 6.17 shows the FTIR spectra of polyimide samples before and after cell test experiments in the spectral range between $\nu = 900 \dots 1900 \text{ cm}^{-1}$. The sterilized sample exhibits the PI specific absorption bands which are

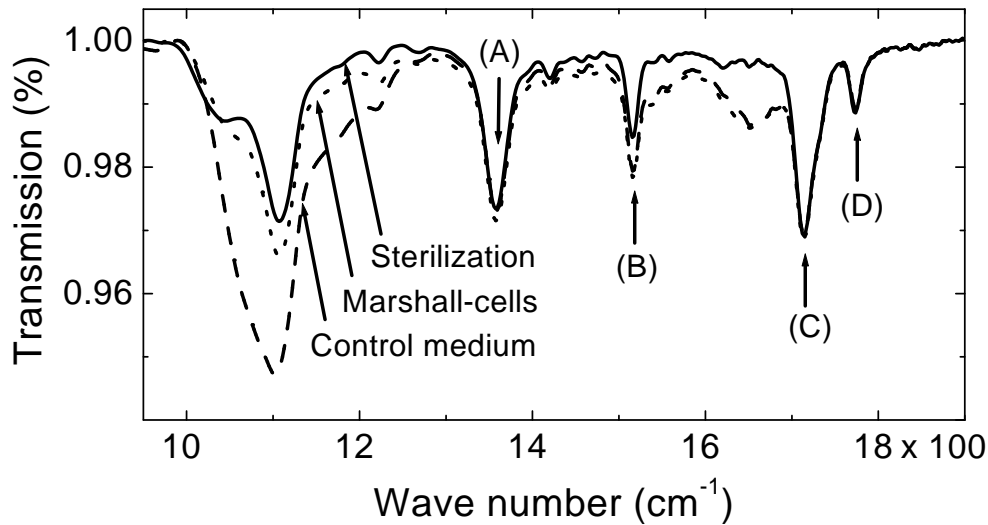


Figure 6.17: FTIR spectra of polyimide samples for $\nu = 950 \dots 1900 \text{ cm}^{-1}$.

widely published [240, 172, 146, 241, 242, 163, 243, 170, 244, 176, 245, 246, 144, 160]: In-plane C-H vibrations on the aromatic rings cause also absorption at $\nu = 1023, 1082, 1125$ and 1224 cm^{-1} according to reference [146] and at $\nu = 1173 \text{ cm}^{-1}$ according to reference [170, 172]. Stretching vibrational modes of the C-N-C imide component, bond (ii) in Figure 3.5, causes the absorption at $\nu = 1380 \text{ cm}^{-1}$, peak (A). Peak (B) at $\nu = 1500 \dots 1520 \text{ cm}^{-1}$ represents the benzene ring C=C stretching, bond (i). Peak (C) at $\nu \approx 1720 \text{ cm}^{-1}$ results from asymmetric stretching of the (imide-) carbonyl groups ($-\text{C}=\text{O}$), bond (iii), whereas the symmetric stretching of the (N)-C=O groups leads to the smaller absorption peak at $\nu \approx 1770 \text{ cm}^{-1}$, peak (D). The absorption peaks (A), C-N-C stretching, (C) and (D), asymmetric and symmetric stretching of $-\text{C}=\text{O}$, respectively, remain unchanged after the cell culture experiments.

The strongest increase in absorption is observed for $\nu = 1020 \dots 1250 \text{ cm}^{-1}$. In particular after the treatment with control medium (i.e., without living cells), the peak broadens and its magnitude at $\nu \approx 1110 \text{ cm}^{-1}$ increases simultaneously. The control medium features a relatively small absorption band around $\nu \approx 950 \dots 1100 \text{ cm}^{-1}$, see Figure 5.6 in chapter 5.3. Based on

the FTIR spectra alone, it is unclear if co.-me. residues cause the observed absorption increase and if such residues also explain the newly developed shoulder at $\nu = 1120 \dots 1220 \text{ cm}^{-1}$. The XPS analysis after prolonged water rinse of test samples, see section 6.3.2.3, and the analysis of impedance spectra after sterilization, see section 6.7, both point to a process where control medium penetrates into the PI surface region. Such a process also explains the increase of the FTIR absorption bands. Peak (B) increases slightly after cell culture treatment and the new peak at $\nu \approx 1600 \dots 1700 \text{ cm}^{-1}$ reminds of the absorption features already found with $\text{SiO}_x\text{:C/SiN}_y$ as well as with BCB samples in this spectral range, see chapters 6.1.2 and 6.2, respectively.

Figure 6.18 depicts the by now well known spectral range $\nu \approx 2800 \dots 3500 \text{ cm}^{-1}$. The absorption bands (E) and (F) appear also with $\text{SiO}_x\text{:C/SiN}_x$

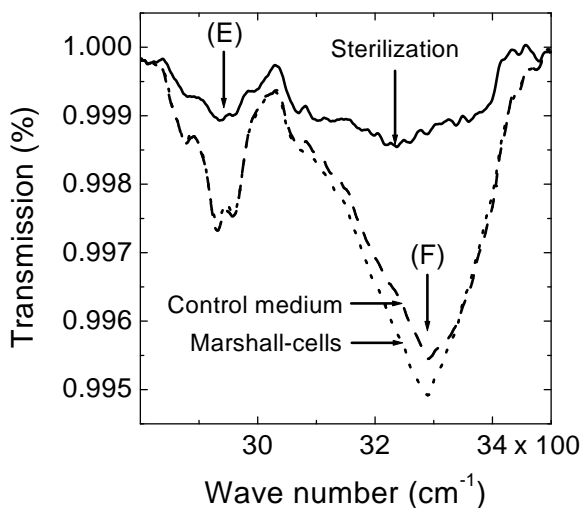


Figure 6.18: FTIR spectra of polyimide samples for $\nu = 2800 \dots 3500 \text{ cm}^{-1}$.

and BCB samples. Similar to the $\text{SiO}_x\text{:C/SiN}_x$ samples, the "as deposited" PI specimen seem to contain small amounts of N-H bonds, peak (F). For PI samples, the increase of this absorption band after cell culture tests is stronger than for the inorganic material and the BCB. See chapters 6.1.2 and 6.2 for a description of both peaks for the $\text{SiO}_x\text{:C/SiN}_y$ and the BCB material, respectively.

The transmission FTIR of polyimide samples shows that all imide- and carbonyl absorption bands which are typical for polyimide remain constant after cell culture treatment. **No degradation** of the material is observed by FTIR.

6.3.2 XPS analysis

Table 6.4 lists the XPS-analysed PI samples. In analogy to the $\text{SiO}_x\text{:C/SiN}_x$ - and BCB materials, the first paragraph focuses on the cell culture experiments. All samples used here, including one untreated sample and one "only sterilized" sample, are cut from the same wafer. In a second paragraph, a group of samples from a different wafer substrate are exposed to solutions of *glutamine* and *glucose* (and NaOH and HCl). The last section describes an experiment which analyses the rinsing efficiency of deionized water with regard to the removal of growing medium residues from the PI's surface.

Due to a temporarily broken-down Mg X-ray source, the measurements of the cell culture experiments are performed using an Al X-ray source, while the glutamine and glucose- solution tests are analysed with the Mg X-ray source. Though the attenuation length for photoelectrons depends on the excitation energy, see equation 5.17, the variations in the depth resolution between Mg- and Al- X-ray source are assumed to be of minor relevance. Both excitation energies should yield identical total element ($\int X$, $X=\text{C, O, N}$) concentrations as well as the same contributions of subpeaks to an element's spectrum.

6.3.2.1 Cell culture experiments

Figure 6.19 shows the binding energy spectrum of C 1s for PI samples before and after cell culture experiments. Figure 6.20 displays the XPS spectra for O 1s and N 1s in (a) and (b), respectively. Based on the fitting of the XPS peaks as described in chapter 5.4, the total element composition of the untreated PI is in almost perfect agreement with the structural formula of the BPDA/PPD polymer as presented in Figure 3.5: $\int \text{C } 1s = 74 \dots 75 \%$, $\int \text{O } 1s = 17 \%$ and $\int \text{N } 1s = 7 \%$. The following analysis follows literature data. Changes in the surface chemistry of polyimides are examined for many applications in the semiconductor industry. As all XPS studies begin with the analysis of the untreated material, there is a large collection of published XPS spectra, especially C 1s spectra, available. The following selection includes PMDA / ODA polyimides, see section 3.2.3. Apart from the ether linkage (C-O-C) in the PMDA / ODA, the binding chemistry of the carbon is practically identical, see references [247, chapter 5.1], [248, 162, 161, 249, 250, 251, 252, 253, 254, 164, 170, 160, 255, 176, 240, 193, 148, 256]. The deconvolution of the C 1s peak reveals two major subpeaks at $E_b = 284.6 \text{ eV}$ for C-C bonds and at $E_b = 288 \text{ eV}$ for C=O bonds and the much smaller subpeak at $E_g \approx 285.5 \text{ eV}$ for the C-N bonds. The shakeup transition $\pi - \pi^*$ which accompanies core level ionizations leads to a small observable satellite component at $E_g \approx 291 \text{ eV}$ (difficult to see in the presented spectral range).

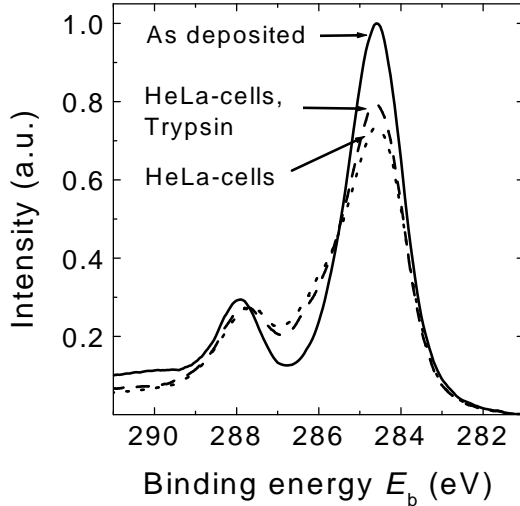


Figure 6.19: XPS spectra of Polyimide samples before and after HeLa-cell test experiments: C 1s.

The quantitative contribution of each subpeak to the total C 1s spectrum corresponds again very well to the structural formula. The oxygen peak of the untreated samples at $E_g \approx 530$ eV results from the carbonyl groups (C=O), see bond (iii) in Figure 3.5. The slight shoulder towards higher binding energy indicates the presence of C-O and / or ether groups (C-O-C) and / or O-N bonds which are no inherent parts in the BPDA/PPD backbone chemistry. Depending on the energy position and / or the full width at half maximum (FWHM), the C=O peak takes up $S_{C=O} \approx 80$ % of the total O 1s peak. A third much smaller peak at $E_g \approx 535$ eV is observed which can again be attributed to $\pi - \pi^*$ transitions. As predicted by the chemical formula, the C-N bonds form a single N 1s peak at $E_b = 399$ eV.

All samples that are exposed to the control medium exhibit a shift in the total element composition with regard to the carbon and nitrogen concentration as compared to the untreated sample: $c_C^{abs} \approx -4 \dots 5$ % and $c_N^{abs} \approx +4 \dots 5$ %. Within the group of six cell culture samples, the increase of N bonds is slightly lower for trypsinized samples. On average, the difference between non-trypsinized and trypsinized samples is of the order of $t_{C,N}^{abs} \approx 0.5$ % (which is the typical margin of error, hence the *trend* among the six samples is summarized). For all cell culture samples, the C 1s C-N subpeak increases in the C 1s spectrum, accompanied by a reduction of the C-C peak. However, matching the lower total N concentration after trypsinization (see above), the C-N increase is consistently lower for all three trypsinized

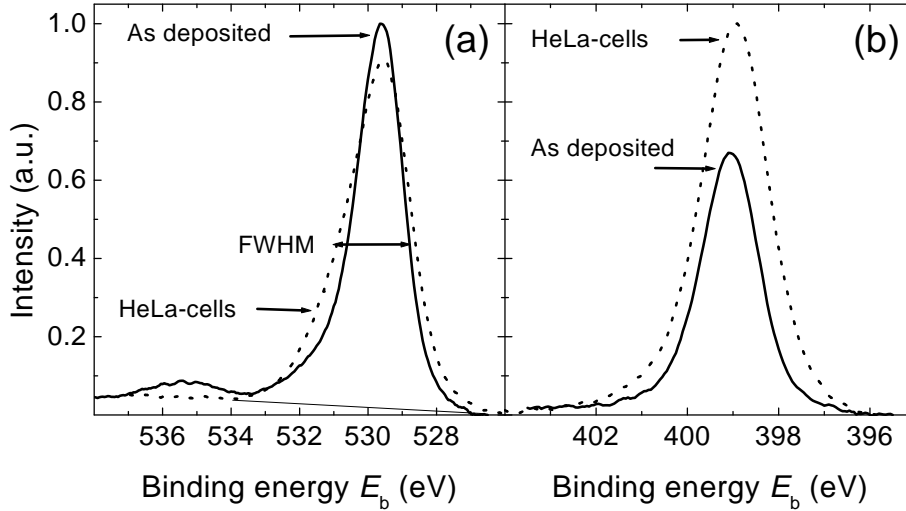


Figure 6.20: XPS spectra of Polyimid samples before and after HeLa-cell test experiments: (a) O 1s, (b) N 1s.

samples. The C 1s $\pi - \pi^*$ peak is no longer discernible. The total oxygen concentration remains unchanged. However, the FWHM of the main peak increases indicating a reduction in C=O groups and an increase in the above mentioned C-O / O-N / C-O-C bonds. The O 1s satellite peak of the $\pi - \pi^*$ transitions disappears. The variations between co.-me.-, or Marshall-cell-, or HeLa-cell- treated samples are smaller than the margin of error of the XPS measurements.

6.3.2.2 Exposure to glutamine and glucose

The control medium contains a large number of enzymes and vitamins in addition to its anorganic components, see Appendix 7.1. In an attempt to seek out the effect of individual components of the growing medium, a series of much simplified solutions is applied to the samples for $t \approx 24$ h. The chemical solutions include (A) 0.01 M glutamine, (B) 0.025 M glucose, (C) glutamine + glucose, (D) HCl (0.01M) + glutamine, (E) NaOH (0.01 M) + glutamine, (F) HCl + glucose, (G) NaOH + glucose. The solutions including the samples are kept in ambient atmosphere under low light conditions during the experiment. After taking the samples out of the solution, they are rinsed in deionized water for $t_{rinse} \approx 1.5$ min, dried with clean nitrogen and mounted into the XPS chamber in the same XPS series, including one additional untreated sample (series (5), see table 6.4). As mentioned in this chapter's

introduction, the Mg-X-ray source is used throughout this XPS run. Neither the C 1s spectra, nor the O 1s-, nor the N 1s spectra reveal any significant alterations in the polyimide's surface chemistry after exposure to solutions (A) to (G). Hence, no spectra are presented. The total element's contributions to the spectra remain constant as well as the share of the subpeaks which constitute the element's peaks. All samples almost exactly reproduce the elemental composition of the "no treatment" and "sterilization" samples of XPS run (1). With the exception of solution (E) where \int C 1s is roughly one absolute percentage point (app) higher and \int O 1s roughly one app lower than average, not even a trend among the treatment groups is observable.

6.3.2.3 Water rinse versus surface contamination through control medium residues

As described in chapter 5.4, the XPS method is highly sensitive to changes in the surface chemistry of a sample. The fraction of electrons that are emitted at a certain depth and reach the surface of the material unscattered depends on the kinetic energy of the electrons (i.e., on the chemical element) and on the composition of the material. As depicted in Figure 6.9, that fraction decreases exponentially with increasing emission depth. Thus, the "maximum" depth of origin of the unscattered detected electrons is of the order of $d_{surf} \approx 1 \dots 4$ nm, see table 5.1 and small chemical variations at the sample's surface can be detected. By the same token, any contamination of the surface to be examined will show up in the XPS spectrum. In the analysis of the XPS spectra one must therefore try to estimate and exclude the effects of surface contamination.

To this end, a series of XPS experiments with polyimide samples from one wafer that are exposed to the control medium followed by a rinse in clean water is devised. Table 6.5 summarizes the treatment procedures of all samples. All samples are hot-oven sterilized as described in chapter 4.1.1. Samples (e), (f) and (g) are exposed to control medium for $t_{co.-me.} = 10$ s at $T_{co.-me.} \approx 20^\circ\text{C}$, followed by a $t_{rinse} = 2$ s, 1 min and 10 min rinse in deionized water, respectively. The three samples are then stored in PbS in ambient atmosphere at $T_{PbS} \approx 20^\circ\text{C}$. Finally, the samples undergo a second rinse step in deionized water for $t_{rinse} = 2$ s, 30 s and 1 min, respectively, before they are dried with clean nitrogen gas and mounted in the XPS chamber. Similarly, the samples (i) and (j) are exposed to control medium in an incubator for 1 day, followed by a water rinse for 2 s and 1 min, respectively, a storage in PbS for 15 min, a second water rinse for 2 s and 30 s, respectively, and the drying with a nitrogen pistol. Sample (d) serves as the reference sample which is only sterilized. Samples (h) and (k) are kept in PbS for 1 d and

Table 6.5: *Rinse of PI samples after exposure to control medium*

Wafer / Sample	treatment exp. to co.-me.	rinse	exp. to PbS	rinse
01 / d	–	–	–	–
01 / e	10 s	2 s	24 h	2s
01 / f	10 s	1 min	24 h	30 s
01 / g	10 s	10 min	24 h	1 min
01 / h	–	–	24 h	1 min
01 / i	1 d	2 s	15 min	2 s
01 / j	1 d	1 min	15 min	30 s
01/ k	–	–	10 min	30 s

10 min, respectively, rinsed in water for 1 min and 30 s, respectively, and dried in nitrogen (neither sample are shown in the plot). All samples are mounted into the XPS chamber in one run (run (6)), see table 6.4 in order to maximise the comparability of the recorded spectra.

Figure 6.21 shows the XPS spectra of samples (d) ... (j). The mathematical fitting procedure reveals the following results: The chemical composition of the reference sample (d) is in agreement with the theoretical structural formula, see chapter 3.2.3. After $t = 10$ s and $t = 1$ d exposure to the control medium, the \int C 1s decreases by about $c_{C,10s}^{abs} = -2$ and $c_{C,1d}^{abs} = -4$ pp, respectively. Within a range of $c_C^{abs} = 0.5 \dots 1$ pp, a trend towards a lower carbon concentration for longer water-rinse periods is observed. The contribution of the C-N subpeak to the total C 1s peak, \mathbf{S} (C-N), increases after $t = 10$ s exposure to the control medium from \mathbf{S} (C-N) = 5 ... 10 % to \mathbf{S} (C-N) = 15 % and after $t = 1$ d exposure to control medium up to \mathbf{S} (C-N) 28 ... 33 %. Here, the effect of prolonged water-rinsing is almost negligible. The longer the exposure to the control medium, the lower the XPS signal of the $\pi-\pi^*$ transition at $E_b \approx 290 \dots 291$ eV.

The analysis of the N 1s peak (not shown in diagram) reveals an increase of the total N concentration from \int N 1s = 6.4 % (sample (d)) to \int N 1s = 9.2 ... 9.9 % for samples (e), (f), (g), reaching \int N 1s = 10.7 ... 11.4 % for the samples (i) and (j) which are exposed to the control medium for 1 day. Among the samples (e), (f) and (g), there is a trend towards higher \int N 1s for longer water-rinsing, \int N 1s (e) = 9.2 %, \int N 1s (f) = 9.7 %, \int N 1s (g) = 9.9 %, with a simultaneous decrease of the \int C 1s concentration. The nitrogen concentration of the two PbS samples (h) and (k) is $c_N^{abs}(h) \approx 0.5$ pp and $c_N^{abs}(k) \approx 1$ pp higher than \int N 1s (d) of the untreated

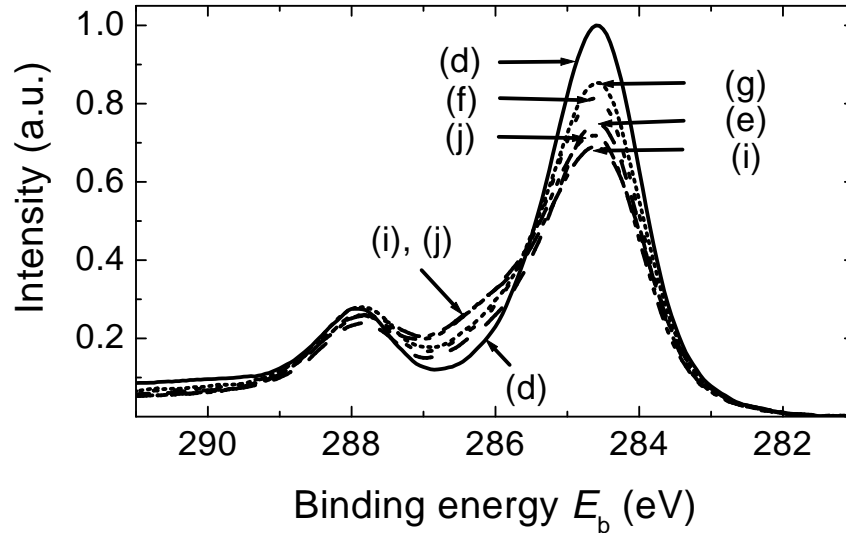


Figure 6.21: XPS spectra (C 1s) of polyimide samples before and after short-time exposure to control medium. All samples except (d) were rinsed in clean water for various amounts of time after the control medium experiment, see table 6.5.

sample.

The variations in the O 1s spectrum are marginal. However, the subpeak at $E_b \approx 535$ eV diminishes for the samples (e), (f), and (g) and does not exist in the spectra of the samples (i) and (j).

Summary of XPS analysis after water rinse experiments

With increasing exposure-time to the control medium, $\int C 1s$ decreases and $\int N 1s$ increases, matching the observations in the previously described cell-culture experiments, see chapter 6.3.2.1. Particularly after $t = 10$ s co.-me. treatment, a prolonged water-rinse slightly reduces the changes in the C 1s spectrum. The effect of the water-rinse is less pronounced after $t = 1$ d exposure to the co.-me. The $\int C 1s (t_{co.-me.})$ and $\int N 1s (t_{co.-me.})$ changes are always greater than the variations due to water-rinsing.

The observations cannot be explained by co.-me. residues at the polyimide surface alone. Rather, with increasing time of co.-me. exposure, either the BPDA/PPD structure is chemically altered and / or the co.-me. penetrates deeper into the PI's surface. With the XPS data alone, both processes cannot be distinguished.

6.3.3 Summary of biostability analysis with FTIR and XPS

The transmission FTIR spectra reveal no changes in the PI specific absorption bands after cell culture treatment, see section 6.3.1. Hence, the PI remains chemically stable under co.-me.- and cell culture conditions. Moreover, the analysis of the impedance spectra in chapter 6.3.4.3 points to a diffusion process of electrolyte components into the hot-oven dried polymer. Both results support the explanation that co.-me. infiltrates the PI surface. Thus the observed XPS changes after co.-me. exposure result from a smooth interface region (which deepens with increasing $t_{co.-me.}$) where co.-me. components remain after the water rinse and contribute to the XPS signal. The PI's surface region is in effect diluted and small signals such as the $\pi-\pi^*$ transition at $E_b \approx 290 \dots 291$ eV or the oxygen subpeak at $E_b \approx 535$ eV diminish. In chapter 6.3.4.3 a physical model for the polyimide is presented which takes into account all experimental results.

6.3.4 Impedance spectroscopy

The analysis of impedance spectra of polyimide divides into two sections. In the first section, spectra of three polyimide series, each of a different layer thickness, are recorded with the aim of identifying the RC-element which corresponds to the polyimide (-bulk). Moreover, three contacting methods are employed and their respective merits are discussed. The second section presents two main experiments, namely, (A) the hot-oven-sterilization of the polyimide and (B) the growth of living cells on the samples. No spectra characteristics can be linked with cell-culture treatments. However, following the sterilization of the $d_{PI-1,2} \approx 50$ nm polyimide samples, gradual changes of the impedance spectra over the time of exposure to the electrolyte (i.e., the time after the assembly of the electrochemical cell) are observed. Based on a physical model for the polyimide, the equivalent circuit of Figure 5.2 is modified to take into account the time-dependent diffusion of electrolyte components into the surface region of the material.

6.3.4.1 Untreated polyimide

Table 6.6 lists the polyimide series and their thicknesses and theoretical values for the polyimide's capacitance $C_{(PI),th}$ and volume resistance $R_{(PI),th}$. Furthermore, the three contacting methods utilized in the measurement setups are given and the polyimide's volume capacitance and shunt resistance as determined from fits of the corresponding impedance spectra are presented.

The general equation for a plane capacitor, equation 5.1, gives the theoretical capacitances for the three polyimide layers. $\epsilon_r = 2.9$ is taken from the technical data of the manufacturer [84] and Ponchak [257]. Surface profiling using a Dektak profilometer yields the thickness of the PI-2 and PI-3 series with a margin of error of below 5%. The thickness of the thin PI-1

Table 6.6: Evaluation of four polyimide series with impedance spectroscopy

		polyimide series		
		PI-1, PI-2	PI-3	PI-4
PI-thickness	$d_{PI-1,2,3,4}$	50 nm	1.2 μm	4.6 μm
	$C_{(PI),th}$ (F)	5.1×10^{-8}	2.1×10^{-9}	6.3×10^{-10}
	$R_{(PI),th}$ (Ω)	5×10^{10}	1.2×10^{12}	4.6×10^{12}
contact	$C_{(PI),ev.}$ (F)	$1.2...5 \times 10^{-7}$	$2...3.5 \times 10^{-9}$	$\approx 7.9 \times 10^{-10}$
evaporation	$R_{(PI),ev.}$ (Ω)	$300...7 \times 10^8$	$\geq 2.5 \times 10^8$	$\approx 10^{10}$
electrolyte	$C_{(PI),el.}$ (F)	$1.5...2 \times 10^{-7}$	$2...2.5 \times 10^{-9}$	$8...8.4 \times 10^{-10}$
cell	$R_{(PI),el.}$ (Ω)	$\geq 10^8$	$\geq 10^5$	$\geq 10^{10}$
gold leaf ²	$C_{P(I),g.l.}$ (F)	$10^{-8}...10^{-9}$	–	–
	$R_{(PI),g.l.}$ (Ω)	$2 \times 10^5...10^{10}$	–	–

layers is obtained from cross-section SEM pictures, see chapter 3.2.5, and Dektak measurements with a margin of error of approximately $\pm 30\%$. The theoretical volume resistance is again taken from the manufacturers' data [84].

The capacitance and volume resistance of the polyimide of each thickness-series for the three contacting methods are calculated in numerical fits of the experimental data to (A) a Randels equivalent circuit, see chapter 5.2.2, for the "dry" contacting methods and (B) to the equivalent circuit of Figure 5.2 for the electrolyte cell measurements. Data (B) may also be fitted with the simple Randels circuit. Figure 6.22 shows the Bode plots of admittance spectra of PI-1 polyimide samples. The spectra (a) and (b) are examples from a series of recorded spectra of the same sample with repeated micro-needle contacting. No gradual spectra variations are observed but rather a sudden shift occurs in the phase angle spectrum. $|Z|(f)$ of curve (B) reaches a maximum towards lower frequencies which is orders of magnitude lower than that of curve $|Z|(f)$ (a). For $\omega \rightarrow 0$, $|Z|$ approaches a maximum of $R_{sh} + R_s$, see equations 5.8 and 5.10. A numerical fit of the data (b) with the Randels equivalent circuit reveals a shunt resistance R_{sh} ($\cong Z_{DE}$) $\approx 25.000 \Omega$ and $R_{sh} \approx 2 \times 10^9 \Omega$ for data (A), while the capacitance C_{DE} remains almost constant at $C_{DE} \approx 1.27 \times 10^{-7}$ F for (A) and (B). Both spectra highlight the danger of partial punctuation of the thin PI-1 layer that goes with the contacting of the evaporated Cr-Au electrode and leads to a reduced reproducibility of the PI's shunt resistance levels off at several dozen ohms which is the overall series resistance of the experimental setup. Spectrum (c) is an

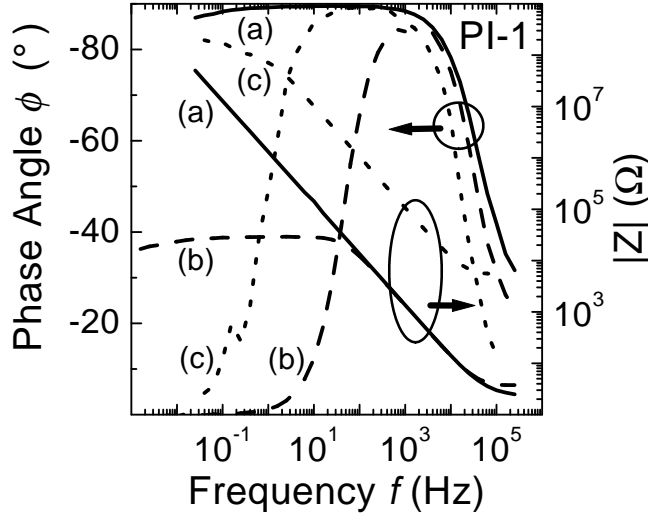


Figure 6.22: Bode plots of admittance spectra of PI-1 polyimide samples. The arrows indicate the axis for the phase angle- and $|Z|$ -plots, respectively. (a) and (b) represent the spectra of one sample with an evaporated "front" contact. (c) shows an example of varying spectra obtained using the gold leaf contacting method.

example of varying spectra which are obtained with the gold leaf contacting of the polyimide layer. The capacitance is by a factor of 30 ... 100 lower than the theoretical value. As described in chapter 5.2.1.2, the gold leaf contacting gives a capacitor arrangement where "wrinkles" in the gold leaf result in large parts of the "capacitor" planes being separated by more than the thickness of the polyimide layer. Consequently, the effective surface area of the device is smaller and difficult to reproduce. The course of $|Z|(f)$ for this specific measurement indicates a shunt resistance of $R_{sh} \geq 10^8 \Omega$ (see $f \leq 10^{-1}$ Hz) and a series resistance R_s of the order of several thousand ohms. The variations in the shunt resistance (not shown in the plot) can again be accounted for by "dents" in the gold-contact inflicted by the micro-needles.

Figures 6.23 and 6.24 depict the analogous Bode plots of the PI-3 and PI-4 series, respectively. The spectra (A) are recorded with evaporated Cr-Au contacts, the spectra (B) using electrolyte cells, as depicted in Figure 5.1. While all four spectra can be interpreted and hence evaluated in terms of a simple Randels equivalent circuit, the fit accuracy is best for the PI-4 samples ($d_{PI-4} = 4.1 \mu\text{m}$) with evaporated Cr-Au contacts. The overall series resistance of the experimental setups varies between 10 ... 50 Ω which is the minimum value for $|Z|(f)$.

The volume resistance of the polyimide films increases with increasing film thickness. The thin PI-1 & 2 films exhibit a theoretical resistance of $R_{PI-1,2,th} \approx 5 \times 10^{10} \Omega$ which is already at the measurement limit of the

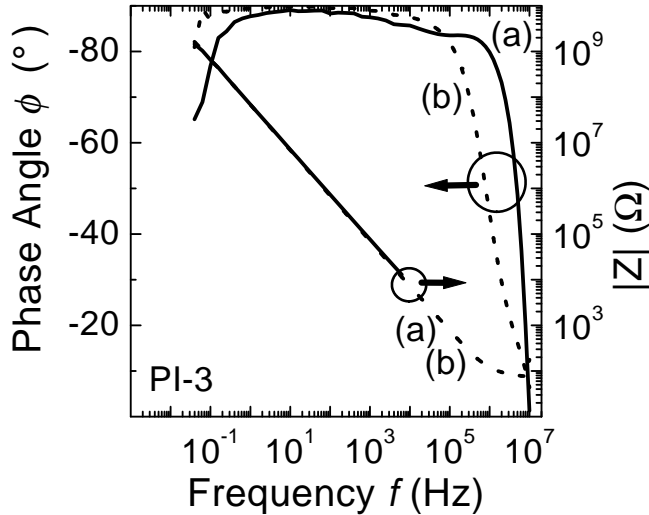


Figure 6.23: Bode plots of admittance spectra of PI-3 polyimide samples. The arrows indicate the axis for the phase angle- and $|Z|$ -plots, respectively. Sample (a) features an evaporated gold contact. Sample (b) is recorded in the electrolyte cell.

EG & G signal response analyser³. The experimentally obtained volume resistance data above $|Z| \approx 10^9 \Omega$ should therefore be treated carefully and rather considered as lowest estimates. Resistance data below that range indicate pin-holes and other structural defects in the polyimide films.

6.3.4.2 Ultra-thin polyimide under electrolyte and cell-culture conditions

Table 6.7 lists the sterilization and cell-culture experiments ("treatments") performed with polyimide samples. Whereas the sterilization experiments include again the four polyimide layers of varying thickness, the cell test experiments use only the thin polyimide of series PI-1 & 2. That is because any electronically distinct, presumably thin, polyimide-electrolyte interface

³The amplitude of the applied *sine* voltage signal is $U = 10 \text{ mV}$. With $|Z|$ of the order of 10^{10} , the measurement range of the response analyser is stretched to $I \approx 10^{-13} \text{ A}$!

³Time elapsed between the assembly of the electrochemical cell and the impedance measurement.

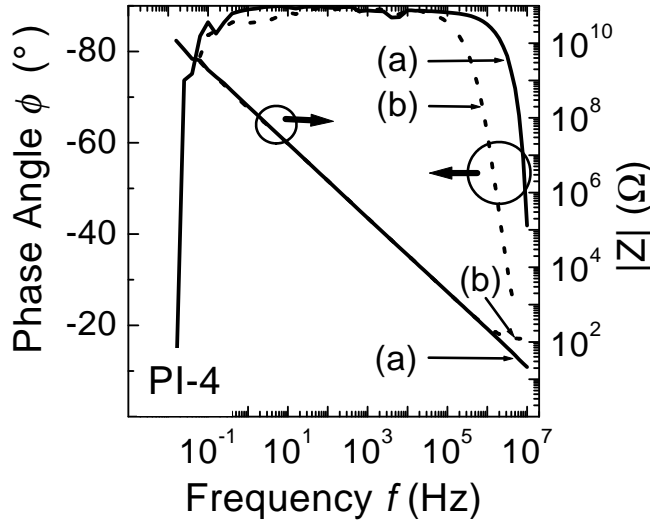


Figure 6.24: Bode plots of admittance spectra of PI-4 polyimide samples. The arrows indicate the axis for the phase angle- and $|Z|$ -plots, respectively. Sample (a) features an evaporated gold contact. Sample (b) is recorded in the electrolyte cell.

layer which might evolve during the growth of living cells would result in a high capacitance (and unknown shunt resistance) which is series connected with the polyimide's volume RC-element. Such a high capacitance is best discernible in impedance spectra, if the volume RC-element is only roughly one order of magnitude smaller.

For all experiments, the electrochemical cell serves as the sole measurement setup. That way, after the PI samples are taken out of the cell-culture medium, interference and possible alteration of the polymer's surface is kept to a minimum. Moreover, the recording of the electrolyte diffusion following the sterilization of the polyimide samples, requires that the samples not be exposed to vacuum as would be necessary in the alternative contact evaporation process.

Each treatment is carried out with a group of at least two samples. Samples that are prepared using (nominally) identical parameters do exhibit a variation of their impedance characteristics. As the chance of pinholes and other morphological inhomogeneities increases with decreasing thickness of the layer, special care must be taken particularly in the choice of the thin PI-1, -2 samples. Thus, samples featuring optically visible "dots", "rings", etc. in the layer as a result of imperfections in the spin-coating and curing process of the polyimide are excluded whenever possible, i.e., when there are spare samples from the same wafer available. Furthermore, samples cut from one single wafer are used when the impedance spectra after different exper-

Table 6.7: Overview of sterilization- and cell-culture experiments with polyimide samples.

Sample	Series	Treatment	PbS :H ₂ O	Impedance spectra, after
P 703 u	PI-4	sterilisation	1:0	3 min, 1-5 d
P 701 xx	PI-3	sterilisation	1:0	5 min, 1-5 d
P 02 c	PI-1	sterilisation	1:0	1 h, 2h, 7 h, 24 h
P 04 t	PI-2	sterilisation	1:0	1 min, 30 min, 1 h, ... 5 d
P 04 r	PI-2	sterilisation	1:10	12 min, 30 min, 1h, ... 5 d
P 04 y	PI-2	sterilisation	1:100	18 min, 40 min, 1h, ... 5 d
P 01 b	PI-1	as deposited	1:0	2h, 17h, ... 5 d
P 02 h	PI-1	Co.-Me.	1:0	1h, 8 h, 24 h, ... 5 d
P 02 l	PI-1	Marshall-c.	1:0	≈ 1 h, 1d, ... 5 d
P 02 p	PI-1	HeLa-c.	1:0	≈ 1 h, 1d, ... 5 d

iments are to be compared. In the context of the sterilization experiments, the distinctions in the diffusion element which are apparent among "equal" samples from different wafers will be addressed.

Figure 6.25 (a) and (b) compares the Bode plots of PI-1 samples (all cut from one wafer) after the samples' sterilisation and after cell-culture experiments, respectively. Figure 6.25 (a) demonstrates the changes of the electrochemical behavior of one sterilized sample over time of exposure to the electrolyte in the measurement setup. Approximately one hour after the assembly of the electrochemical cell, two minima of the phase angle ϕ over frequency f appear and the phase angle changes slowly over a wide frequency range $f = 10 \dots 10^4$ Hz. Seven hours later, the phase angle minimum at $f \approx 1 \dots 10$ Hz disappears but the slope of ϕ over f remains almost unchanged. After one day, the remaining minimum of the phase angle has slightly shifted to $f = 10^3$ Hz and ϕ decreases rapidly towards lower frequencies. The ϕ spectrum is now almost identical to that of the virgin polyimide sample (i.e., "As deposited"), shown in Figure 6.25 (b).

The analysis of the impedance spectra of samples that were subjected to living cells or the control medium reveals larger variations among the samples of one treatment group than are encountered among untreated or sterilized samples. However, the main characteristics of the "as deposited" samples hold also for the specimen which are exposed to either the control medium or living cells. No reproducible spectra variations can be attributed to either one of the cell test treatment groups.

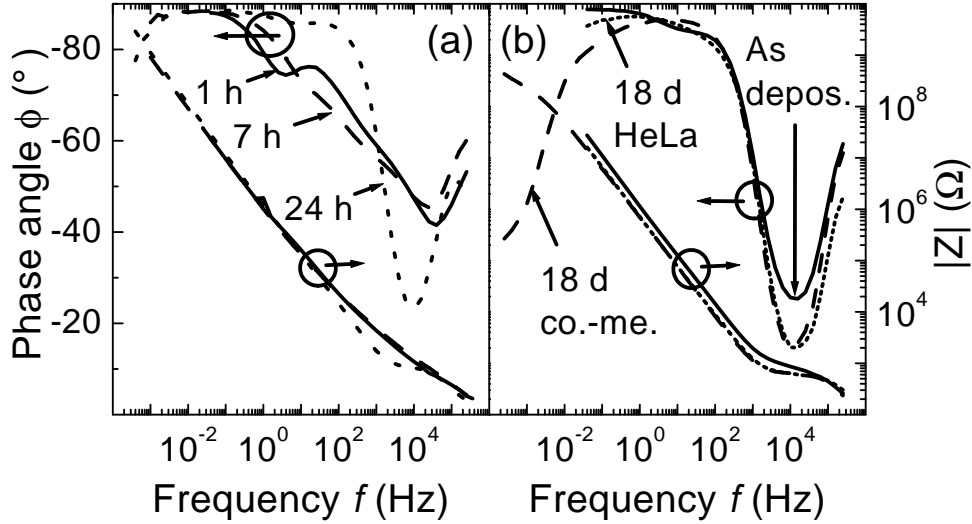


Figure 6.25: Impedance spectra of Polyimide samples. Bode plot of (a) one sample after hot-oven sterilization at $T_{h.o.} = 105^\circ$ for 12 hours. The time of the start of the measurement after the assembly of the electrochemical cell is given. (b) Several samples, each representing a group of samples exposed to a certain treatment within the cell test experiment. The arrows indicate the outer left- and outer right- ordinate-axis for the phase angle ϕ and $|Z|$, respectively, for both (a) and (b).

Figures 6.26 and 6.27 show the results of further sterilization experiments aimed at a better understanding of the time-behavior of the impedance spectra in Figure 6.25. Polyimide specimen from a second wafer, PI-2 (with nominally identical deposition parameters as the PI-1 series), are kept at $T_{h.o.} = 105^\circ\text{C}$ in a dry oven for approximately 12–18 hours and subsequently set up in the electrolyte cell with three concentrations of the electrolyte solution. Starting with the original concentration of physiological solution, $c_{Na^+} \approx 10^{23} \text{ l}^{-1}$, see Appendix 7.1, Figure 6.26, the ion concentration was reduced by a factor of 10, no plot shown, and by a factor of 100 in Figure 6.27 using deionized water.

The phase angle v frequency plot in Figure 6.26 shows a local minimum of $\phi \approx -55^\circ$ immediately after the assembly of the electrolyte cell. Initially, that minimum diminishes while shifting towards lower frequencies. After $t \approx 3 \text{ h}$, the minimum reappears at $f \approx 1 \dots 3 \times 10^{-2} \text{ Hz}$ and sharpens until it reaches a final status after approximately 10 hours. Simultaneously,

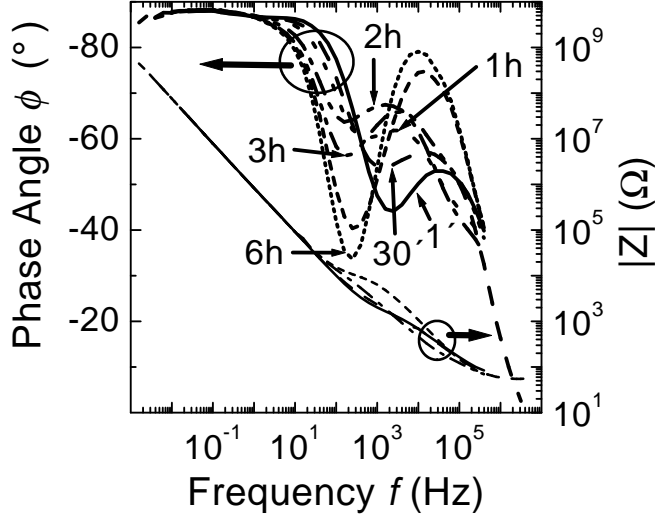


Figure 6.26: Bode plots of impedance spectra of PI-2 polyimide samples. Electrolyte cell setup with the original PbS solution with an ion concentration of $c_{Na^+} \approx 10^{23} \text{ l}^{-1}$.

a local maximum at $f \approx 5 \times 10^3 \text{ Hz}$ develops with the phase angle reaching $\phi \approx -80^\circ$. At frequencies below $f \approx 10^{-2} \text{ Hz}$ and above $f \approx 5 \times 10^5 \text{ Hz}$, the impedance spectrum remains unchanged over time.

The spectra in Figure 6.27, PbS : H₂O = 1 : 100, show the phase angle ϕ initially decreasing monotonically from almost $\phi = -90^\circ$ at $f = 10^{-1} \text{ Hz}$ to $\phi \approx -20^\circ$ at $f \approx 3 \times 10^5 \text{ Hz}$. At $f \approx 10^2 \text{ Hz}$, a point of inflection is observed which forms into a local minimum after $t \approx 3 - 6 \text{ h}$. The final status is reached after $t \approx 12 \dots 24 \text{ h}$. It appears that the final impedance spectrum is reached earlier for samples using the original PbS. However, the limited number of tested samples does not allow for a clear interpretation and further experiments are needed.

Figure 6.28 (a) and (b) displays the fitted curves and the corresponding measurement data for sample P04t – original PbS – and sample P04y – PbS : H₂O = 1 : 100, respectively. The time between the assembly of the electrochemical cell and the start of the measurement is given and the arrows point to the the outer left- and outer right- ordinate-axis for the phase angle ϕ and $|Z|$, respectively, for both (a) and (b). The fit and the recorded data are hardly distinguishable. The fitting routine is applied to the equivalent circuit of Figure 5.2, modified by an additional *Warburg impedance* term. All RC elements in Figure 5.2 can be ascribed to the dielectric and to the electrolyte cell setup and are verified for the PI as well as the SiO_x:C/SiN_x samples. Hence, the expansion of the equivalent circuit by a Warburg impedance in

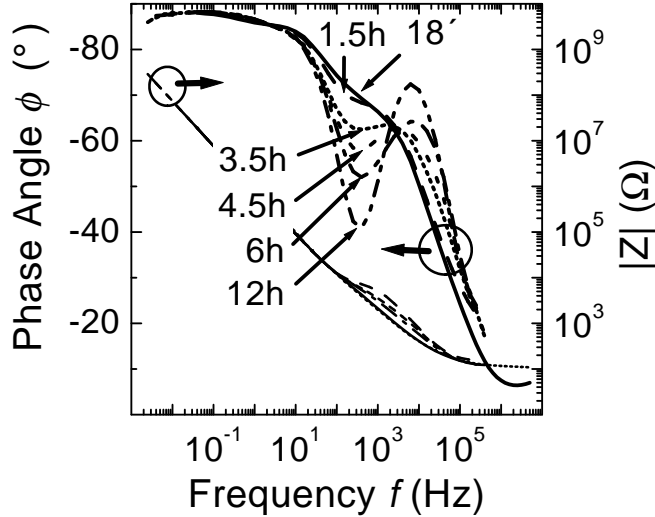


Figure 6.27: Bode plots of impedance spectra of PI-2 polyimide samples. Electrolyte cell setup with a $PbS : H_2O = 1 : 100$ diluted solution with an ion concentration of $c_{Na^+} \approx 10^{21} t^{-1}$.

order to be able to explain the time-dependent impedance spectra is justified. The following section describes a physical model which takes into account diffusion-like processes in the polyimide's surface region. Based on that model, the circuit including the Warburg impedance is developed and the fitting parameters are given.

6.3.4.3 Physical model and equivalent circuit

The analysis of all impedance spectra reveals distinct capacitive elements in the experimental setup. With the aim of interpreting and understanding the experimental data, Figure 6.29 depicts a physical model of the polyimide sample in an electrolyte cell setup. Region (1) represents the the polymer's bulk which in this model is not affected by cell culture experiments and remains unchanged over time of exposure to the electrolyte in the experimental setup after the sterilisation of the sample. As seen in SEM cross section views of the material, see chapter 3.2.5, the volume does exhibit a columnar-like structure. The surface of the polymer is indicated by the grey shaded area (2). See chapter 3.2.5 for a description of its morphology. Cracks, fissures, etc. reach a certain depth and the region is less homogeneous than the bulk. The transient changes in the impedance spectra over time following the sterilisation of the material are thought to origin in this thin surface layer. The electrolyte which mainly consists of H_2O and Na^+ and Cl^- ions, see Appendix 7.1, "contacts" the polymer. The arrows (3) indicate components of

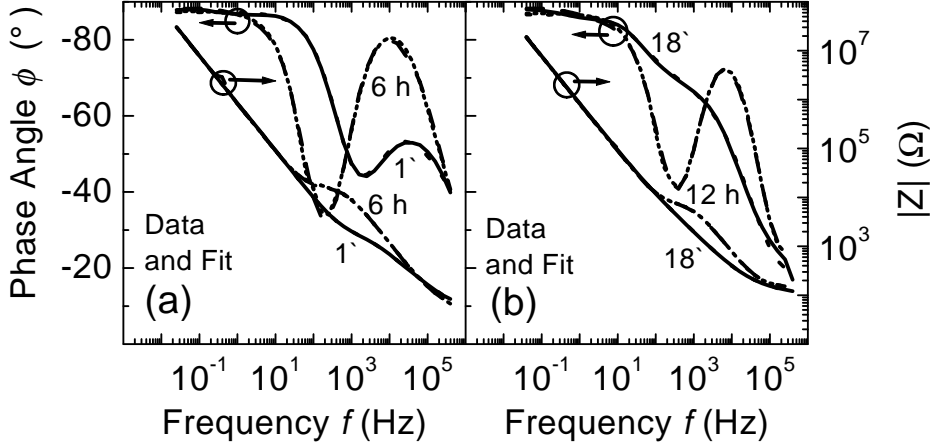


Figure 6.28: Bode plot of impedance spectra (a) Recorded data of sample P04t – using original PbS – and numerical fit. (b) Recorded data of sample P04y – using a PbS:H₂O = 1:100 solution – and numerical fit. The time after the assembly of the electrochemical cell is given. The arrows indicate the outer left- and outer right- ordinate-axis for the phase angle ϕ and $|Z|$, respectively, for both (a) and (b).

the electrolyte entering the material after the drying process in the hot-oven sterilisation. At the Cr-contact – electrolyte interface, a Helmholtz layer forms with a "spacing" between the electrolyte's ions (the inner Helmholtz plane) and the solid state of $d_{HH} \approx 1$ nm. The Cr sheet and the silicon wafer - polyimide interface are separated by $d_{Cr-W} \approx 200$ μ m.

Based on the physical model, the equivalent circuit of Figure 5.2 is modified to explain the impedance spectra of the thin polyimide after sterilization. In order to accommodate the postulated distinct surface region of the polyimide, the new circuit in Figure 6.30 (a) ... (d) contains a *Warburg impedance* Z_W which takes into account diffusion-like processes at the material's surface. $R_g C_g$ in (a) again represents the geometric capacitance of the electrolyte cell setup. (b) depicts the Helmholtz layer capacitance $R_{HH} C_{HH}$. The polyimide's bulk capacitance $R_{de} C_{DE}$ -element in (c) is series connected to the Warburg impedance and a shunt resistance $R_{(sh),w}$ in (d). As shown in the analysis of the electrolyte cell without a dielectric, see section 5.2.4, only a lower limit for the shunt resistance R_g can be calculated, $R_g \geq 10^6$ Ω (dotted line symbol). Similarly, a lowest limit for R_{de} is found, $R_{de} \geq 5 \times 10^6$ Ω

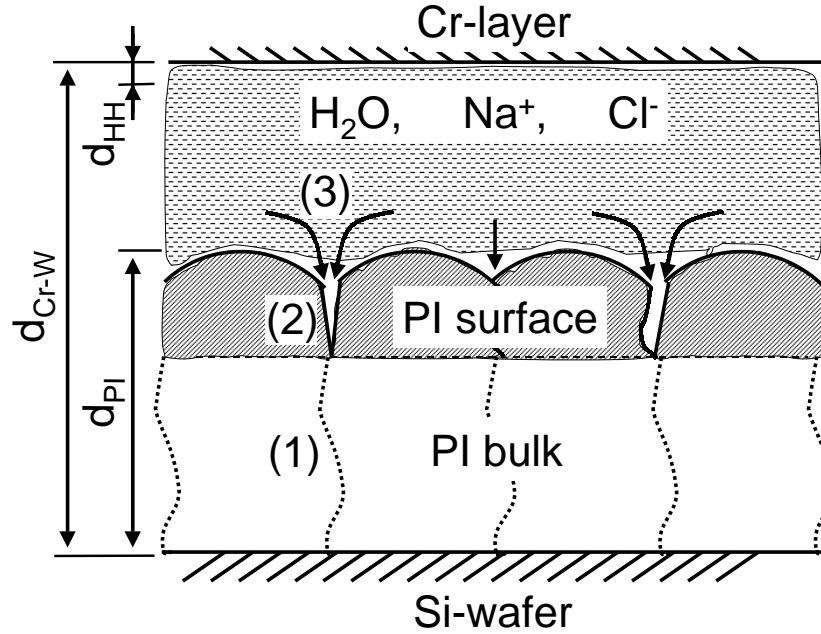


Figure 6.29: Cross section sketch of polyimide samples in the electrolyte cell setup. (d_{Cr-W}) Separation between the wafer substrate and the Cr-electrode. ($d_{PI-1,2}$) Total thickness of the PI. (d_{HH}) Distance between the inner Helmholtz plane and the solid (indicated exemplarily for both Helmholtz layers). (1) "Grains" in the columnar structure of the bulk material. (2) cracks, symbolising the surface roughness. (3) Entry path for electrolyte components into the surface layer.

(dotted line symbol). The gold contact- and electrolyte cell measurements described at the beginning of the chapter show R_{de} to be of the order of $R_{de} \approx 10^{10} \Omega$. The large Helmholtz capacitance $C_{HH}R_{HH}$ may be left out in the fitting routine without significantly reducing the accuracy of the fit (dotted line symbol). The polyimide's volume capacitance is represented by C_{DE} . Except for the gold leaf contacting, all experimentally obtained capacitance values of the polyimide are several percent higher than the corresponding theoretical data, see table 6.6 at the beginning of the chapter. This deviation from theory decreases with increasing thickness of the dielectric. The data obtained from the contact evaporation- and the electrolyte cell measurements are in good agreement (though fit-data from the electrolyte cell setup exhibit a tendency towards higher capacitances). Variation of the capacitance data within one experimental setup results from a typical margin of error of 20% for the contacted (geometric) surface area. The generally higher "experimental capacitance" as compared to the theory

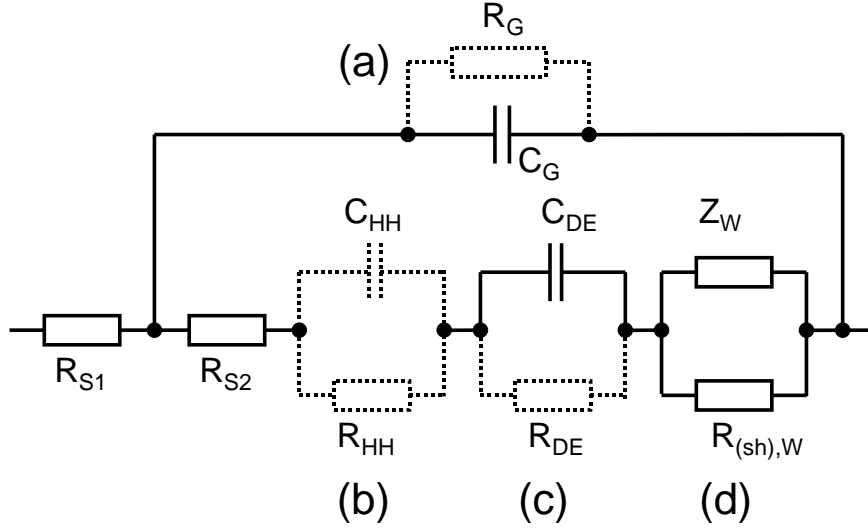


Figure 6.30: Equivalent circuit for polyimide samples in the electrochemical cell. (a) Geometric capacitance of the setup. (b) Helmholtz layer. (c) PI bulk. (d) PI surface region, where the Warburg impedance represents diffusion-like processes of electrolyte components. The dotted elements may be left out in the fitting routine, see text.

is explained by the surface roughness of the polyimide, see chapter 3.2.5, which leads to fluctuations in the separation of the capacitor plates (silicon wafer and electrolyte-PI interface). In principle, the resulting *rough surface capacitance* $C_{(PI),r.s.}$ can be estimated according to

$$C_{(PI),r.s.} \sim \frac{A_1}{\bar{d}_{PI} + \Delta d_{PI}} + \frac{A_1}{\bar{d}_{PI} - \Delta d_{PI}} + \frac{A_2}{\bar{d}_{PI}}, \quad (6.3)$$

where \bar{x} denotes the mean separation between the wafer surface ("back contact") and the electrolyte-PI interface, Δx represents the (average) deviation from \bar{x} and A_1 is the surface area of the polyimide which is closer or further apart from the wafer than the surface A_2 which corresponds to the mean thickness of the polymer. An increase in the average deviation Δx from the mean thickness of the polymer, i.e. a less smooth surface of the polymer, increases the second term of the equation, thus raising the total capacitance of the polyimide layer.

The process of electrolyte components entering the surface polyimide layer – area (2) in Figure 6.29 – for sterilized samples is thought to be governed

by diffusion, which is described by Fick's laws of diffusion,

$$\frac{\partial c(x_d, t)}{\partial t} = D_d \frac{\partial^2 c(x_d, t)}{\partial x_d^2}, \quad (6.4)$$

with the concentration c of the diffusing species and the coordinate x_d along the diffusion path and the diffusion coefficient D_d . This differential equation is analogous to the wave equation which describes the propagation of electromagnetic waves in RC-lines, see references [258, chapter 2.1], [216, chapter 2] and Appendix 7.2. For the "open circuit" boundary condition, the impedance \underline{Z} follows equation

$$\underline{Z}_W = \frac{R_w \tanh(iK\omega)^p}{(iK\omega)^p}, \quad (6.5)$$

which is for $p = 0.5$ the Warburg impedance \underline{Z}_w in the context of the diffusion process in the equivalent circuit ((D) in Figure 6.30). The parameter K , see appendix 7.2, is given by

$$K = \frac{l_d^2}{D_d}, \quad (6.6)$$

with the diffusion thickness l_d and the effective diffusion coefficient D_d . For the parameter R_w holds

$$R_w \propto \frac{l_d}{D_d}. \quad (6.7)$$

The fitted curves presented in Figure 6.28 (A) and (B) for the samples P04t and P 04y, respectively, are obtained with a Warburg parameter $p = 0.55 \dots 0.65$ for the first measurements after $t_{04t} = 6$ min and $t_{04y} = 18$ min. Other samples may be fitted with $p = 0.5$. The last measurements after $t_{04t} = 6$ h and $t_{04y} = 12$ h may either be fitted without the Warburg element, or with a parameter $p = 0.9 \dots 0.95$. Parameter R_w is found to be of the order of $R_w \approx 1 \times 10^5 \dots 10^6$. Parameter K decreases from $K \approx 0.15 \dots 0.30$ for the first recordings to $K \approx 0.006 \dots 0.02$ after $t_{04t} = 6$ h and $t_{04y} = 12$ h, respectively.

The volume of the electrolyte, $V \approx 100 \text{ mm}^2 \times 0.1 \text{ mm} \approx 10 \text{ mm}^3$, is about one million times the volume of the entire polyimide. Therefore, it is reasonable to assume a constant concentration of ions and water molecules (the PI surface remains always covered with the electrolyte) at the PI-electrolyte interface over time. The solution to Fick's equation (7.10) is then given by the error function complement,

$$c(x_d, t) = c_{el-pi} \operatorname{erfc} \left(\frac{x_d}{2\sqrt{D_d t}} \right), \quad (6.8)$$

with the coordinate x perpendicular to the PI's surface and the diffusion length \sqrt{Dt} . c_{El-PI} is the concentration of the diffusing species at the electrolyte-polyimide interface [259]. See Appendix 7.1 for the concentrations of the components of the PbS- and control medium electrolytes. The manufacturer of the PI 2611, HDMicrosystems, gives an initial concentration for water of $c_{H_2O} \approx 0.5\%$ [84].

Figure 6.31 illustrates the proposed diffusion-like penetration of the polyimide's surface region by components of the electrolyte. The concentration

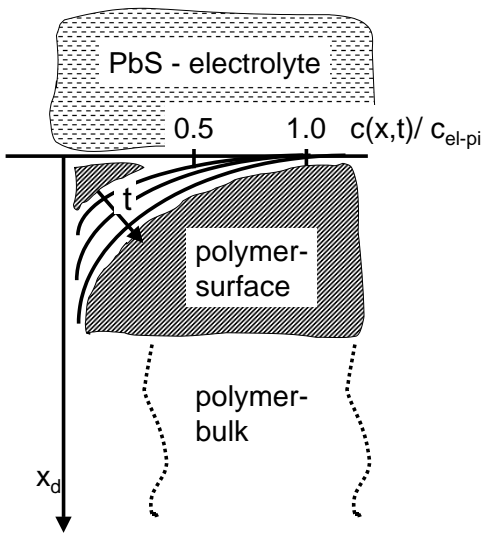


Figure 6.31: Schematic diagram for electrolyte components entering the polymer surface. Assuming a diffusion-like process, the error function compliment governs the concentration C of a diffusing species at any depth x perpendicular to the materials surface. C_s is the (constant) boundary concentration, see text.

$c(x, t)$ of a diffusing species is normalized with the interface concentration c_{el-pi} . Assuming a constant diffusion coefficient in the surface region of the material, $D_{(d),s} = \text{const.}$, the diffusion length \sqrt{Dt} increases with time, thus raising the concentration of the diffusing species perpendicular to the material's surface as indicated. The diffusion process continues in the bulk material. As spectra do not change significantly after $t \approx 24$ hours, the diffusion constant $D_{(d),b}$ in the polymer bulk is assumed to be lower than near the surface. One or two weeks after the assembly of the electrochemical cell, the reproducibility of the spectra decreases. This is, however, most likely related to alterations in the experimental setup such as an oxydation of the Ag-contact stripes or water uptake by the EVA based sealing.

6.3.5 Summary: PI 2611

The observations of the impedance spectroscopy on ultra-thin PI test samples contribute to the assessment of the **biostability** of the material in two ways:

(i) The observed diffusion-like process of PbS electrolyte components into the PI's surface explains the FTIR and XPS analysis of the samples. The "water rinse experiment" shows that with increasing time of exposure to the control-medium, the effect of a prolonged water-rinsing of the sample (ie. a prolonged cleaning of the sample) on the XPS spectra decreases, see section 6.3.2.3. The question rises if the C 1s spectra are to be explained by an alteration of the BPDA/PPD backbone structure of the PI or by co.-me. which penetrates deeper into the PI's surface with increasing time of co.-me. exposure. The results of the impedance spectroscopy support the model that control medium penetrates into the PI in a similar manner as PbS does. Thus a "smooth" interface region at the PI's surface evolves where co.-me. residues are embedded in the BPDA/PPD matrix and result in a "diluted" XPS spectrum of the PI. IS thus also reconciles the FTIR spectra which show an increase in the total number of C-H - and C=C benzene bonds (Fig. (6.17)), with the XPS spectra which indicate a decrease of the C-C peak, accompanied by the raise of the C-N component (Fig. (6.19) and (6.21).

(ii) As PbS electrolyte enters the surface region of the PI, the shunt resistance of the (bulk) material remains above the measurement range of the Schlumberger- and EG & G measurement setup. Hence, the insulation capabilities of the test layers after up to three weeks exposure to in-vitro cell cultures remain intact. Moreover, since the FTIR spectroscopy shows no decrease in the PI's specific absorption bands, the water uptake does not lead to the break up of bonds in the BPDA/PPD backbone.

Electrolyte components (of the in-vivo environment of an implanted device) which eventually reach the PI-chip interface may have a negative effect on the adhesion properties of the encapsulation layer. However, following unpublished preliminary results of implanted (subretinal and subcutaneous) PI 2611 test samples, no delamination problems whatsoever occurred during the implantation period of one year [1].

Chapter 7

Appendix

7.1 Composition of the Dulbecco's growing medium and the phosphate buffered saline

Table 7.1 lists the composition of the Dulbecco's Phosphate Buffered Saline (PbS) that is used throughout this work [260].

Table 7.1: *Contents of Dulbecco's Phosphate Buffered Saline (PbS).*

Component	Concentration g l^{-1}
KCl	0.2
KH_2PO_4 (anhyd)	0.2
NaCl	8.0
Na_2HPO_4 (anhyd)	1.15

Table 7.2 lists the composition of Dulbecco's cell culture medium [261, 262]. "A" indicates amino acids; "V" marks specific vitamins. For a description of enzymes and vitamins see references [7, 263].

Table 7.2: *Contents of Dulbecco's MEM cell culture medium. The concentration C of each component is given. "A" indicates amino acids; "V" marks specific vitamins.*

Component	C	Component	C
	mg l ⁻¹		mg l ⁻¹
NaCl	6400	L-Methionine	A 30
KCl	400	L-Phenylalanine	A 66
CaCl ₂	200	L-Threonine	A 95
MgSO ₄ · 7H ₂ O	200	L-Tryptophan	A 16
NaH ₂ PO ₄	124	L-Tyrosin	A 72
D-Glucose	4500	L-Valine	A 94
Fe(NO ₃) ₃ · 9H ₂ O	0.1	Glycine	A 30
Na-Pyruvat	110	L-Serine	A 42
Phenolred	15		
NaHCO ₃	3700	Cholinchloride	4
		Folic acid	V B9 4
L-Arginine · HCL	A 84	myo-Inositol	7.2
L-Cystine	A 48	Nicotinamide	V B3 4
L-Glutamine	A 580	D-Ca-Pantothenate	V B5 4
L-Histidine · HCL · H ₂ O	A 42	Pyridoxal · HCL	V B6 4
L-Isoleucine	A 105	Riboflavin	V B2 0.4
L-Leucine	A 105	Thiamin · HCL	V B1 4
L-Lysine · HCL	A 146		

7.2 RC-line- and Warburg impedance

The following analysis demonstrates the analogy between the impedance of a finite length RC transmission line and the Warburg impedance of a diffusion process.

Figure 7.1 depicts the equivalent circuit for any transmission line of infinitesimal length dz . The physical length of the "real" transmission line is given by l . R' , L' , G' and C' represent the per unit length (p.u.l.) resistance, p.u.l. inductance, p.u.l. shunt conductance and p.u.l. capacitance of the line, respectively. The voltage signal is given by u ; i represents the electric

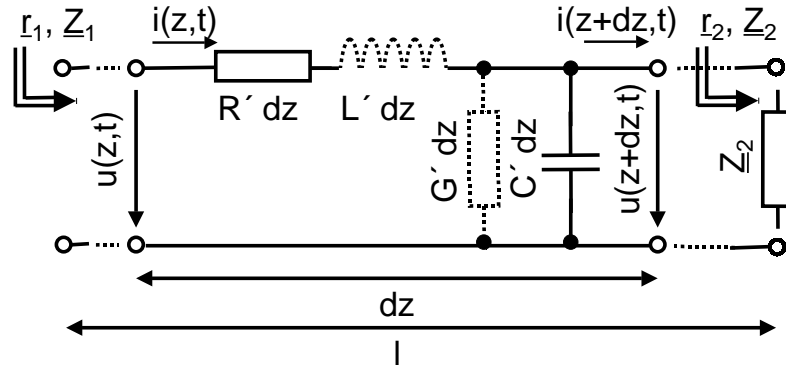


Figure 7.1: RLGC- equivalent circuit for a transmission line of infinitesimal length dz . l indicates the physical length of the "real" transmission line. R' = per unit length (p.u.l.) resistance, L' = p.u.l. inductance, G' = p.u.l. shunt conductance and C' = p.u.l. capacitance. The dotted circuit elements for L and G are neglected in the mathematical analysis, see text. Z_1 is the input impedance of the line terminated by Z_2 .

current. Z_2 represents the impedance terminating the line of length l . Z_1 symbolizes the input impedance of the line of length l . r_2 is the reflection coefficient of Z_2 and r_1 that of Z_1 for a stationary state.

For u holds

$$u(z + dz, t) = u(z, t) - R'dz i(z, t) - L'dz \frac{\partial i(z, t)}{\partial t} \quad (7.1)$$

$$-\frac{u(z + dz, t) - u(z, t)}{dz} = R'i(z, t) + L' \frac{\partial i(z, t)}{\partial t}. \quad (7.2)$$

With $dz \rightarrow 0$ follows

$$-\frac{\partial u(z, t)}{\partial z} = R'i(z, t) + L' \frac{\partial i(z, t)}{\partial t}. \quad (7.3)$$

Similarly, for i holds

$$i(z + dz, t) = i(z, t) - G'dz u(z + dz, t) - C'dz \frac{\partial u(z + dz, t)}{\partial t} \quad (7.4)$$

$$-\frac{\partial i(z, t)}{\partial z} = G'u(z, t) + C' \frac{\partial u(z, t)}{\partial t}. \quad (7.5)$$

In the following analysis the p.u.l. shunt conductance and p.u.l. inductance of the line are neglected, ie., $G' = L' = 0$:

$$-\frac{\partial u(z, t)}{\partial z} = R'i(z, t) \quad (7.6)$$

$$-\frac{\partial i(z, t)}{\partial z} = C' \frac{\partial u(z, t)}{\partial t} \quad (7.7)$$

Applying the operator $\frac{\partial}{\partial z}$ to the first equation yields

$$\frac{\partial^2 u}{\partial z^2} = R'C' \frac{\partial u}{\partial t}. \quad (7.8)$$

Similarly, application of $\frac{\partial}{\partial t}$ to the first equation and of $\frac{\partial}{\partial z}$ to the second equation gives

$$\frac{\partial^2 i}{\partial z^2} = R'C' \frac{\partial i}{\partial t}. \quad (7.9)$$

see reference [258] p. 50. Both wave-equations are structurally identical with Fick's second law of diffusion,

$$\frac{\partial C(x, t)}{\partial t} = D \frac{\partial^2 C(x, t)}{\partial x^2}, \quad (7.10)$$

with the concentration C of the diffusing species and the coordinate x along the diffusion path, see section 6.3.4.3. For a sinusoidal signal in a RC line, the propagation constant $\underline{\gamma}$, $\underline{\gamma} = \alpha + j\beta$ with the attenuation constant α and the phase constant β , is given by

$$\underline{\gamma} = \sqrt{j\omega R'C'}. \quad (7.11)$$

For the characteristic impedance \underline{Z}_c holds

$$\underline{Z}_c = \sqrt{\frac{R'}{j\omega C'}}. \quad (7.12)$$

The reflection coefficients \underline{r}_1 and \underline{r}_2 at the beginning and at the end of the RC line in Figure 7.1, respectively, are given by

$$\underline{r}_1 = \underline{r}_2 \exp\{-2\gamma l\} \quad (7.13)$$

$$\underline{r}_2 = \frac{\underline{Z}_2 - \underline{Z}_c}{\underline{Z}_2 + \underline{Z}_c}. \quad (7.14)$$

For $\underline{Z}_2 \rightarrow 0$, ie. a short-circuit terminated RC line, holds $\underline{r}_2 = -1$ and \underline{Z}_{1sc} becomes

$$\underline{Z}_{1sc} = \underline{Z}_c \frac{1 - \exp\{-2\gamma l\}}{1 + \exp\{-2\gamma l\}} \quad (7.15)$$

$$\underline{Z}_{1sc} = \sqrt{\frac{R'}{j\omega C'}} \frac{1 - \exp\{-2\sqrt{j\omega R' C'} l\}}{1 + \exp\{-2\sqrt{j\omega R' C'} l\}} \quad (7.16)$$

$$\underline{Z}_{1sc} = R' l \frac{1}{\sqrt{j\omega R' C'} l} \tanh \sqrt{j\omega R' C'} l, \quad (7.17)$$

which is analogous to equation (6.5) for the Warburg diffusion impedance,

$$\underline{Z}_W = \frac{R \tanh(iK\omega)^p}{(iK\omega)^p}, \quad (7.18)$$

with $p = 0.5$.

Abbreviations and constants

a-Si:H	hydrogenated amorphous silicon
AMD	Age Related Macula Degeneration
AP 8000	3-aminopropyltriethoxysilane, Dow Chemical
ATCC	American <i>type culture collection</i> (http://www.atcc.org)
BCB	dry-etch <i>benzocyclobutene</i> , Dow Chemical
BPDA / PPD	<i>biphenyldianhydride</i> / 1,4 <i>phenylenediamine</i> (a polyimide)
c-Si	crystalline silicon
CMOS	complementary metal-oxide semiconductor technology
Dulbecco's medium	cell growing medium, see appendix for components
EDX	energy dispersive X-ray diffraction
EVA	<i>Ethylen/Vinyl/Acetate</i> copolymers
FTIR	Fast Fourier Transmission Infrared Spectroscopy
HMDSO	<i>hexamethyldisiloxane</i>
IMS	IMS CHIPS, Institute for microelectronics Stuttgart
IgR	image reversal (photoresist, lithography)
IR	infrared electromagnetic radiation
ISO	International Organization for Standardization
ITO	indium tin oxide
MCT	HgCdTe infrared detector in spectrometer
MEA	micro-electrode array
MPD	Micro-Photodiode

MPDA	Micro-Photodiode Array
NMI	Natural and Medical Science Institute at the University of Tübingen
NMP	<i>n</i> -nethyl-2-pyrrolidone
RIE	reactive ion etch
RP	Retinitis Pigmentosa
RW	reference wafer for infrared spectroscopy
PbS	Phosphate buffered saline
PECVD	plasma enhanced chemical vapor deposition
PI	polyimide
PI 2611	polyimide 2611, HD Microsystems, DuPont
PMDA – ODA	<i>Pyromellitic Dianhydride-Oxydianiline</i> (a polyimide)
RCS rats	Royal College of Surgeons rats
SEM	scanning electron microscope
TCO	transparant conductive oxide
TEOS	<i>tetra-ethyl-ortho-silicate</i>
UAK	University Eye Hospital Tübingen
USP	U.S. Pharmacopaia, an organization for the standardization of medicines
UV	ultraviolet electromagnetic radiation
XPS	X-ray photoelectron spectroscopy
XRD	X-ray diffraction
ϵ_0	universal dielectric constant, $\epsilon_0 = 8.854 \cdot 10^{-12} \text{ A s V}^{-1}\text{m}^{-1}$
j	the imaginary unit, $j = \sqrt{-1}$
k	Boltzman constant, $k = 1.28 \times 10^{-23} \text{ J K}^{-1}$
q	elementary charge, $q = 1.6 \times 10^{-19}\text{C}$
\hbar	Planck's constant, $\hbar = 1.054 \cdot 10^{-34} \text{ Js}$ $\hbar = h/2\pi$

Symbols

$\alpha(l)$	absorption coefficient of light in specified material	(cm^{-1})
$\alpha(e^-)$	absorption coefficient for photoelectrons	(nm^{-1})
ϵ_{EVA}	dielectric constant of EVA, $\epsilon_{EVA} \approx 3-4$	
ϵ_{H_2O}	dielectric constant of H ₂ O	
$\epsilon_{r,BCB}$	dielectric constant of BCB ($\epsilon_{r,BCB}=2.65$)	
$\epsilon_{r,PI}$	dielectric constant of PI ($\epsilon_{r,PI}=2.8$)	
η_{a-Si}	conversion efficiency of a-Si:H based photodiodes	(%)
$\theta_{b,E}$	bond angle of ether group in PI	($^\circ$)
ϑ	detection angle of the XPS analyser	($^\circ$)
κ	phase angle of the constant phase element	
λ	attenuation length of photoelectrons	(monolayers)
λ_{att}	attenuation length of photoelectrons	(nm)
λ_l	wavelength of light	(nm)
ν	wave number	(cm^{-1})
$\rho_{(BICR),s}$	density of BICR "Marshall" cells at saturation	(cm^{-2})
$\rho_{(w),l}$	resistivity of wafer substrates, highly doped	($\Omega \text{ cm}$)
$\rho_{(w),h}$	resistivity of wafer substrates, lowly doped	($\Omega \text{ cm}$)
τ	time constant for fit of element concentration (XPS)	(h ⁻¹)
ϕ	phase angle between voltage and current signal	($^\circ$)
φ	work function	(eV)
ω	angular frequency	(s ⁻¹)
a	prefactor for fit of element concentrations (XPS)	
A	amplitude of the constant phase element	($\text{F}^\kappa \text{S}^{1-\kappa} \text{cm}^{-2}$)
A_1	(small-scale) area of PI with greater or smaller thickness than average	(μm^2)
A_2	(small-scale) area of PI with average thickness	(μm^2)

A_α	percentage of photoelectrons emitted between $d = 0 \dots \alpha$ which contribute to XPS peaks	(%)
A_{ce}	area of counter electrode	(μm^2)
A_{cv}	area of contact via	(μm^2)
A_{EVA}	sample area in contact with EVA	(mm^2)
A_p	peak area in Gaussian or Lorentzian distribution	
A_s	surface area of cell culture samples	(mm^2)
A_{se}	area of stimulation electrode	(μm^2)
$A_{PbS,EVA}$	surface area of electrodes in electrolyte cell setup.	(mm^2)
A_{PbS}	sample area in contact with PbS	(mm^2)
app	absolute percentage points	
b_i	XPS background at channel i	
c	element concentration (XPS)	(%)
c_{CO_2}	CO ₂ concentration in incubator	(%)
c_{Na^+}	concentration of Na ⁺ ions in electrolyte	(l^{-1})
c_0	constant for fit of element concentrations (XPS)	
c_{el-pi}	concentration of the diffusing species at the electrolyte–polyimide interface	(cm^{-2})
c_{moe}^{abs}	margin of error for concentration of elements (XPS) in absolute percentage points	
$c_{(IR),Si-N}$	change in concentration of Si-N bonds as determined by FTIR	(%)
$c_{(H),X}^{abs}$	change in concentration of element X as determined by XPS in absolute percentage points after HeLa cell-culture treatment	(%)
$c_{(M),X}^{abs}$	change in concentration of element X as determined by XPS in absolute percentage points after Marshall cell-culture treatment	(%)
$c_{(H,t),X}^{abs}$	change in concentration of element X as determined by XPS in absolute percentage points after HeLa cell-culture and trypsinization	(%)
c_X^{abs}	change in concentration of element X as determined by XPS in absolute percentage points	(%)
c_X^{rel}	change in concentration of element X as determined by XPS in relative percentage points	(%)
$c(x, t)$	concentration of diffusing species	(cm^{-2})
C	capacitance of a plane capacitor	(F), $F = \text{A s V}^{-1}$
C_{io}	capacitance of the inorganic dielectric	(F)
$C_{(io),c}$	capacitance of the inorganic dielectric as fitted with circuit (c)	(F)
$C_{(io),H}$	capacitance of the inorganic dielectric after HeLa cell culture treatment	(F)

$C_{(io),cm}$	capacitance of the inorganic dielectric after co.-me. treatment	(F)
C_p	capacitance in a parallel RC element	(F)
C'	per unit length capacitance	(C m ⁻¹)
$C_{(PI),th}$	theoretical capacitance of PI samples following equation for a plance capacitor	(F)
$C_{(PI),ev.}$	capacitance of PI samples after contact evaporation	(F)
$C_{(PI),el.}$	capacitance of PI samples in electrolyte cell setup	(F)
$C_{(PI),g.l.}$	capacitance of PI samples after gold leaf contacting	(F)
$C_{(PI),r.s.}$	capacitance of PI samples with rough surface	(F)
C_{de}	Capacitance of dielectric	(F)
C_g	geometric capacitance of electrolyte cell setup	(F)
C_{HH}	helmholtz double layer capacitance	(F))
d	emission depth of photoelectrons	(m)
$d_{(BCB),cm}$	thickness of commercially available BCB	(μ m)
d_{Cr-W}	geometric separation between Cr-electrode and wafer substrate	(μ m)
d_{HH}	separation between inner Helmholtz plane and the solid	(nm)
d_{hill}	lateral dimension of PI hillocks in SEM	(nm)
d_{if}	thickness of PI – electrolyte interface	(nm)
d_{io}	thickness of inorganic samples	(nm)
d_{max}	maximum peak-to-valley distance in PI	(nm)
$d_{PI-1,2,3,4}$	thickness of PI samples of PI series 1, 2, 3, 4	(nm)
\bar{d}_{PI}	average thickness of PI samples (in model for surface roughness)	(nm)
Δd_{PI}	deviation from d_{PI}	(nm)
d_{SiN_x}	thickness of SiN _x layer	(nm)
d_{surf}	thickness of surface layer	(nm)
d_{tl}	thickness of modelled top layer (XPS)	(nm)
$d_{(tl),t=x}$	thickness of modelled top layer (XPS) after $t = x$ days	(nm)
d_{ss}	dissolution rate of SiN _x in control medium	(nm d ⁻¹)
D	illumination	(W m ⁻²)
D_d	diffusion coefficient	(cm ² s ⁻¹)
$D_{(d),s}$	diffusion coefficient in PI 2611 surface region	(cm ² s ⁻¹)
$D_{(d),b}$	diffusion coefficient in PI 2611 bulk	(cm ² s ⁻¹)
E	energy of electrons in semiconductors	(eV)

E_{Al}	X-ray energy of Al-source, $E_{Al}=1253.6$ eV	(eV)
E_{Mg}	X-ray energy of Mg-source, $E_{Mg}=1486.6$ eV	(eV)
E_b	binding energy	(eV)
$E_{(b),X}$	binding energy of element X	(eV)
E_c	energy at center of Gaussian or Lorentzian peak	(eV)
$E_{(e^-),kin}$	kinetic energy of photoelectrons	(eV)
E_g	band gap	(eV)
$E(\mathbf{k})$	dispersion relationship	
E_p	energy of phonons	(eV)
f	frequency	(Hz), Hz = s ⁻¹
FF	fill factor	(%)
G	conductance	(Ω^{-1})
$G_{1,2,3}$	Gaussian distributions in XPS fit function Y	
G'	per unit length conductance	($\Omega^{-1} \text{ m}^{-1}$)
$h\nu$	photon energy	(eV)
$i(t)$	time dependent current	(A)
I	current	(A)
\underline{I}	complex current	(A)
I_0	saturation current	(mA)
i_c	current charging the Helmholtz capacitance	(mA)
i_f	faradaic current across Helmholtz layer	(mA)
j	total angular momentum of core electrons	
I_{mpp}	current at maximum power point	(mA)
I_{ph}	photocurrent	(mA)
I_s	stimulation current	(mA)
$I(V)$	current-voltage characteristics	
I_{sc}	short-circuit current	(mA)
K	parameter in Warburg impedance, $K = l_{diff}^2/D_{diff}$	(s)
\mathbf{k}	wave vector	
k	prefactor in XPS-background calculation	
k_F	spring constant in Hooke's law	(kg s ⁻²)
kT	thermal energy	(meV)
l	physical length of the "real" RC line	(m)
l_d	diffusion thickness	(m)
l_{oam}	orbital angular momentum of core electrons	
$L_{1,2,3}$	Lorentzian distributions in XPS fit function Y	
L	inductance	(H), H = V s A ⁻¹
L'	per unit length inductance	(H m ⁻¹)
m	mass of atoms in Hooke's law	(kg)
$m_{1,2,3}$	prefactor in XPS fit function Y	
MFP	mean free path of photoelectrons	(nm)

$MOE_{(A),PbS}$	margin of error of sample area in contact with PbS	(%)
n	ideality factor	
nip, pin	sequence of doped and intrinsic a-Si:H layers	
nipnip	sequence of doped and intrinsic a-Si:H layers	
p	exponent in Warburg impedance, $p = 0.5$ for diffusion	
$p_{(BCB),c}$	pressure in chamber during BCB curing	(Pa), Pa = N m ⁻² 1 Pa = 10 ⁻⁵ bar
p_j	peak amplitude for XPS background calculation	
pp	percentage points	
$P(d)$	probability as function of emission depth	
Q	Charge	(C), C = A s
r_{Au}	sputter-deposition rate for Au on dielectrics	(nm min ⁻¹)
r_H	hydrogen dilution of a-Si:H	
R	resistance	(Ω)
R'	per unit length resistance	(Ω m ⁻¹)
R_{de}	shunt resistance of dielectric	(Ω)
R_{HH}	shunt resistance of Helmholtz layer	(Ω)
R_{io}	bulk resistance of inorganic dielectric	(Ω)
$R_{X/Y}$	peak ratio of elements (or bonds) X and Y (XPS)	
$R_{(PI),th}$	theoretical conductance of PI (manufacturer's data)	(Ω)
R_g	shunt resistance of the electrolyte cell setup	(Ω)
R_p	shunt resistance of a a-Si:H- or c-Si photodiode	(Ω)
$R_{(PI),ev.}$	resistance of PI samples after contact evaporation	(Ω)
$R_{(PI),el.}$	resistance of PI samples in electrolyte cell setup	(Ω)
$R_{(PI),g.l.}$	resistance of PI samples after gold leaf contacting	(Ω)
R_{sh}	shunt resistance	(Ω)
$R_{(sh),w}$	shunt resistance for Warburg diffusion element	(Ω)
R_s	series resistance	(Ω)
R_{s1}	series resistance in equivalent circuit	(Ω)
R_{s2}	series resistance in equivalent circuit	(Ω)
$R_{s,\Sigma}$	total series resistance for $f \rightarrow \infty$	(Ω)
$R_{(a-Si),s}$	series resistance of a-Si:H photodiodes	(Ω)
R_t	tissue resistance	(Ω)
R_w	prefactor in the Warburg impedance	(Ω)
$R_{(w),h}$	resistivity of substrate wafer, high resistivity	(Ω cm)
$R_{(w),l}$	resistivity of substrate wafer, low resistivity	(Ω cm)
s	spin of core electrons	
S X	XPS subpeak concentration, (eg., X = C-N)	

$\int X$	element concentration in the total XPS spectrum, X = Si, O, N, C	(%)
S_{de}	FTIR spectra of dielectrics	
S_n	normalized FTIR spectra	
S_{rw}	FTIR spectra of reference wafer	
t	time	(h)
$t_{co.-me.}$	time of exposure to the co.-me.	(h)
t_0	start of measurement	
$t_{1,3}$	timeframe, see XPS (SiN_x)	(d)
$t_{2,X}$	time until equilibrium for concentration of element X is reached (XPS)	(d)
$t_{(BICR),d}$	doubling time of BICR "Marshall" cell culture	(h)
t_{pic}	time between removal of petri dishes from incubator and recording of optical microscope pictures	(min)
t_{rinse}	amount of time the sample is rinsed in deionized water	(min)
t_{st}	duration of sterilization of cell culture samples	(h)
T	absolute temperature	(K)
T_{an}	annealing temperature	(K)
$T_{(BCB),c}$	final BCB cure temperature	(°C), $1^\circ\text{C} = 273 \text{ K}$
$T_{(a-Si),d}$	deposition temperature of a-Si:H	(°C), $\frac{1^\circ\text{C}}{0.555} + 32 = 1^\circ\text{F}$
$T_{co.-me.}$	temperature of co.-me.	(°C)
$T_{(SiN_x),d}$	deposition temperature of SiN_x	(°C)
$T_{(TEOS),d}$	deposition temperature of TEOS SiO_2	(°C)
T_{FTIR}	operating temperature of MCT detector	(K)
T_{gtt}	glass transition temperature	(°C)
$T_{h.o.}$	hot-oven temperature during sterilization	(°C)
T_{inc}	temperature in incubator	(°C)
T_{PbS}	temperature of PbS at time of removal of living cells from samples	(°C)
$T_{(PI),c}$	final PI cure temperature	(°C)
T_{tryp}	temperature of trypsin during trypsinization	(°C)
T_{pic}	temperature during recording of optical microscope pictures	(°C)
$T(t)$	temperature ramp during curing process	
V	voltage	(V)
V_0	amplitude of sinusoidal voltage signal	(V)
\underline{V}	complex voltage	(V)
V_{ch}	polarization voltage of stimulation electrode	V
V_{mpp}	voltage at maximum power point	(V)
V_{oc}	open circuit voltage	V
V_{se-ce}	stimulation electrode – counter electrode potential	(V)
w	full width at half maximum	(eV)

x	displacement of atoms in Hooke's law	(m)
x_d	coordinate along the diffusion path	(m)
y_0	offset in XPS fit function Y	
Y	function composed of Gaussian and Lorentzian distributions for XPS fit algorithm	
\underline{Y}	admittance	(Ω^{-1})
z	coordinate along RC line	(m)
\underline{Z}	impedance	(Ω)
\underline{Z}_1	input impedance of RC line of length l	(Ω)
\underline{Z}_2	impedance terminating the RC line	(Ω)
\underline{Z}_w	Warburg impedance	(Ω)

Bibliography

- [1] K. Kohler and M. Stelzle, unpublished, project meeting, 2002.
- [2] W. Bargmann, *Histologie und Mikroskopische Anatomie des Menschen*, 1st ed. (Thieme Verlag, Stuttgart, 1977), p. 657.
- [3] E. Zrenner, K.-D. Miliczek, V. P. Gabel, H. G. Graf, E. Guenther, H. Haemmerle, B. Hoefflinger, K. Kohler, W. Nisch, M. Schubert, A. Stett, and S. Weiss, *Ophthalmic Res* **29**, 269 (1997).
- [4] E. Zrenner, *Science* **295**, 1022 (2002).
- [5] Schmidt, *Physiologie Kompakt*, 3rd ed. (Springer Verlag, Berlin, Heidelberg, 1999).
- [6] Schmidt, *Grundlagen der Sinnesphysiologie*, 3rd ed. (Springer Verlag, Berlin, Heidelberg, 1977).
- [7] L. Stryer, *Biochemistry*, 3rd ed. (W. H. Freeman and Company, New York, 1988), p. 1029.
- [8] S. Deetjen, *Physiologie*, 3rd ed. (Urban und Fischer, München, Stuttgart, 1999), pp. 93–113.
- [9] C. von Campenhausen, *Die Sinne des Menschen*, 2nd ed. (Georg Thieme, Stuttgart, 1993), pp. 99–234.
- [10] Pro Retina Deutschland e.V, <http://www.pro-retina.de/index.html>.
- [11] G. E. Tassiker, US Patent No. 2,760,483, 1956.
- [12] G. S. Brindley and W. S. Lewin, *J. Physiol.* **196**, 479 (1968).
- [13] E. M. Schmidt, M. J. Bak, F. T. Hambrecht, C. V. Kufta, D. K. O'Rourke, and P. Vallabhanath, *Brain* **119**, 507 (1996).
- [14] W. H. Dobbelle and M. G. Mladejovsky, *J. Physiol.* **243**, 553 (1974).

- [15] W. H. Dobelle, *ASAIIO Journal* 1 (2000).
- [16] G. Peyman, A. Y. Chow, C. Liang, V. Y. Chow, J. I. Perlman, and N. S. Peachey, *Ophthalmic Surgery and Lasers* **29**, 234 (1998).
- [17] M. S. Humayun, E. de Juan, G. Dagnelie, R. J. Greenberg, R. H. Propst, and H. Phillips, *Arch Ophthalmology* **114**, 40 (1996).
- [18] M. S. Humayun, E. de Juan, J. D. Weiland, G. Dagnelie, S. Katona, R. Greenberg, and S. Suzuki, *Vision Research* **39**, 2569 (1999).
- [19] M. T. Pardue, E. B. S. Jr., J. I. Perlman, K. Narfstroem, A. Y. Chow, and N. S. Peachey, *Exp. Eye Res.* **73**, 333 (2001).
- [20] H. Haemmerle, B. Hoefflinger, M. B. Schubert, and E. Zrenner, 9. Forumsgespraech der Gesellschaft fuer Biomedizinische Technologien in Ulm e.V., 28. Nov. 1997.
- [21] E. Zrenner, F. Gekeler, V. P. Gabel, H. G. Graf, M. Graf, E. Guenther, H. Haemmerle, B. Hoeffliner, K. Kobuch, K. Kohler, W. Nisch, H. Sachs, B. Schlosshauer, M. Schubert, H. Schwahn, M. Stelzle, A. Stett, B. Troeger, and S. Weiss, *Ophthalmologie* **98**, 357 (2001).
- [22] M. Stelzle, A. Stett, B. Brunner, M. Graf, and W. Nisch, *Biomedical Microdevices* **3**, 133 (2001).
- [23] K. Kobuch, H. Sachs, E. Zrenner, and V.-P. Gabel, *Invest. Ophthalmol. Vis. Sci.* **39**, 903 ff (1998).
- [24] A. Y. Chow, M. T. Pardue, V. Y. Chow, G. A. Peyman, C. Liang, J. I. Perlman, and N. S. Peachey, *IEEE Trans Neurol Systems and Rehabilitation Engineering* **9**, 86 (2001).
- [25] K. Kohler, J. A. Hartmann, D. Werts, and E. Zrenner, *Ophthalmologie* **98**, 364 (2001).
- [26] P. Walter, P. Szurman, M. Vobig, H. Berk, H.-C. Luedtke-Handjery, H. Richter, Deng, C. Mittermayer, K. Heimann, and B. Sellhaus, *Retina. The Journal of Retinal and Vitreous Diseases* **19**, 546 (1999).
- [27] R. Eckmiller, *Ophthalmic Research* **29**, 281 (1997).
- [28] J. Wyatt and J. Rizzo, *IEEE Spectrum* **May**, 47 (1996).
- [29] A. E. Grumet, J. L. W. Jr., and J. F. Rizzo, *J. of Neuroscience Methods* **101**, 31 (2000).

- [30] R. E. Eckmiller, Int. Conf. Neural Inf. Processing Proc. **2**, 21 (1996).
- [31] T. Poggio and D. Beymer, IEEE Spectrum **33**, 60 (1996).
- [32] M. Schwarz, L. Ewe, R. Hauschild, B. J. Hosticka, J. Huppertz, S. Kolnsberg, W. Mokwa, and H. K. Trieu, Sensors and Actuators **83**, 40 (2000).
- [33] H. Schwahn, F. Gekeler, K. Kohler, K. Kobuch, H. G. Sachs, F. Schulmeyer, W. Jakob, V.-P. Gabel, and E. Zrenner, Graefe's Arch Clin Exp Ophthalmol **239**, 961 (2001).
- [34] R. Eckhorn, A. Stett, T. Schanze, F. Gekeler, H. Schwahn, E. Zrenner, M. Wilms, M. Eger, and L. Hesse, Ophthalmologie **98**, 369 (2001).
- [35] K. Kohler, E. Guenther, and E. Zrenner, Klin Monatsbl Augenheilkd **211**, 84 (1997).
- [36] A. Stett, W. Barth, S. Weiss, H. Haemmerle, and E. Zrenner, Vision Research **40**, 1785 (2000).
- [37] E. Zrenner, A. Stett, S. Weiss, R. B. Aramant, E. Guenther, K. Kohler, K.-D. Miliczek, M. J. Seiler, and H. Haemmerle, Vision Research **39**, 2555 (1999).
- [38] A. Y. Chow and V. Y. Chow, Neuroscience Letters **225**, 13 (1997).
- [39] A. Stett, K. Kohler, S. Weiss, H. Haemmerle, and E. Zrenner, Invest. Ophthalmol. and Vis. Sci. **39**, 162 (Abstract) (1998).
- [40] D. Braun and P. Fromherz, Phys. Rev. Lett. **86**, 2905 (2001).
- [41] A. Stett and P. Fromherz, Phys. Rev. E **55**, 1779 (1997).
- [42] P. Fromherz and A. Stett, Phys. Rev. Lett. **75**, 1670 (1995).
- [43] U. Henze, G. Zwadlo-Klarwasser, B. Klosterhalfen, H. Hoecker, H. Richter, and C. Mittermayer, Deutsches Aerzteblatt **96**, 756 (1999).
- [44] H. Haemmerle, K. Kobuch, K. Kohler, W. Nisch, H. Sachs, and M. Stelzle, Biomaterials **23**, 797 (2002).
- [45] P. Fromherz, Email, personal communication, 2001.
- [46] R. A. Street, *Hydrogenated Amorphous Silicon*, 1st ed. (Cambridge University Press, Cambridge, New York, 1991), p. 62 ff.

- [47] J. D. Joannopoulos and G. Lucovsky, *The Physics of Hydrogenated Amorphous Silicon II*, 1st ed. (Springer Verlag, Berlin, Heidelberg, 1984), p. 15.
- [48] N. W. Ashcroft and N. D. Mermin, *Solid State Physics*, 1st ed. (Saunders College Publishing, Harcourt Brace College Publishers, Fort Worth, Philadelphia, 1976), p. 562 ff.
- [49] S. J. Fonash, *Solar Cell Device Physics*, 1st ed. (Academic Press Inc., San Diego, California, 1981), pp. 9–30.
- [50] S. Veprek, F. A. Sarott, and Z. Iqbal, *Phys. Rev. B* **36**, 3344 (1987).
- [51] D. Beeman, R. Tsu, and M. F. Thorpe, *Physical Review B* **32**, 874 (1985).
- [52] N. Maley, D. Beeman, and J. S. Lannin, *Phys. Rev. B* **38**, 10611 (1988).
- [53] H. M. Branz, *Physical Review B* **59**, 5498 (1999).
- [54] A. V. Keudell and J. R. Abelson, *J. Appl. Phys.* **84**, 489 (1998).
- [55] R. A. Street, *Hydrogenated Amorphous Silicon*, 1st ed. (Cambridge University Press, Cambridge, New York, 1991), p. 81 ff.
- [56] G. D. Cody, T. Tiedje, B. Abeles, B. Brooks, and Y. Goldstein, *Physical Review Letters* **47**, 1480 (1981).
- [57] J. Tauc, *Amorphous and Liquid Semiconductors*, 1st ed. (Plenum Press, London and New York, 1974), p. 227 ff.
- [58] T. Akin, K. Najafi, R. H. Smoke, and R. M. Bradley, *IEEE Trans. on Biomed. Engineering* **41**, 305 (1994).
- [59] M. Rojahn and M. B. Schubert, *Mat. Res. Soc. Symp. Proc.* **609**, A21.4.1 (2000).
- [60] J. Yang, A. Banerjee, and S. Guha, *Appl. Phys. Lett.* **70**, 2975 (1997).
- [61] P. Alpuim and J. P. Conde, *J. Appl. Phys.* **86**, 3812 (1999).
- [62] C. Koch, M. Ito, V. Svrcek, M. B. Schubert, and J. H. Werner, *Thin Solid Films* **383**, 129 (2001).
- [63] M. B. Schubert, A. Hierzenberger, V. Baumung, H. N. Wanka, W. Nisch, M. Stelzle, and E. Zrenner, *Mat. Res. Soc. Symp. Proc.* **467**, 913 (1997).

- [64] M. B. Schubert, *Thin Solid Films* **337**, 240 (1999).
- [65] Y. Hishikawa and S. Okamoto, *Solar Energy Mat. and Solar Cells* **33**, 157 (1994).
- [66] G. Kroetz, J. Wind, H. Stitzl, and G. Mueller, *Phil. Mag. B* **63**, 101 (1991).
- [67] J. Merten, J. M. Asensi, C. Voz, A. V. Shah, R. Platz, and J. Andreu, *IEEE Trans. on Electron Devices* **45**, 423 (1998).
- [68] J. Merten, C. Voz, A. Munoz, J. M. Asensi, and J. Andreu, *Solar Energy Materials and Solar Cells* **57**, 153 (1999).
- [69] JohnRobertson, *Mat. Res. Soc. Symp. Proc.* **609**, A1.4.1 (2000).
- [70] N. Wyrsh, C. Droz, L. Feitknecht, M. Goerlitzer, U. Kroll, J. Meier, P. Torres, E. Vallat-Sauvain, A. Shah, and M. Vanecek, *Mat. Res. Soc. Symp. Proc.* **609**, A15.1.1 (2000).
- [71] J. Yang, K. Lord, and S. Guha, *Mat. Res. Soc. Symp. Proc.* **609**, A15.4.1 (2000).
- [72] G. Yue, D. Han, J. Yang, and S. Guha, *Mat. Res. Soc. Symp. Proc.* **609**, A5.9.1 (2000).
- [73] S. M. GadelRab, A. M. Miri, and S. G. Chamberlain, *IEEE Trans Electron. Dev.* **45**, 560 (1998).
- [74] J. W. Coburn and H. F. Winters, *J. Vac. Sci. Technol.* **16**, 391 (1979).
- [75] H. Jansen, H. Gardeniers, M. de Boer, M. Elwenspoek, and J. Fluitman, *J. Micromech. Microeng.* **6**, 14 (1996).
- [76] J. M. Frary and P. Seese, *Semiconductor International* 72 (1981).
- [77] S. Tao, Q. Ma, D. Striakhilev, and A. Nathan, *Mat. Res. Soc. Symp. Proc.* **609**, A12.2.1 (2000).
- [78] i. J. Gloeckner, personal communication, unpublished, 2001.
- [79] J. H. Werner, *Appl. Phys. A* **47**, 291 (1988).
- [80] S. S. Hegedus, *Progress in Photovoltaics: Res. and Appl.* **5**, 151 (1997).
- [81] H. Haken and H. C. Wolf, *Atom- und Quantenphysik*, 7th ed. (Springer Verlag, Berlin, Heidelberg, 2000), p. 313.

- [82] C. Koch, M. Ito, and M. B. Schubert, *Solar Energy Materials and Solar Cells* **68**, 227 (2001).
- [83] L. F. Marsal, J. Pallares, A. Orpella, D. Bardes, J. Puigdollers, and R. Alcubilla, *Mat. Res. Soc. Symp. Proc.* **609**, A23.7.1 (2000).
- [84] HDMicrosystems, PI2611 Series – Product information and process guide, 1998.
- [85] J. R. Huang, Y. Lee, T. N. Jackson, and C. R. Wronski, in *26th IEEE Photovoltaic Specialists Conference* (IEEE Inc., Piscatway, 1997), pp. 699–702.
- [86] H. Gleskova, S. Wagner, and Z. Suo, in *Flat-Panel Display Materials Symp., Mat. Res. Soc.* (MRS, Pittsburgh, 1998), pp. 73–78.
- [87] A. Sazonov and A. Nathan, *J. Vac. Sci. Technol.* **18**, 780 (2000).
- [88] i. c. H. Gruber, personal communication, 2002.
- [89] S. Vassanelli and P. Fromherz, *The J. of Neuroscience* **19**, 6767 (1999).
- [90] P. Fromherz, V. Kiessling, K. Kottig, and G. Zeck, *Appl. Phys. A* **69**, 571 (1999).
- [91] M. Jenker and P. Fromherz, *Phys. Rev. Lett.* **79**, 4705 (1997).
- [92] A. N. I. of Health Workshop, October 16-17, 1995.
- [93] P. C. Nicolson and J. Vogt, *Biomaterials* **22**, 3273 (2001).
- [94] D. de Beer, P. Stoodley, F. Roe, and Z. Lewandowski, *Biotechnology and Bioengineering* **43**, 1131 (1994).
- [95] G. M. Bruinsma, H. C. van der Mei, and H. J. Busscher, *Biomaterials* **22**, 3217 (2001).
- [96] S. L. McArthur, K. M. McLean, H. A. W. S. John, and H. J. Griesser, *Biomaterials* **22**, 3295 (2001).
- [97] S. A. Bradley and S. H. Carr, *J. Appl. Phys.* **44**, 4269 (1973).
- [98] L. Lu, M. J. Yaszemski, and A. G. Mikos, *Biomaterials* **22**, 3345 (2001).
- [99] K. E. Uhrich, S. E. M. Ibim, D. R. Larrier, R. Langer, and C. T. Laurencin, *Biomaterials* **19**, 2045 (1998).

- [100] R. F. B. Turner, D. J. Harrison, and R. V. Rajotte, *Biomaterials* **12**, 361 (1991).
- [101] T. Stieglitz, H. Beutel, M. Schuettler, and J.-U. Meyer, *Biomedical Microdevices* **2**, 283 (2000).
- [102] R. R. R. Jr., J. A. Miller, and W. M. Reichert, *Biomaterials* **14**, 627 (1993).
- [103] T. Stieglitz, H. Beutel, R. Keller, C. Blau, and J.-U. Meyer, *IEEE* **5**, 2307 (1997).
- [104] K. E. Uhrich, A. Gupta, T. T. Thomas, C. T. Laurencin, and R. Langer, *Macromolecules* **28**, 2184 (1995).
- [105] X. Navarro, S. Calvet, F. J. Rodriguez, T. Stieglitz, C. Blau, M. Buti, E. Valderrama, and J.-U. Meyer, *J. Peripheral Nervous System* **3**, 91 (1998).
- [106] M. Vetter and M. Rojahn, *Mat. Sci. Eng.* **B71**, 321 (2000).
- [107] M. Vetter, *Thin Solid Films* **337**, 118 (1999).
- [108] H. Lin, L. Xu, X. Chen, X. Wang, M. Shen, F. Stubhan, K.-H. Merkel, and J. Wilde, *Thin Solid Films* **333**, 71 (1998).
- [109] L. Jiang, X. Chen, X. Wang, L. Xu, F. Stubhan, and K.-H. Merkel, *Thin Solid Films* **352**, 97 (1999).
- [110] E. Guenther, B. Troeger, B. Schlosshauer, and E. Zrenner, *Vision Research* **39**, 3988 (1999).
- [111] M. Misawa, T. Fukunaga, K. Niihara, T. Hirai, and K. Suzuki, *J. of Non-Crystalline Solids* **34**, 313 (1979).
- [112] J. Robertson, *Philosophical Magazine B* **63**, 47 (1991).
- [113] D. Dobkin, <http://www.batnet.com/enigmatics/semiconductor-processing/CVD-Fundamentals/films/SiN-properties.html>, 2002.
- [114] R. E. Dickerson, H. B. Gray, and G. P. Haight, *Prinzipien der Chemie*, 2 ed. (Walter de Gruyter Co., Berlin, New York, 1978), p. 548 ff.
- [115] S. Garcia, D. Bravo, M. Fernandez, I. Martil, and F. J. Lopez, *Appl. Phys. Lett* **67**, 3263 (1995).

- [116] P. M. Martin and G. J. Exarhos, *J. Vac. Sci. Technol.* **3**, 615 (1985).
- [117] P. M. Martin, *J. Vac. Sci. Technol.* **2**, 330 (1984).
- [118] W. A. P. Claassen, W. G. J. N. Valkenburg, M. F. C. Willemsen, and W. M. v. d. Wijgert, *J. Electrochem. Soc.* **132**, 893 (1985).
- [119] G. F. Erikson and K. Dyrbye, *J. Micromech. Microeng.* **6**, 55 (1996).
- [120] C. L. Borst, V. Korthuis, G. B. Shinn, J. D. Luttmmer, R. J. Gutmann, and W. N. Gill, *Thin Solid Films* **385**, 281 (2001).
- [121] Y. Travaly, L. Zhang, Y. Zhao, R. Pfeffer, K. Uhrich, F. Cosandey, E. Garfunkel, and T. E. Madey, *J. of Materials Research* **14**, 3673 (1999).
- [122] F. Faupel, T. Strunskus, M. Kiene, A. Thran, and C. v. Bechtolsheim, *Mat. Res. Soc. Symp. Proc.* **511**, 15 (1998).
- [123] J.-H. Im, E. O. S. II, A. S. T. Stokich, Jr., J. Hetzner, J. Curphy, C. Karas, G. Meyers, D. Hawn, A. Chakrabarti, and S. Froelicher, *Trans. of the ASME* **122**, 28 (2000).
- [124] R. H. II, R. DeVellis, P. Garrou, D. Burdeaux, T. Stokich, P. Townsend, T. Manial, L. Bratton, F. David, K. Berry, K. Heighstreet, M. Lanka, and M. Tozer, in *ISHM Proc.* (PUBLISHER, ADDRESS, 1992), pp. 584–590.
- [125] R. F. Kopf, R. A. Hamm, R. W. Ryan, J. Burm, A. Tate, Y.-K. Chen, G. Georgiou, D. V. Lang, and F. Ren, *J. of Electronic Materials* **27**, 954 (1998).
- [126] J.-B. Lee, J. English, C.-H. Ahn, and M. G. Allen, *J. Micromech. Microeng.* **7**, 44 (1997).
- [127] D. J. Peretti, M. J. Radler, and T. Takahashi, The Dow Chemical Company (1995).
- [128] H. M. Clearfield, S. Wijeyesekera, E. A. Logan, A. Luu, D. Gieser, C.-M. Lin, J. Jing, W. B. Rogers, D. Scheck, D. Benson, and J. He, in *IEEE Intern. Conf. on Multichip Modules and High Density Packaging* (IEEE Inc., Piscataway, 1998), pp. 501–505.
- [129] J. Wolf, F. J. Schmueckle, W. Heinreich, M. Toepper, K. Buschick, A. Owzar, O. Ehrmann, and H. Reichl, in *Intern. Symp. on Microelectronics* (IMAPS - Int. Microelectron. and Packaging Soc., Reston, 1997), pp. 29–36.

- [130] H.-M. Heiliger, M. Nagel, H. G. Roskos, H. Kurz, F. Schnieder, W. Heinrich, R. Hey, and K. Ploog, *Appl. Phys. Lett.* **70**, 2233 (1997).
- [131] F. Kuechenmeister, Z. Stavreva, U. Schubert, K. Richter, C. Wenzel, and M. Simmonds, in *Mat. Res. Soc. Proc. ULSI XIV* (MRS, Pittsburgh, 1999), pp. 237–242.
- [132] M. E. Mills, P. Townsend, D. Castillo, S. Martin, and A. Achen, *Microelectronic Engineering* **33**, 327 (1997).
- [133] E. O. S. I. M. E. Mills, D. Hawn, M. van Gestel, A. Knorr, H. Gundlach, K. Kumar, A. E. Kaloyeros, and R. E. Geer, *Mat. Res. Soc. Symp. Proc.* **511**, 133 (1998).
- [134] C. D. Sheraw, D. J. Gundlach, and T. N. Jackson, *Mat. Res. Soc. Symp. Proc.* **558**, 403 (2000).
- [135] J.-H. Lan, T.-K. Chou, C.-S. Chiang, and J. Kanicki, *Mat. Res. Soc. Symp. Proc.* **471**, 27 (1997).
- [136] S. Wolff, A. Grosse, H.-J. Schimper, A. R. Giehl, M. Kuhnke, and R. Grote, *J. Vac. Sci. Technol.* **A 19**, 87 (2001).
- [137] T. Stieglitz, personal communication, 2001.
- [138] H. Beutel, T. Stieglitz, and J. U. Meyer, in *IEEE 11th Annual Intern. Workshop on Micro Electromechanical Systems, IEEE Robotics and Autom. Soc.* (IEEE Inc., Piscataway, 1998), pp. 306–311.
- [139] J. Im, T. S. Jr, J. Hetzner, G. Buske, J. Curphy, E. O. S. II, and G. Meyers, in *Intern. Symp. on Advanced Packaging Materials* (IMAPS - Int. Microelectron. and Packaging Soc., Reston, 1999), pp. 53–56.
- [140] L. E. Stillwagon and R. G. Larson, *Phys. Fluids* **4**, 895 (1992).
- [141] C. J. Lawrence, *Phys. Fluids* **31**, 2786 (1988).
- [142] J. S. Kim, S. Kim, and F. Ma, *J. Appl. Phys.* **73**, 422 (1993).
- [143] K. Kohler, personal communication at project meeting, 2002.
- [144] R. Buchhold, A. Nakladal, G. Gerlach, K. Sahre, and K.-J. Eichhorn, *Thin Solid Films* **312**, 232 (1997).
- [145] S. Niyogi, S. Maiti, and B. Adhikari, *Polymer Degradation and Stability* **68**, 459 (2000).

- [146] D.-Y. Shih, N. Klymko, R. Flitsch, J. Paraszczak, and S. Nunes, *J. Vac. Sci. Technol.* **9**, 2963 (1991).
- [147] E. Breitmaier and G. Jung, *Organische Chemie*, 4th ed. (Georg Thieme Verlag, Stuttgart, New York, 2001), p. 118 ff.
- [148] G. Turban and M. Rapeaux, *J. Electrochem. Soc.* **130**, 2231 (1983).
- [149] J. M. Neiryneck, S. P. Murarka, and R. J. Gutmann, *Mat. Res. Soc. Symp. Proc.* **381**, 229 (1995).
- [150] G.-R. Yang, Y.-P. Zhao, J. M. Neiryneck, S. P. Murarka, and R. J. Gutmann, *J. Electrochem. Soc.* **144**, 3249 (1997).
- [151] C. L. Borst, D. G. Thakurta, W. N. Gill, and R. J. Gutmann, *J. Electrochem. Soc.* **146**, 4309 (1999).
- [152] Y. Ikada, *Biomaterials* **15**, 725 (1994).
- [153] V. Zaporozhchenko, T. Strunskus, K. Behnke, C. v. Bechtolsheim, M. Kiene, and F. Faupel, *J. Adhesion Sci. Technol.* **14**, 467 (2000).
- [154] D.-Q. Yang, M. Meunier, and E. Sacher, *Appl. Surface Science* **173**, 134 (2001).
- [155] H. W. Schock, personal communication, 2002.
- [156] H. Leybold, personal communication at ims chips, 2002.
- [157] J. G. Jinkins and R. E. Davis, *J. Vac. Sci. Technol. A* **11**, 1056 (1993).
- [158] S. Iwamori, T. Miyashita, S. Fukuda, S. Nozaki, K. Sudoh, and N. Fukuda, *Vacuum* **51**, 615 (1998).
- [159] K. W. Paik and A. L. Ruoff, *J. Adhesion Sci. Technol.* **4**, 465 (1990).
- [160] D.-Y. Shih, J. Paraszczak, N. Klymko, R. Flitsch, S. Nunes, J. Lewis, C. Yang, J. Cataldo, R. McGouey, W. Graham, R. Serino, and E. Galligan, *J. Vac. Sci. Technol. A* **3**, 1402 (1989).
- [161] P. O. Hahn, G. W. Rubloff, J. W. Bartha, F. Legoues, R. Tromp, and P. S. Ho, *Mat. Res. Soc. Symp. Proc.* **40**, 251 (1984).
- [162] E. Kondoh, T. P. Nguyen, D. W. Plachke, H. Carstanjen, and E. Arzt, *Appl. Phys. Lett* **70**, 1251 (1997).

- [163] M. Amagai, M. Ohsumi, E. Kawasaki, R. Baumann, and H. Kitagawa, in *IEEE Int. Reliability Ph. Proc.* (IEEE Inc., Piscataway, 1994), pp. 101–107.
- [164] M. Amagai, *Microelectronics Reliability* **40**, 2077 (2000).
- [165] R. F. Saraf, J. M. Roldan, and T. Derderian, *IBM J. Res. Develop.* **38**, 441 (1994).
- [166] V. Svorcik, E. Arenholz, V. Rybka, and V. Hnatowicz, *Nuclear Instruments and Methods in Physics Research B* **122**, 663 (1997).
- [167] D.-S. Seo, T. O.-Ide, H. Matsuda, T.-R. Isogami, K.-I. Muroi, Y. Yabe, and S. Kobayashi, *Mol. Cryst. Liq. Cryst.* **231**, 95 (1993).
- [168] G. Danev and E. Spassova, *Thin Solid Films* **228**, 301 (1993).
- [169] S. Gong and J. Kanicki, *SID 98 Digest* 722 (1998).
- [170] J. Lu, S. V. Deshpande, E. Gulari, and J. Kanicki, *J. Appl. Phys.* **80**, 5028 (1996).
- [171] C. Beleznai, R. Vajtai, and L. Nanai, *Fractals* **5**, 275 (1997).
- [172] S. Gong, J. Kanicki, L. Ma, and J. Z. Z. Zhong, *Mat. Res. Soc. Symp. Proc.* **508**, 229 (1998).
- [173] C. E. Hoyle, D. Creed, R. Nagarajan, P. Subramanian, and E. T. Anzures, *Polymer* **33**, 3162 (1992).
- [174] T. Nakata, F. Kannari, and M. Obara, *Optoelectronics-Devices and Technologies* **8**, 179 (1993).
- [175] C. D. Dimitrakopoulos and S. Kowalczyk, *Thin Solid Films* **295**, 162 (1997).
- [176] N. Inagaki, S. Tasaka, and K. Hibi, *J. of Polymer Science* **30**, 1425 (1992).
- [177] N. J. Chou, A. D. Marwick, R. D. Goldblatt, L. Li, G. Coleman, and J. E. Heidenreich, *J. Vac. Sci. Technol.* **10**, 248 (1992).
- [178] C. L. Borst, W. N. Gill, and R. J. Gutmann, in *CMP-MIC Conf. Proc.* (IMIC, Tampa, Florida, USA, 1999), pp. 409–412.

- [179] K. S. Patel, P. A. Kohl, and S. A. Allen, *J. of Polymer Science* **38**, 1634 (2000).
- [180] K. S. Patel, P. A. Kohl, and S. A. Bidstrup-Allen, in *IEEE Trans. on Componentss, Packaging and Manufacturing Technology B* (IEEE Inc., Piscataway, 1998), pp. 199–202.
- [181] K. R. Williams and R. S. Muller, *J. of Microelectromechanical Systems* **5**, 256 (1996).
- [182] R. D. Tacito and C. Steinbruechel, *J. Electrochem. Soc.* **143**, 2695 (1996).
- [183] M. J. Berry, I. Turlik, P. L. Smith, and G. M. Adema, *Mat. Res. Soc. Symp. Proc.* **227**, 351 (1991).
- [184] K. W. Paik, R. J. Saia, and J. J. Chera, *Mat. Res. Soc. Symp. Proc.* **203**, 303 (1991).
- [185] V. Parihar and R. Singh, *Mat. Res. Soc. Symp. Proc.* **511**, 241 (1998).
- [186] C. J. Mogab, A. C. Adams, and D. L. Flamm, *J. Appl. Phys.* **49**, 3796 (1978).
- [187] J. W. Butterbaugh, D. C. Gray, and H. H. Sawin, *J. Vac. Sci. Technol.* **9**, 1461 (1991).
- [188] D. T. Price, R. J. Gutmann, and S. P. Murarka, *Thin Solid Films* **308-309**, 523 (1997).
- [189] M. Schier, *J. Electrochem. Soc.* **142**, 3238 (1995).
- [190] M. R. Baklanov, S. Vanhaelemeersch, H. Bender, and K. Maex, *J. Vac. Sci. Technol. B* **17**, 372 (1999).
- [191] B. Rogers, M. J. Berry, I. Turlik, P. Garrou, and D. Castillo, *Intern. J. of Microcircuits and Electronic Packaging* **17**, 210 (1994).
- [192] H.-J. Krokoszinski, H. Oetzmann, H. Gernoth, and C. Schmidt, *Thin Solid Films* **135**, 1 (1986).
- [193] M. R. Reddy, N. Srinivasamurthy, and B. L. Agrawal, *European Space Agency Journal* **16**, 193 (1992).
- [194] B. A. Banks, M. J. Mirtich, S. K. Rutledge, and D. M. Swec, *Thin Solid Films* **127**, 107 (1985).

- [195] E. O. S. II, M. E. Mills, D. D. Hawn, J. C. Liu, and J. P. Hummel, in *IEEE Intern. Interconnect Technol. Conf. Proc.* (IEEE Inc., Piscataway, 1998), pp. 223–225.
- [196] D. Hegemann, U. Vohrer, C. Oehr, and R. Riedel, *Surface and Coatings Technology* **116-119**, 1033 (1999).
- [197] B. Heublein, K. Pethig, and A.-M. Elsayed, *J. Invas. Cardiol.* **10**, 255 (1998).
- [198] U. Beck, D. T. Smith, G. Reiners, and S. J. Dapkunas, *Thin Solid Films* **332**, 164 (1998).
- [199] W. Nisch, pers. comm., 2002.
- [200] C. de Duve, *Die Zelle. Expedition in die Grundstruktur des Lebens I + II*, 1st ed. (Spektrum der Wissenschaft Verlagsgesellschaft mbH Co., Heidelberg, 1986).
- [201] B. Schlosshauer, pers. comm., 2001.
- [202] M. F. Rajewsky, *Exp. Cell Res.* **60**, 269 (1970).
- [203] M. F. Rajewsky and A. Grueneisen, *Eur. J. Immunol.* **2**, 445 (1972).
- [204] W. F. Scherer, J. T. Syverton, and G. D. Gey, *J. Exp. Medicine* **97**, 695 (1953).
- [205] G. O. Gey, W. D. Coffman, and M. T. Kubicek, *Cancer Res.* **12**, 264 (1952).
- [206] R. I. Freshney, *Culture of Animal Cells*, 4th ed. (Wiley-Liss, New York, 2000), p. 179.
- [207] R. I. Freshney, *Culture of Animal Cells*, 4th ed. (Wiley-Liss, New York, 2000), p. 184.
- [208] A. Hauch and A. Georg, *Electrochimica Acta* **46**, 3457 (2001).
- [209] T. C. Hodge, S. A. B. Allen, and P. A. Kohl, *J. Polymer Science* **37**, 311 (1999).
- [210] O. Zinke and H. Seither, *Widerstände, Kondensatoren, Spulen und ihre Werkstoffe*, 2nd ed. (Springer Verlag, Berlin, Heidelberg, 1982), p. 141.

- [211] S. R. Morrison, *The Chemical Physics of Surfaces*, 2nd ed. (Plenum Press, New York, 1978), p. 265.
- [212] Y. V. Pleskov, *Solar Energy Conversion. A photochemical approach*, 1st ed. (Springer Verlag, Berlin, Heidelberg, 1990).
- [213] A. J. Bard and L. R. Faulkner, *Electrochemical Methods. Fundamentals and Applications*, 2nd ed. (John Wiley & Sons Inc., New York, Chichester, 2001), p. 368 ff.
- [214] J. R. Macdonald, *Impedance Spectroscopy*, 1st ed. (John Wiley & Sons, Inc., New York, Chichester, 1987), p. 12 ff.
- [215] A. C. Fisher, *Electrode Dynamics*, 1st ed. (Oxford University Press, Oxford, New York, 1996), p. 60 ff.
- [216] W. Juengst and C. Weddigen, *Elektronik*, 2nd ed. (Springer Verlag, Berlin, Heidelberg, 1993), p. 23 ff.
- [217] H. Haken and H. C. Wolf, *Atom- und Quantenphysik*, 7th ed. (Springer Verlag, Berlin, Heidelberg, 2000).
- [218] R. L. Liboff, *Introductory Quantum Mechanics*, 2nd ed. (Addison-Wesley Publishing Company, Inc., Reading, Massachusetts, 1992), p. 456.
- [219] S. F. Johnston, *Fourier Transform Infrared. A constantly evolving technology*, 1st ed. (Ellis Horwood Limited, Chichester, West Sussex, England, 1991), p. 84 f.
- [220] J. W. Cooley and J. W. Tukey, *Math. Comput.* **19**, 297ff (1965).
- [221] I. InfraRed Associates, personal communication, 1998.
- [222] C. U. PERKIN-ELMER, Norwalk, 1976.
- [223] K. Siegbahn, C. Nordling, A. Fahlman, R. Nordberg, K. Hamrin, J. Hedman, G. Johansson, T. Bergmark, S.-E. Karlsson, I. Lindgren, and B. Lindberg, *ESCA Atomic, molecular and solid state structure studied by means of electron spectroscopy, presented to the Royal Society of Sciences of Uppsala, Dec. 3rd, 1965* (Almqvist & Wiksells Boktryckeri AB, Uppsala, Sweden, 1967).
- [224] edited by D. Briggs and M. P. Seah, *Practical Surface Analysis*, 2nd ed. (John Wiley, Sons, Inc., Salle + Sauerlaender, Chichester, New York, Aarau, 1990), p. 112.

- [225] M. P. Seah and W. A. Dench, *Surf. Interface Anal.* **1**, 2 ff (1979).
- [226] C. D. Wagner, W. M. Riggs, L. E. Davis, J. F. Moulder, and G. E. Muilenberg, *Handbook of X-ray photoelectron spectroscopy*, 1st ed. (Perkin-Elmer Corp. Physical Electronics Division, Eden Prarie, Minnesota, USA, 1979), p. all.
- [227] D. A. Shirley, *Phys. Rev. B* **5**, 4709 ff (1972).
- [228] C. W. Ong, X. A. Zhao, Y. M. Ng, K. F. Chan, T. C. Tsang, and C. L. Choy, *Appl. Phys. Lett.* **69**, 3501 (1996).
- [229] T. M. Klein, T. M. Anderson, A. I. Chowdhury, and G. N. Parsons, *J. Vac. Sci. Technol.* **17**, 108 (1999).
- [230] M. Orfert and K. Richter, *Surface and Coatings Technol.* **116-119**, 622 (1999).
- [231] D. L. Smith, A. S. Alimonda, C.-C. Chen, S. E. Ready, and B. Wacker, *J. Electrochem. Soc.* **137**, 614 (1990).
- [232] D. Stryahilev, A. Sazonov, and A. Nathan, *J. Vac. Sci. Technol. A* **20**, 1087 (2002).
- [233] A. Izumi and H. Matsumura, *Appl. Phys. Lett.* **71**, 1371 (1997).
- [234] edited by D. Briggs and M. P. Seah, *Practical Surface Analysis*, 2nd ed. (John Wiley, Sons, Inc., Salle + Sauerlaender, Chichester, New York, Aarau, 1990), p. 207.
- [235] C. Laibrock and A. Stett, personal communication at NMI, 2001.
- [236] S. Poulin, D. Q. Yang, E. Sacher, C. Hyett, and T. H. Ellis, *Appl. Surface Science* **165**, 15 (2000).
- [237] D.-Q. Yang and E. Sacher, *Appl. Surface Science* **173**, 30 (2001).
- [238] C. E. Mohler, A. J. G. Strandjord, D. W. Castillo, M. R. Stachowiak, R. H. Heistand, P. E. Garrou, and T. G. Tessier, *Mat. Res. Soc. Symp. Proc.* **323**, 295 (1994).
- [239] P. Garrou, J.-H. Im, J. Hetzner, G. Meyers, D. Hawn, J. Wu, M. B. Vincent, and C. P. Wong, *IEEE Trans. on Advanced Packaging* **23**, 568 (2000).

- [240] Z. Qin, J. Zhang, H. Zhou, Y. Song, and T. He, *Nuclear Instruments and Methods in Physics Research B* **170**, 406 (2000).
- [241] A. R. K. Ralston, M. C. Buncick, D. D. Denton, T. E. Boltshauser, J. M. Funk, and H. P. Baltès, in *IEEE Transducers* (IEEE Inc., Piscataway, 1991), pp. 759–763.
- [242] C. J. Newsome and M. O’Neill, *J. Appl. Phys.* **88**, 7328 (2000).
- [243] A. Endo, M. Takada, K. Adachi, H. Takasago, T. Yada, and Y. Onishi, *J. Electrochem. Soc.* **134**, 2522 (1987).
- [244] M. Zuo, T. Takeichi, A. Matsumoto, and K. Tsutsumi, *Colloid Polym. Sci* **276**, 555 (1998).
- [245] C. E. Hoyle, D. Creed, E. T. Anzures, P. Subramanian, and R. Nagarajan, *SPIE* **1559**, 101 (1991).
- [246] A. Viehbeck, M. J. Goldberg, and C. A. Kovac, *J. Electrochem. Soc.* **137**, 1460 (1990).
- [247] O. W. Fischer, Diploma-thesis: Photoelektronenspektroskopische Untersuchungen an durch Plasma modifizierten Oberflächen., 1998.
- [248] C. A. Kovac, J. L. Jordan-Sweet, M. J. Goldberg, J. G. Clabes, A. Viehbeck, and R. A. Pollak, *IBM J. Res. Develop.* **32**, 603 (1988).
- [249] P. N. Sanda, J. W. Bartha, B. D. Silverman, and P. S. Ho, *Mat. Res. Soc. Symp. Proc.* **40**, 283 (1984).
- [250] P. S. Ho, R. Haight, R. C. White, and B. D. Silverman, *Journal de Physique* **49**, 49 (1988).
- [251] F. D. Egitto, L. J. Matienzo, K. J. Blackwell, and A. R. Knoll, *J. Adhesion Sci. Technol.* **8**, 411 (1994).
- [252] R. Flitsch and D.-Y. Shih, *J. Vac. Sci. Technol.* **8**, 2376 (1990).
- [253] S. G. Anderson, J. Leu, B. D. Silverman, and P. S. Ho, *J. Vac. Sci. Technol.* **11**, 368 (1993).
- [254] F. Kokai, H. Saito, and T. Fujioka, *J. Appl. Phys.* **66**, 3252 (1989).
- [255] G. Rozovskis, J. Vinkevicius, and J. Jaciauskiene, *J. Adhesion Sci. Technol.* **10**, 399 (1996).

- [256] Y. Nakamura, Y. Suzuki, and Y. Watanabe, *Thin Solid Films* **290-291**, 367 (1996).
- [257] G. E. Ponchak and A. N. Downey, *IEEE Trans. on Components, Packaging, and Manufacturing Technol. B* **21**, 171 (1998).
- [258] Zinke and Brunswig, *Lehrbuch der Hochfrequenztechnik, Bd. 1*, 1st ed. (Springer Verlag, Berlin, Heidelberg, 1990), p. 47 ff.
- [259] S. M. Sze, *Physics of Semiconductor Devices*, 2nd ed. (Wiley Interscience, New York, 1981), p. 67.
- [260] R. Dulbecco and M. Vogt, *J. Exp. Med.* **106**, 167 (1957).
- [261] R. Dulbecco and G. Freeman, *Virology* **8**, 396 (1959).
- [262] J. D. S. et al, *Virology* **12**, 185 (1960).
- [263] P. Karlson, D. Koenecke, and J. Koolman, *Biochemie*, 14th ed. (Georg Thieme Verlag, Stuttgart, 1994).

Danksagung¹

Ich möchte mich bei allen bedanken, die zum Gelingen dieser Arbeit beigetragen haben. Mein besonderer Dank gilt

- Prof. Dr. J. H. Werner für die Möglichkeit, mich mit der interdisziplinären Themenstellung auseinanderzusetzen, sowie für anregende Diskussionen und seine stete Förderung meiner Forschungsarbeit.
- Prof. Dr. E. Zrenner für die Übernahme des Mitberichts. Auf zahlreichen Projektbesprechungen hat er mich für die Arbeit an der Schnittstelle Medizin – Elektrotechnik / Physik begeistert.
- Dr. M. B. Schubert, dessen Besonnenheit, organisatorisches Talent und fachliche Betreuung viel zum Gelingen dieser Arbeit beigetragen haben. Er hatte immer ein offenes Ohr – für neue Forschungsideen genauso, wie für meine Sorgen.
- Dr. Brümmer, Prof. Dr. D. F. Hülser und Frau B. Rehkopf für die Gelegenheit, am Biologischen Institut mit in-vitro Zellkulturserien zu arbeiten. Ohne ihre tatkräftige Unterstützung wäre ein großer Teil der Arbeit nicht möglich gewesen.
- Dr. G. Bilger, der mich in die Tiefen der XPS Methode einführte. Als unermüdlicher Diskussionspartner hat er viel zur Klarheit bei der Interpretation der Messungen beigetragen.
- Heide Gruber am Institut für Mikroelektronik Stuttgart für viel Ausdauer bei der Vorbereitung und Aufzeichnung von Rasterelektronenmikroskop-Aufnahmen, sowie für die freundschaftliche Atmosphäre ;-)

¹Acknowledgment. All people listed here are German native speakers (with the exception of Kai Chen whose German is almost perfect). Hence no English acknowledgment is given.

- Dr. M. Schütz, Steffen Maisch und Dr. S. Seifritz für die gemeinsame Aufnahme und Diskussion zahlreicher Infrarot-Transmissionsspektren am Institut für organische Chemie.
- Dr. J. Egelhaaf vom Institut für Systemtheorie und Bildschirmtechnik für Plasma-Ätzungen an amorphem Silizium.
- Dr. V. Bucher für die Preparation der $\text{SiO}_x\text{:C/SiN}_x$ Proben am NMI.
- Sven Bauerdick am NMI, der mit mir die Polyimid Proben hergestellt hat.
- Dr. W. Nisch, Dr. M. Stelzle, Dr. A. Stett, Dr. C. Leibrock am NMI sowie H.- G. Graf am IMS für zahlreiche fachliche Diskussionen über technologische, physikalische und medizinische Fragestellungen rund um das Retina Implantat.
- Dr. S. Wolff in der Arbeitsgruppe Integrierte Optoelektronik der Universität Kaiserslautern, die mir die BCB Prozessierung beibrachte.
- A. Reiß für die Schnelligkeit bei der Anfertigung zahlreicher Spezialbauteile in der institutseigenen Werkstatt.
- Kai Chen aus Shanghai, China, für seine Bereitschaft, auch zu unkonventionellen Arbeitszeiten Impedanzspektren meiner Proben aufzuzeichnen.
- Christian Gemmer, Jörg Glöckner und Dr. K. Brühne, mit denen ich auf unseren obligatorischen Mittagsspaziergängen auch nicht-fachliche Diskussionen aller Art führen konnte. Darüber hinaus danke ich Jörg Glöckner für die gründliche Durchsicht der Gleichungen, die Impedanzmessungen und RGLC-Leitungen beschreiben.
- allen Mitarbeitern des Instituts für Physikalische Elektronik für die angenehme Arbeitsatmosphäre.

Meiner Freundin Julia Denger danke ich für das Korrekturlesen der Zusammenfassung der Arbeit. Ganz besonders danke ich meinen Eltern für ihre Begleitung, ihr Vertrauen und ihre immer währende Unterstützung während meines Studiums und der Promotion.

Curriculum vitae

Martin Rojahn

born on February 6 1973 in Halle an der Saale, Germany.

Education

9/79	–	6/89	primary school Oberschule Kröllwitz, Halle
9/89	–	6/91	high school Thomas-Müntzer-Gymnasium, Halle
6/91			Abitur

Community service

9/92	–	10/93	ambulance man at the Rettungsdienst Ammerland
------	---	-------	---

College

10/91	–	9/92	studies of physics at the
10/93	–	8/95	Carl von Ossietzky University Oldenburg,
9/96	–	10/98	minor subjects: chemistry, philosophy
7/94			intermediate diploma in physics
9/95	–	5/96	studies of physics and philosophy at the University of Saskatchewan, Saskatoon, Canada. project thesis: "The role of friendship in Aristotle's Nichomachean Ethics"
1/97	–	4/97	student research project: "Dark- and photoconductivity of microcrystalline silicon"
9/97	–	9/98	Diploma thesis: "Classification of clouds for the calculation of terrestrial solar irradiance from satellite data",
10/98			Diploma in physics

Dissertation

12/98		02/03	thesis "Encapsulation of a retina implant" at the Institute of Physical Electronics of the University of Stuttgart
-------	--	-------	--

Lebenslauf

Martin Rojahn

geboren am 6. Februar 1973 in Halle an der Saale.

Schulausbildung

9/79 – 6/89 Erweiterte Oberschule Kröllwitz, Halle
9/89 – 6/91 Thomas-Müntzer-Gymnasium, Halle
6/91 Abitur

Zivildienst

9/92 – 10/93 Rettungshelfer beim Rettungsdienst Ammerland

Studium

10/91 – 9/92 Studium der Physik an der
10/93 – 8/95 Carl-von-Ossietsky-Universität Oldenburg
9/96 – 10/98 Nebenfächer: Chemie, Philosophie
7/94 Vordiplom der Physik
9/95 – 5/96 Studium der Physik und Philosophie
 an der University of Saskatchewan,
 Saskatoon, Kanada. Projektarbeit: "Die Rolle
 der Freundschaft in Aristoteles' Nikomachischer Ethik"
1/97 – 4/97 Studienarbeit: "Dunkel- und Photoleitfähigkeit von
 mikrokristallinem Silizium"
9/97 – 9/98 Diplomarbeit: "Wolkenklassifizierung zur Berechnung
 der Einstrahlung am Boden aus Satellitendaten"
10/98 Diplom der Physik

Promotion

12/98 – 2/03 Thema: "Verkapselung eines Netzhaut-Implantates",
 Institut für Physikalische Elektronik,
 Universität Stuttgart

Erklärung

Hiermit erkläre ich, dass ich die vorliegende Dissertation "Encapsulation of a retina implant" selbstständig verfasst und nur die angegebenen Hilfsmittel verwendet habe.

Stuttgart, den 17. 02. 2003

(Martin Rojahn)

I hereby declare that I compiled the present thesis on my own and by making use only of the resources cited and that all the passages taken from other works are indicated as borrowings via specification of the original source.

Stuttgart, February 17 2003

(Martin Rojahn)